UNIVERSITY OF CALIFORNIA

SANTA CRUZ

THE PRODUCTION AND EVOLUTION OF SCALING LAWS VIA GALAXY MERGING

A dissertation submitted in partial satisfaction of the
requirements for the degree of

DOCTOR OF PHILOSOPHY

in

PHYSICS

by

Matthew D. Covington

September 2008

The Dissertation of Matthew D. Covington
is approved:

_____

Professor Joel Primack, Chair

_____

Professor Sandra Faber

_____

Professor Avishai Dekel

_____

Lisa C. Sloan
Vice Provost and Dean of Graduate Studies

Table of Contents

List of Figures

List of Tables

Abstract

The Production and Evolution of Scaling Laws via Galaxy Merging

by

Matthew D. Covington

Galaxy mergers are a major force in the formation of galaxies. We study a large suite of hydrodynamical galaxy merger simulations in order to better understand how mergers could lead to the development and evolution of galaxy scaling laws. We begin by constructing a physically-motivated analytical model that predicts the properties of the remnants of galaxy mergers. The free parameters in this model are calibrated using the simulation set. Once developed, the merger model is applied to two Semi-Analytic Models of galaxy formation and used to study the production and evolution of elliptical galaxy scaling laws via merging. We demonstrate that major mergers of disk galaxies are capable of producing the observed scaling relations. The tilt of the fundamental plane and the rotation of the size-mass relation from that of disks, are the result of a gas gradient in the progenitor galaxies.

We also demonstrate that galaxy mergers are capable of reproducing the observed high-redshift Tully-Fisher law outliers along with the tight $S_{0.5}$-stellar mass relation. Furthermore, we show using the simulations that $S_{0.5}$ tracks the total enclosed mass including the contribution from dark matter.

To my late Grandfather,

Jess B. Covington,

who helped to instill in me at an early age

the thrill of exploration

and the joy of imagination.

Acknowledgments

Chapter 1

Introduction

Over the past 30 years cosmology has converged toward a coherent picture of the global evolution of the universe since its inception with the big bang. Structure in the universe forms from the imprint of a primordial power spectrum that results from the stretching of quantum fluctuations over large scales during an early inflationary period in the universe's existence. These quantum fluctuations provide the density contrasts necessary to seed the formation of structure in the universe. In the ΛCDM, 'concordance', cosmology structure forms hierarchically as overdense regions of the universe collapse and merge into larger and larger masses. These structures are primarily made of a poorly understood form of weakly interacting matter, dark matter. These dark matter halos are dominantly controlled via simple gravitational interactions. Because non-gravitational, dissipative effects can be ignored, we have fairly quickly come to an understanding about how such structure would form, through both analytical techniques (Zel'Dovich, 1970; Gunn & Gott, 1972) and N-body simulations (Springel et al., 2005; Diemand et al., 2006).

However, as this picture has fallen into place, astrophysicists have turned to the more complex problem of understanding the visible component of the universe, baryons, which we see primarily in the form of stars within galaxies. Galaxy formation is a complex process that results from a combination of gravitational and hydrodynamical forces, and is even affected by poorly understood small-scale physical processes such as supernova feedback and accretion onto supermassive black holes. Thus the jump from dark matter halo formation to galaxy formation is non-trivial and marks one of the central questions in astrophysics today.

As structure forms hierarchically, through the merging of larger and larger halos, an important question is the extent to which merging plays a role in galaxy formation. It was noted by Toomre & Toomre (1972) that galaxy mergers are capable of explaining many of the curious disturbed galaxies in the observed universe with features such as tidal tails or bridges, and furthermore that merger remnants would look very similar to observed elliptical galaxies. Numerous previous studies have used computer simulations to glean understanding about galaxy mergers and have demonstrated that mergers of disk galaxies produce objects that are very similar to observed elliptical galaxies (Toomre & Toomre, 1972; Barnes & Hernquist, 1992; Mihos & Hernquist, 1994b; Naab et al., 1999; Cox et al., 2006; Robertson et al., 2006; Boylan-Kolchin et al., 2006; Hopkins et al., 2006; Cox et al., 2008a).

Of particular interest is to what extent mergers are responsible for creating elliptical galaxies. There is another proposed mechanism for creating ellipticals, monotonic collapse (Larson, 1974; Pipino & Matteucci, 2004). If both of these mechanisms play a role, then do they populate different regions of the space of elliptical galaxy properties? Furthermore, observed elliptical galaxies fall on a number of scaling relations, including the size-mass relation (Kormendy, 1977), the Faber-Jackson relation (Faber & Jackson, 1976), and the tight fundamental plane (Dressler et al., 1987; Djorgovski & Davis, 1987). Can galaxy mergers reproduce the observed relations? If so, do the processes that occur during mergers provide us with physical explanations for any of the relations? These are the broad questions within galaxy formation that motivate this dissertation work.

3

During his dissertation work, T.J. Cox, a collaborator of the author and previous student of the author's adviser, constructed a large suite of galaxy merger simulations, which probed many possible initial conditions with a number of progenitor types and a variety of orbits (Cox, 2004; Cox et al., 2006, 2008a). This dissertation mines T.J's merger suite, rich data set that it is, to address many questions about the role of galaxy mergers in galaxy formation.

While it is possible to simulate specific merger cases, simulating a set of mergers large enough to statistically represent all of the various merger scenarios over the history of the real universe remains beyond the power of current computing resources. Galaxy formation on this scale is usually studied using semi-analytic models (SAMs). In Chapter 2, I develop a physically-based model for predicting the properties of merger remnants from the initial conditions of a merger and the progenitor properties. This model provides insight into the physical processes that occur during mergers and also provides a recipe for SAMs that allows the study of the properties of statistical samples of merger remnants over cosmological time. In Chapter 3, I apply this new merger model to two different SAMs, use the results to study the scaling relations of merger remnants over time, and make comparisons with observed scaling relations. Given progenitor properties that match the observed distributions, the model is capable of reproducing the observed scaling relations, and furthermore provides insight into how they arise via the merger process. This suggests that mergers are not only a viable mechanism for producing ellipticals, but that features of the merger process, particularly gas dissipation, help to explain the observed relations. In Chapter 4, I demonstrate that the merger

simulations can explain a novel observational finding by Kassin et al. (2007) concerning the kinematics of high redshift galaxies. I then use the simulations to interpret the observational results. The simulations demonstrate that the new kinematic parameter, $S_{0.5}$, effectively tracks the central galaxy mass, including the contribution from dark matter.

Chapter 2

Predicting the Properties of Merger

Remnants

2.1 Introduction

Major mergers between galaxies are central to the formation and evolution of elliptical galaxies (Toomre & Toomre, 1972; Toomre, 1977; Mihos & Hernquist, 1994a). The hierarchical buildup of galaxies in the ΛCDM cosmology consists of a sequence of mergers, of which a significant fraction are "major," involving progenitors with a mass ratio larger than 1:3. The gravitational interactions in such mergers have a dramatic effect on the dynamics and morphology of the galaxies, in particular turning rotating disks into pressure-supported spheroids. If the progenitors also contain gas, the mergers induce starbursts followed by gas consumption, which leads to aging stellar populations. The modeling of major mergers is therefore a key element in the attempts to confront the broad picture of galaxy formation with detailed observations. This is commonly performed via simulations incorporating Semi-Analytic Models (SAMs), where the complex physical processes are modeled using simplified parametric recipes.

Advanced SAMs are currently attempting the non-trivial task of following the sizes and internal velocities of galaxies. For disk galaxies, sizes are evaluated using the halo virial radii R_{vir} and spin parameters λ via $R_{\mathrm{disk}} \simeq \lambda R_{\mathrm{vir}}$, with some modifications due to the halo density profile (Fall & Efstathiou 1980; Mo, Mao & White; Bullock, Dekel et al. 2001; Dutton et al. 2006). The sizes of the remnants of gas-poor ("dry") mergers, where the dominant interaction is gravitational, can be extracted from the properties of the progenitors and the orbital energy by assuming conservation of energy and relaxation to virial equilibrium (Cole et al., 2000a). These considerations work well

in simulations of relatively dry mergers, quite independently of the details of the orbit.

While dry mergers may dominate in the formation of the most massive galaxies (Naab et al., 2006), the most common mergers are "wet" mergers of gaseous galaxies. It is thought that gas processes play an important role in the formation of ellipticals (Robertson et al., 2006; Dekel & Cox, 2006; Ciotti et al., 2007). As demonstrated below, the sizes predicted by dissipationless energy conservation can be off by a factor of a few for gas-rich mergers. Our goal is to construct a more accurate recipe to predict the size and velocity dispersion of the remnant of a wet merger given the properties of the progenitors and the orbital parameters. Cosmological mergers involve a complex mixture of variables (such as orbital parameters, gas fractions, mass ratio and bulge fraction) and physical processes (such as star formation and feedback), all of which can influence the properties of the merger remnants. Given a rich suite of high-resolution SPH merger simulations (Cox, 2004; Cox et al., 2006), that span the available parameter space and physical processes, albeit in a rather sparse and nonuniform manner, we seek a model that will properly represent the simulation results and enable an interpolation between them as well as an extrapolation to outside the simulated regime.

For such a recipe to be successful, it should be based on a toy model that grasps the essence of the main physical processes involved in wet mergers. Our intuition is guided by the finding from the simulations that the remnants are more compact when the initial gas fraction is higher and when the first passage involves a stronger tidal impulse, namely when a larger fraction of the orbital energy turns into internal kinetic energy. At a first glance, this may seem surprising, as a system that gains energy is not

expected to become more tightly bound, and indeed, the remnants of dry mergers are not very sensitive to the strength of the impulse. This dependence on gas fraction and on the impulse implies that a higher gas fraction and a stronger impulse are associated with a higher degree of dissipation, via shocks, collisions of gas clouds, and induced gas flows toward the centres of the merging systems. The resultant higher gas densities enhance the energy losses to radiation, leaving behind a more tightly bound remnant. In parallel, the higher degree of dissipation yields a stronger burst of star formation, which tends to be focused in the central region of the remnant. This understanding is the basis for our proposed recipe, which characterizes the merger by the impulse at first passage, evaluates the associated degree of dissipation and the resultant radiative energy losses and star formation, and accounts for these energy losses in the energy balance. A few free parameters with values of order unity can hopefully compensate for the crude approximations made. These approximations include, for example, an assumption of structural homology between the progenitors and remnant. The physically motivated recipe is then calibrated using the merger simulations, and its success is to be judged by its accuracy in matching the simulated remnant properties.

In §2.2 we describe the simulations used for this study. In §2.3 we present the details of our model for predicting remnant properties. In §2.4 we generalize the model to unequal mass mergers. In §2.5 we discuss certain limitations of our model, and in §2.6 we summarize our conclusions. Appendix A discusses the details of our impulse approximation. Appendix B presents an explicit recipe for SAMs.

2.2 Merger Simulations

2.2.1 Numerical Code

The numerical simulations analyzed in this work are part of a large suite of galaxy merger simulations designed to study the induced star formation (Cox, 2004; Cox et al., 2006) and observable counterparts (Jonsson, 2006; Jonsson et al., 2006) of such events. Details of these simulations can be found in the above references, but we include here a brief description for completeness.

All numerical simulations performed in this work use the N-Body/SPH code GADGET (Springel, Yoshida & White, 2001). Hydrodynamics are included via the Lagrangian technique of smoothed particle hydrodynamics (SPH). We use the "conservative entropy" version of SPH (Springel & Hernquist, 2002). Gas is assumed, for simplicity, to be a primordial plasma that can radiatively cool via atomic and free-free emission.

All of the numerical simulations presented here include star formation. Stars are formed in regions of gas which are above a critical density for star formation at a rate proportional to the local gas density and inversely proportional to the local dynamical time-scale. The efficiency of star formation is fixed by requiring star formation to follow the observed correlation between gas and star-formation rate surface densities (Kennicutt, 1998).

We also include a simple prescription to simulate the effects of feedback from massive stars. This feedback acts to pressurize the interstellar medium and regulates

the conversion of gas to stars. Details of this model and the parameter choices can be found in Cox et al. (2006). Specifically, most simulations studied in this paper used the $n2med$ parameter set. Under these assumptions the gas pressure increases as the density squared; i.e, star-forming gas has a "stiff" equation of state. Other cases are discussed in §2.5.

The simulations presented here adopt a gravitational softening length $h = 400$ pc for the dark matter particles and 100 pc for the stellar and gas particles. We remind the reader that, in GADGET, forces between neighboring particles become non-Newtonian for separations $< 2.3\,h$.

2.2.2   Initial Galaxies

All of the simulations presented here are mergers between two identical disk galaxies, except for cases discussed in §2.4. The disk galaxy models are motivated by observations of low-redshift galaxies. In some cases we made systematic studies of varying progenitor galaxy properties (e.g. varying gas fraction in the G3 gas fraction series). While many of these varied cases would not look like typical low-redshift galaxies, we made no attempt to vary properties in such a way as to capture variation with redshift. Furthermore, the simulations are not cosmological since the two galaxies are isolated. Disk galaxies are constructed in equilibrium and contain dark matter, an exponential stellar disk, an extended exponential gas disk, and some contain a dense central bulge. Our suite consists of five main types of models, detailed in Table 2.1:

1. Z galaxies are gas-poor bulgeless disks and are roughly modeled after the Milky

Way.

2. D galaxies are $\frac{1}{100}$ of the mass of the Z's, are bulgeless disks, and have a high gas fraction.

3. Y galaxies are $\frac{1}{10}$ of the mass of the Z's, are bulgeless disks, and have a high gas fraction.

4. Sbc galaxies are modeled after local Sbc-type spirals, with a small bulge and high gas fraction.

5. G galaxies span a range of mass, bulge fraction, and gas fraction. Their properties are taken from statistical samples of local galaxies, including the SDSS. Their dark matter halos have not been adiabatically contracted (Blumenthal et al., 1984; Mo et al., 1998), unlike all the other models.

The ratio of the gas to stellar exponential radii varies with model type. For the Z, D, and Y models, the gas and stellar radii are equal. For the Sbc and G models, the gas radii are three times the stellar radii. For more detail on these models see Cox (2004).

2.2.3 Merger Orbits

The sizes of merger remnants are affected by the initial orbits and orientations. To understand this relationship a sufficient exploration of the merger orbit and orientation parameter space is required. To this end, we perform mergers on an identical orbit with various orientations of the merging galaxies. We also perform mergers with many

Table 2.1: Properties of progenitor galaxy models. M_{tot} is total mass, baryons plus dark matter; c is concentration ($R_{\text{vir}}/r_{\text{s}}$); M_{stars} is the initial stellar mass; B/D is the bulge-to-disk ratio; f_{g} is the initial gas mass divided by M_{tot}; $R_{1/2}$ is the initial three-dimensional stellar half mass radius.

Type	M_{tot} $(10^{10}\text{M}_\odot)$	c	M_{stars} $(10^{10}\text{M}_\odot)$	B/D	f_{g}	$R_{1/2}$ (kpc)
Milky Way Series						
D	1.4	20	0.036	0	0.025	1.16
Y	14.0	15	0.3	0	0.02	2.85
Z	143.0	12	5.1	0	0.004	4.04
Sbc Series						
Sbc	81.4	11	4.92	0.26	0.066	7.15
G Series						
G0	5.0	14	0.1	0.02	0.012	1.84
G1	20.0	12	0.5	0.06	0.010	2.33
G2	51.0	9	1.5	0.11	0.009	2.90
G3	116.0	6	5.0	0.22	0.011	3.90
G3 Gas Fraction Series						
G3gf1	116.0	6	3.6	0.32	0.023	3.49
G3gf2	116.0	6	2.6	0.52	0.031	2.89
G3gf3	116.0	6	1.5	1.34	0.040	1.77
G3gf4	116.0	6	5.3	0.20	0.005	3.96

different orbits. Of all of the galaxy models, the Sbc models have the largest variety of orbits and orientations. The majority of the orbits in the suite are parabolic or near parabolic with eccentricities of 0.9 to 1.0. While these orbits are generally motivated by statistics from N-body simulations (Benson, 2005; Khochfar & Burkert, 2006), the distribution of orbits in the merger suite was not designed to exactly duplicate these statistics.

2.3 Modeling Properties of the Remnants

2.3.1 Non-dissipative Energy Conservation Model

Energy conservation during the merger may be a useful constraint to impose. If the progenitors and the remnant are homologous, then energy conservation and the virial theorem may be applied to the stellar systems as if they are self-gravitating without introducing a large error. Current SAMs employ such considerations to predict merger remnant radii (Cole et al., 2000a; Hatton et al., 2003). We start by summarizing the model of Cole et al.

In order to take orbital energy into account, this model assumes that the baryonic components of the progenitors spiral in under dynamical friction, losing energy to the outer dark matter halo, until reaching a distance that equals the sum of their three-dimensional stellar half-mass radii. Energy conservation is assumed from this point on. Thus the orbital energy term in the conservation equation is equal to the energy of a zero eccentricity (circular) orbit of the two galaxies with a constant separation equal to

Table 2.1: The orbital parameters of each of the equal mass merger simulations used in this study. Values are calculated from the orbital initial conditions assuming a point mass orbit. R_{peri} denotes pericentric distance. e denotes eccentricity. For equal mass mergers θ_1 and θ_2 denote the orientation of the first and second galaxy with respect to the orbital plane, where for $\theta_1 = 0$ the first galaxy is aligned with the orbital plane. For unequal mass mergers θ denotes the orientation of the orbit of the smaller progenitor with respect to the orientation of the larger progenitor. Again, $\theta = 0$ represents a case where the merger orbit aligns with the larger progenitor.

Equal Mass Mergers (55 runs)				
name	R_{peri} (kpc)	e	θ_1	θ_2
D1mf-u1	1.1	1.0	0	30
D2mf-u1	2.4	1.0	0	30
D3mf-u1	4.1	1.0	0	30
D4mf-u1	6.4	1.0	0	30
D5mf-u1	8.9	1.0	0	30
D6mf-u1	12.9	1.0	0	30
D7mf-u1	0.6	1.0	0	30
G0G0a-u1	2.24	0.95	-30	30
G0G0r-u1	2.24	0.95	150	30
G0G0-u1	2.24	1.0	-30	30
G1G1a-u1	2.96	0.95	-30	30
G1G1r-u1	2.96	0.95	150	30
G2G2r-u1	3.82	0.95	150	30
G2G2-u1	3.82	0.95	-30	30
G3blv5G3blv5-u1	13.6	0.95	-30	30
G3G3a-u1	13.6	0.95	-30	30
G3G3b-u1	13.6	0.95	-30	30
G3G3r-u1	13.6	0.95	150	30
G3gf1G3gf1b-u1	13.6	0.95	-30	30
G3gf2G3gf2b-u1	13.6	0.95	-30	30
G3gf3G3gf3b-u1	13.6	0.95	-30	30
G3gf4G3gf4b-u1	13.6	0.95	-30	30
Y1mf-u1	2.9	1.0	0	30
Y2mf-u1	5.7	1.0	0	30
Y3mf-u1	10.0	1.0	0	30
Y4mf-u1	15.7	1.0	0	30
Y5mf-u1	21.4	1.0	0	30
Y6mf-u1	31.4	1.0	0	30

name	R_{peri} (kpc)	e	θ_1	θ_2
Sbc201-u4	11.0	1.0	0	30
Sbc202-u4	11.0	1.0	180	30
Sbc203-u4	11.0	1.0	180	210
Sbc204-u4	5.5	1.0	0	30
Sbc205-u4	44.0	1.0	0	30
Sbc206-u4	11.0	1.0	90	30
Sbc207-u4	11.0	1.0	270	30
Sbc208-u4	5.5	1.0	180	30
Sbc209-u4	5.5	1.0	180	210
Sbc211-u4	44.0	1.0	180	210
Sbc212-u4	11.0	0.9	0	30
Sbc213-u4	25.0	0.8	0	30
Sbc214-u4	44.0	0.8	0	30
Sbc215-u4	100.0	1.0	0	30
Sbc216-u4	100.0	0.8	0	30
Sbc217-u4	11.0	1.0	90	90
Sbc218-u4	11.0	0.9	180	210
Z2m-u1	7.1	1.0	0	30
Z7m-u1	21.4	0.9	0	30
Z8m-u1	35.7	0.8	0	30
Z9m-u1	1.7	1.0	0	30
Z10m-u1	3.9	1.0	0	30
Z11m-u1	14.2	1.0	0	30
Z12m-u1	22.2	1.0	0	30
Z13m-u1	30.4	1.0	0	30
Z14m-u1	44.7	1.0	0	30
Z15m-u1	8.1	1.0	0	30

Table caption (above): Equal Mass Mergers (continued)

Table 2.2: The orbital parameters of each of the unequal mass simulations used in this study.

Unequal Mass Mergers (22 runs)				
name	R_{peri} (kpc)	e	θ	Mass Ratio
G1G0-u3	2.96	0.95	-30	1:3.9
G1G0r-u3	2.96	0.95	150	1:3.9
G2G0-u3	3.82	0.95	-30	1:10
G2G0r-u3	3.82	0.95	150	1:10
G2G1-u3	3.82	0.95	-30	1:2.6
G2G1r-u3	3.82	0.95	150	1:2.6
G3G1a-u1	13.6	0.95	0	1:5.8
G3G1b-u1	13.6	0.95	-90	1:5.8
G3G1c-u1	13.6	0.95	-60	1:5.8
G3G1d-u1	13.6	0.95	180	1:5.8
G3G1e-u1	6.8	0.95	-30	1:5.8
G3G1f-u1	27.2	0.95	-30	1:5.8
G3G1g-u1	64.4	0.95	-30	1:5.8
G3G1h-u1	120	0	-30	1:5.8
G3G2a-u1	13.6	0.95	0	1:2.3
G3G2b-u1	13.6	0.95	-90	1:2.3
G3G2c-u1	13.6	0.95	-60	1:2.3
G3G2d-u1	13.6	0.95	180	1:2.3
G3G2e-u1	6.8	0.95	-30	1:2.3
G3G2f-u1	27.2	0.95	-30	1:2.3
G3G2g-u1	64.4	0.95	-30	1:2.3
G3G2h-u1	120	0	-30	1:2.3

the sum of their half-mass radii,

$$\frac{(M_1 + M_2)^2}{R_{\mathrm{f}}} = \frac{M_1^2}{R_1} + \frac{M_2^2}{R_2} + \frac{1}{c}\frac{M_1 M_2}{R_1 + R_2}. \tag{2.1}$$

This equation relates the stellar three-dimensional half-mass radius of the remnant, R_{f}, to the masses and three-dimensional stellar half-mass radii of the progenitors, M_1, M_2, R_1 and R_2, respectively. For major mergers, the masses are assumed to include the total stellar mass plus, as a rather arbitrary choice, twice the dark matter masses within R_1 and R_2 respectively. The constant c is a structural parameter which relates GM^2/R to the actual internal binding energy. It is assumed to take the same value, $c = 0.5$, for both the progenitors and the remnant.

This model, though crude, provides a general framework for estimating the outcome of a given merger. However, it has not been previously tested against realistic simulations that include gas dynamics and star formation. We begin by applying this recipe to the cases in our merger simulation suite. The predictions of the model are plotted against the actual half-mass radii of the simulated remnants in Figure 2.1. Throughout this paper we use the fractional rms scatter, S, to assess goodness of fit.

$$S = \sqrt{\frac{1}{N}\sum \frac{(P_{\mathrm{predicted}} - P_{\mathrm{true}})^2}{P_{\mathrm{true}}^2}}, \tag{2.2}$$

where P is some property that we are trying to predict from the initial conditions and are measuring from the simulation for comparison.

The predictions of this simple model deviate from the true radii by $S = 0.50$. Figure 2.1 shows that the model systematically over-predicts the radii of the remnants.

18
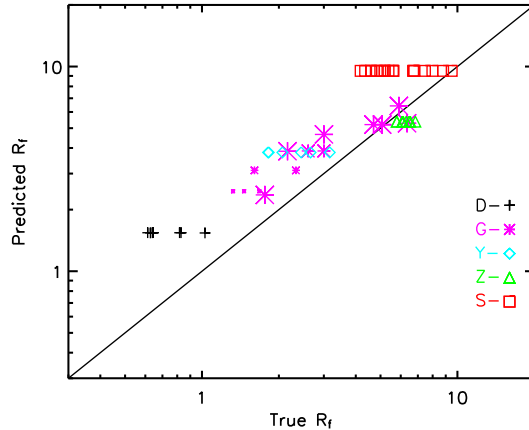
Figure 2.1: Dissipationless energy conservation model. The three-dimensional half-mass radii predicted by the model versus the actual radii in the simulated remnants. The symbols and colors denote the type of progenitors (Table 1): D (black crosses), G (purple asterisks), Y (blue diamonds), Z (green triangles) and Sbc (red squares). The symbols for G's have four different sizes which represent the different types of G progenitors. Larger symbols represent more massive galaxies. With a relatively large scatter of $S = 0.5$, this dissipationless model systematically over-predicts the sizes of the remnants, because it does not address the radiative energy losses.

This is a straightforward result of ignoring the radiative energy losses. Note that the predictions are best for the cases where the progenitors have the lowest gas fraction, cases Z and G3. For each type of progenitor, we see a wide spread in actual sizes for a given predicted size. This results from the variations in orbits and orientations, which are not addressed by the model. Despite the shortcomings of the dissipationless energy conservation model, it is a useful starting point. Our next goal is to correct for the dissipative effects.

19

2.3.2   A Toy Model for Radiative Losses

While the above dissipationless model works quite well in the case of low gas fraction, dissipative losses are likely to play an important role in the gas-rich mergers that were especially frequent in the early epochs of galaxy formation. In particular, they seem to be a crucial element in the formation of the Fundamental Plane of elliptical galaxies (Robertson et al., 2006; Dekel & Cox, 2006). We therefore wish to incorporate the radiative losses in our model.

When two gas-rich galaxies merge, a number of processes cause gas interactions and result in radiative energy losses. Tidal torques during a close pass can decrease the angular momentum in the gas disks and induce inflows into the galaxy centres. In a nearly radial encounter, the gas disk of one galaxy collides with that of the other creating shocks, which can result in loss of angular momentum. Furthermore, tidal forces during a merger introduce orbital crossings and density perturbations within the gas disks which ultimately lead to an increased gas collision rate. As the gas clouds collide and radiate away their kinetic energies, they fall toward the centre of the galactic potential well. This results in higher gas densities which lead to star formation and further radiative losses. Hence, the orbit, energy losses, and star formation are intimately linked.

The first step toward predicting energy losses from a given initial configuration is to characterize the perturbative strength of a given encounter. More specifically, we need to assess the dependence of the gas collisions and dissipation on the properties of the orbit. We find that the dissipation resulting from a given orbit can be characterized

using the orbital parameters at the first close pass. This may seem surprising at first, since often most of the stars are formed in the final coalescence rather than at the initial encounter, but it can be explained by the sequence of events following the first pass. The gas disks are perturbed during the first pass, inducing a continuous gas in-fall toward the galactic centre, lasting ~ 1 Gyr. A stronger disturbance in the first pass leads to a larger buildup of gas in the progenitor centres. Some of this gas is involved in a first starburst immediately following the first pass, but a large fraction of this gas serves as a reservoir for star formation during the later stages of the merger, especially the violent final coalescence. Consequently, an orbit that is more disruptive on the first pass also suffers more energy losses, and forms more stars, during the final coalescence. This is illustrated in Figure 2.2.

During a close pass of two galaxies, orbital energy is injected into the internal kinetic energies of both galaxies. We define this "impulse" as the difference between the peak in the total internal kinetic energies during the encounter and the total initial internal kinetic energies of the two progenitors. We approximate the impulse on galaxy 1 by

$$\Delta E = \frac{AG^2 M_{1,\mathrm{tot}}^2 M_{2,\mathrm{tot}}}{V_{\mathrm{peri}}^2 (R_{\mathrm{peri}}^2 + B\ R_{1,\mathrm{tot}}\ R_{\mathrm{peri}} + C\ R_{1,\mathrm{tot}}^2)}, \qquad (2.3)$$

where $M_{1,\mathrm{tot}}$ and $M_{2,\mathrm{tot}}$ are the total mass of the perturbed and perturbing galaxies respectively, baryons plus dark matter, and $R_{1,\mathrm{tot}}$ is the total half mass radius of the perturbed galaxy. R_{peri} is the "pericentric distance" of the first passage, as calculated from the initial orbit assuming point masses. The best-fitting values of the parameters are found to be $A = 1.6$, $B = 1.0$ and $C = 0.006$. The fit of the equation to the impulse

21
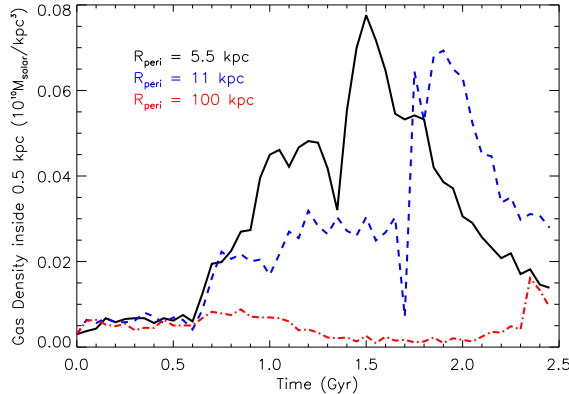
Figure 2.2: The central gas density in the inner 0.5 kpc during three separate Sbc mergers with initial orbital pericentric distances of 5.5, 11 and 100 kpc (solid black, dashed blue, and dash-dot red respectively). In all cases, the initial pass occurs at 0.6 Gyr. Final coalescences occur at roughly 1.5, 1.8 and 2.4 Gyr respectively. The plot demonstrates that the central gas density in the period following the first pass is increasing with decreasing pericentre distance, and that the density at the final coalescence is following the same trend.

measured from the simulations in shown in Figure 2.3. A more detailed discussion of this impulse approximation is given in Appendix A.

We characterize the dissipative strength of a merger using the fractional impulse at the first pass, $f_k \equiv \Delta E / K_{\text{tot}}$, where ΔE is the impulse and K_{tot} is the total initial internal kinetic energy of the galaxy, baryons and dark matter. We find that f_{new}, the fraction of new stars formed in the merger relative to M_{tot}, is indeed proportional to the fractional impulse and to the gas fraction f_{g},

$$f_{\text{new}} = C_{\text{new}} \ f_{\text{g}} \ f_{\text{k}}. \tag{2.4}$$

The best fit to our simulations is obtained for $C_{\text{new}} \sim 0.3$. The gas fraction determines the overall normalization of star formation, whereas the impulse factor tracks the vari-
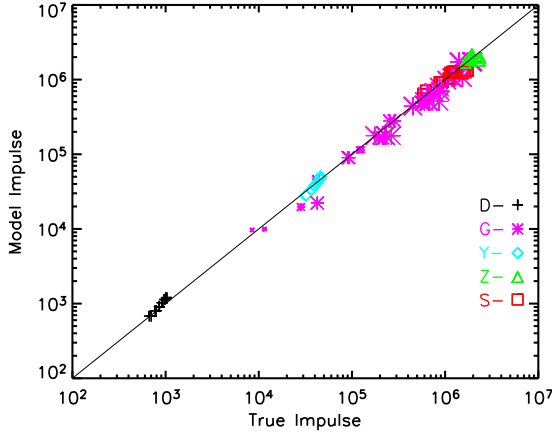
Figure 2.3: The approximation for the impulse against the measured impulse from the simulations. $S = 0.40$.

ations with orbit. This prediction for the fraction of new stars is plotted in Figure 2.4 against the actual fraction of new stars in the simulated remnants. In order to consistently treat the star formation in simulations that were run for different lengths of time, and in keeping with previous work (Somerville et al., 2001), we separate star formation into a merger-induced burst component and a quiescent component. We accomplish this by subtracting out star formation measured from simulations of each progenitor in isolation. The quantity f_{new} in equation 2.4 refers to the burst component only.

Given the above correlation between impulse and star formation, we proceed to predict the energy loss by assuming that the colliding gas that forms new stars during the merger loses a constant fraction of its kinetic energy in the collision. In more detail, we make the following assumptions:

1. Gas clouds have initial velocities approximately equal to the average initial veloc-
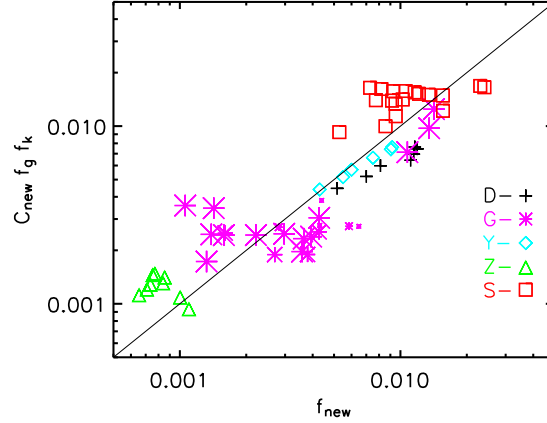
Figure 2.4: Fraction of new stars formed during the merger: the approximation based on gas fraction and impulse versus the actual value in the simulations. A stronger perturbation from a larger impulse enhances the collision rate between gas clouds, and thus induces more star formation.

ities of the dark matter/baryon system.

2. The average impulse per mass imparted to gas that will form new stars is approximately equal to the average impulse per mass for the entire dark matter/baryon system.

3. The energy lost during the merger is proportional to the kinetic energy of the gas that will form stars. This includes: 1) the initial kinetic energy, and 2) the kinetic energy gained from the impulse.

While simplistic, these assumptions allow us to make a connection between radiative losses and star formation. Assumption (i) would be valid if the system resembled an isothermal sphere. Assumption (iii) provides a sensible way for parameterizing the energy loss, given that it is associated with collisions of gas clouds. Under this

24
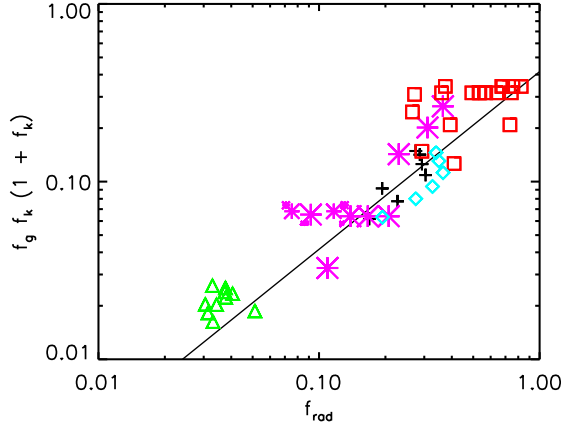
Figure 2.5: Fractional energy loss. The approximation of radiative losses in equation 2.6, which is based on gas fraction and impulse, is shown against the actual radiative energy losses. It demonstrates a crude proportionality, with the line plotted $y = 0.4x$.

assumption, the radiative energy loss can be written as

$$E_{\text{rad}} \propto (f_{\text{new}} \ K_{\text{tot}} + f_{\text{new}} \ \Delta E). \qquad (2.5)$$

The first term is the total initial internal kinetic energy of the gas that forms stars, and

the second term is the energy imparted to that gas by the impulse. Dividing by K_{tot},

and using equation 2.4 gives

$$f_{\text{rad}} \propto f_{\text{new}}(1 + f_{\text{k}}) \propto \ f_{\text{g}} \ f_{\text{k}} \ (1 + f_{\text{k}}). \qquad (2.6)$$

This expression is plotted in Figure 2.5 against the actual radiative energy losses in our

simulations, showing a crude proportionality, with the proportionality constant ~ 0.4.

25

2.3.3   A Dissipative Model for Remnant Radii

Guided by this toy model for dissipative losses during a galaxy merger, we construct a modified energy conservation equation for predicting remnant radii. Note that the final stellar mass can be computed using the initial mass and the equation for star formation (2.4). We choose to include in our energy formula the initial stellar mass plus the mass of the stars formed during the merger, such that the dissipative term tracks the loss of energy of the progenitor's gas that becomes stars in the remnant. The energy equation is

$$E_{\mathrm{int,f}} = E_{\mathrm{int,i}} + E_{\mathrm{rad}} + E_{\mathrm{orb}}, \tag{2.7}$$

where the final and initial internal energies are

$$E_{\mathrm{int,f}} = -\frac{C_{\mathrm{int}} G (M_1 + M_2 + M_{\mathrm{new,1}} + M_{\mathrm{new,2}})^2}{R_{\mathrm{f}}} \tag{2.8}$$

$$E_{\mathrm{int,i}} = -C_{\mathrm{int}} G \left[\frac{(M_1 + M_{\mathrm{new,1}})^2}{R_1} + \frac{(M_2 + M_{\mathrm{new,2}})^2}{R_2} \right], \tag{2.9}$$

and M_1, M_2, R_1, and R_2 are the initial stellar masses and the corresponding three-dimensional half-mass radii of the progenitors, R_{f} is the final three-dimensional half-mass radius of the remnant, and $M_{\mathrm{new,1}}$ and $M_{\mathrm{new,2}}$ are the mass of new stars formed during the merger in galaxies one and two respectively, as predicted by our model. The constant structural parameter, which relates the internal energy of the systems to GM^2/R, is determined by best fit to the radii of the simulated remnants to be $C_{\mathrm{int}} \simeq 0.5$. In assuming homology, we set the structural constants for the progenitors and remnants to the same value.

The radiated energy term is the sum of the losses from the two progenitors,

$$E_{\mathrm{rad}} = -C_{\mathrm{rad}}\Sigma_{i=1}^{2}K_i f_{\mathrm{g},i} f_{\mathrm{k},i}(1 + f_{\mathrm{k},i}), \qquad (2.10)$$

where K_i, $f_{\mathrm{g},i}$ and $f_{\mathrm{k},i}$ are the initial internal kinetic energy, gas fraction and impulse corresponding to progenitor i. The constant of proportionality relating our expression for energy loss to the actual energy lost is determined by best fit to the radii of the simulated remnants to be $C_{\mathrm{rad}} \simeq 1.0$.

The orbital energy is:

$$E_{orb} = -\frac{G(M_1 + M_{\mathrm{new},1})(M_2 + M_{\mathrm{new},2})}{R_{\mathrm{sep}}}$$
$$+\frac{1}{2}(M_1 + M_{\mathrm{new},1})V_1^2 + \frac{1}{2}(M_2 + M_{\mathrm{new},2})V_2^2$$

where R_{sep}, the distance between the progenitors' centres of mass, and V_1 and V_2, the centre of mass velocites of each progenitor, are defined at the beginning of the encounter. Most of our simulations are nearly parabolic, such that this term is close to zero.

Our model predictions for the remnant radii are plotted against the actual stellar half-mass radii of the simulated merger remnants in Figure 2.6. The overall scatter is $S = 0.21$, which is a significant improvement over the dissipationless model. There is no obvious systematic error, and the fit is good both for the wide range of progenitor properties and for the different choices of orbital parameters. The spread for a particular progenitor type results from differences in orbit and orientation. For most cases this orbital spread is well fit by the model. This is particularly evident with the D and Y series, for which only orbit is varied and not orientation. The spread in Sbc series is not quite as closely tracked by the model. This additional spread is the

result of differing orientations. Orientation is not taken into account in the model for reasons described in §2.5.2. We note that the performance of the final model for radii is somewhat better than what might have been expected from the quality of the prediction of radiative losses, shown in 2.5. However, this is not as surprising if one remembers that radiative losses are only a correction on the non-dissipative model. Even if this correction is not exact, it always acts in the proper direction and makes the remnants more compact.

2.3.4   Velocity Dispersion

Naab et al. (2006) have shown that the kinematics of merger remnants change as a function of initial gas fraction. When predicting the central velocity dispersion of merger remnants we take gas fraction into account in two ways: first by using the gas fraction dependent predicted radius, and second by adjusting the central dark matter fraction to account for the rearrangement of gas and subsequent formation of new stars. In order to compute the stellar velocity dispersion of the merger remnants, we implement a virial relation of the type

$$\sigma^2 = C_{\mathrm{vir}} \frac{GM_{\mathrm{dyn}}}{R}, \tag{2.11}$$

where M_{dyn} is the dynamical mass of the system. This mass includes all of the stellar mass of the system and also a contribution from the dark matter near the centre of the galaxy. C_{vir} is a constant that varies slightly with galaxy structure and also accounts for the conversion between the three-dimensional radius and the projected, two-dimensional velocity dispersion. R is a characteristic radius (e.g., the stellar half-mass radius). σ

28
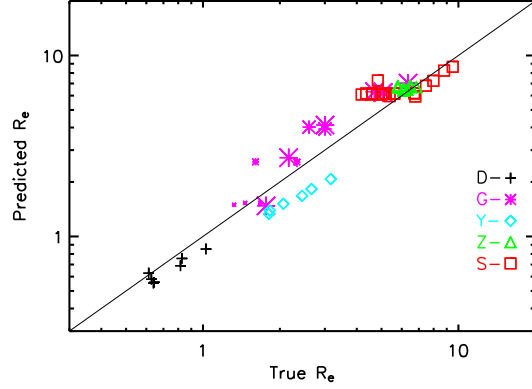
(a)
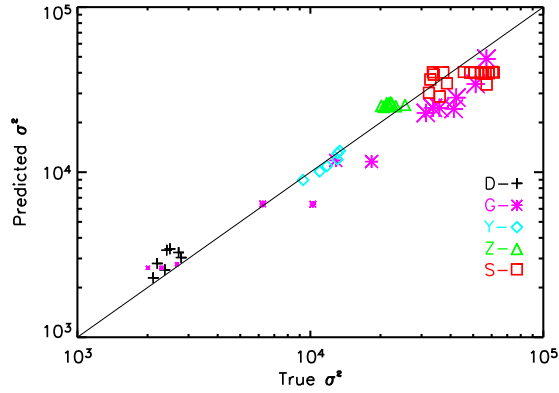
(b)

Figure 2.6: The model predictions for radius (a) and velocity dispersion (b) versus the actual values. Predicted R_e and True R_e are the predicted and simulated values of the three-dimensional stellar half-mass radius of the remnants, respectively. σ is the line-of-sight velocity dispersion inside the projected half-mass radius. The scatter is $S = 0.21$ for the radius prediction and $S = 0.24$ for σ^2.

is a line-of-sight velocity dispersion of stars inside the projected half-mass radius. We measure this from the simulations by averaging over 50 random projections.

Given the predicted values for R_f and the final stellar mass, one may attempt to estimate σ^2. However, variations in central progenitor dark matter fractions and differing amounts of star formation result in significantly different ratios of M_{dyn} to the total stellar mass in the remnants. Because we are dealing with an approximate virial relation of a system that actually is not completely self-gravitating, it is not obvious from first principles what the exact contribution to M_{dyn} from dark matter should be. We track the dark matter contribution by estimating the dark-matter fraction for each remnant. Therefore the uncertainty above, concerning which dark matter mass to include, translates into an uncertainty in which radius to choose for defining a dark-matter fraction. Because we use the three-dimensional stellar half-mass radius in our virial relation, it would be reasonable to choose a radius $\sim R_f$. However, one can pick a range of radii and still achieve sensible results by making slight adjustments to C_{vir}. We find the best results when we focus on the dark matter fraction inside *half* of the three-dimensional stellar half-mass radius. We define the dark-matter fraction within a given radius by

$$f_{dm} = \frac{M_{dm}}{(M_{dm} + M_{stars})}, \tag{2.12}$$

where M_{dm} and M_{stars} are the dark matter and stellar masses inside that radius, respectively. Much of the variation in the remnant dark matter fraction, $f_{dm,f}$, is due to the variation in initial dark-matter concentrations and baryon distributions. However, another important effect is the tendency of new stars to form near the galaxy centre,

causing mergers that form more stars to end up with lower $f_{\mathrm{dm,f}}$ values. We thus predict the final dark-matter fraction using the initial dark matter masses and our model prediction for the mass in new stars,

$$f_{\mathrm{dm,f}} = \frac{M_{\mathrm{dm,1}} + M_{\mathrm{dm,2}}}{M_{\mathrm{dm,1}} + M_{\mathrm{dm,2}} + C_{\mathrm{stars}}(M_1 + M_2 + M_{\mathrm{new}})}. \tag{2.13}$$

$M_{\mathrm{dm,1}}$ and $M_{\mathrm{dm,2}}$ are the dark matter masses inside half of the three-dimensional stellar half-mass radii of the progenitors. M_1 and M_2 are the stellar masses of the progenitors, and M_{new} is the total mass of stars formed during the merger as predicted by equation 2.4. This expression simply assumes that the inner region of the remnant contains the same amount of dark matter as the sum of the inner regions of the progenitors, and that a fixed fraction, C_{stars}, of the final stellar mass is inside one-half of the three-dimensional stellar half-mass radius. We find that the best fit to the simulated remnants is $C_{\mathrm{stars}} \simeq 0.35$.

Our modified virial relation becomes

$$\sigma^2 = C_{\mathrm{vir}} \frac{G(M_1 + M_2 + M_{\mathrm{new}})}{R_{\mathrm{f}}(1 - f_{\mathrm{dm,f}})}. \tag{2.14}$$

The best-fitting value from our simulations is $C_{\mathrm{vir}} \simeq 0.30$. The model predictions for the stellar line-of-sight velocity dispersions are shown in Figure 2.6, in comparison with the simulated values. The scatter in σ^2 is $S = 0.24$, and the overall performance is similar to that of the model for the final radii. There are no obvious systematic errors, and the predictions properly capture the variations due to either progenitor properties or orbital parameters.

31

2.4   Unequal Mass Mergers

The cases studied so far were mergers of identical galaxies, and the model was built using the simulations of these cases. However, most mergers in the universe are of unequal mass galaxies. More recent simulations were run of unequal mass mergers (Cox et al., 2008b), and given the importance of unequal mass mergers in the real universe we here examine the accuracy of our model for different progenitor mass ratios. For this study we used simulations of unequal mass mergers from the G series of galaxies (Cox et al., 2008b). These mergers cover a range of mass ratios and a variety of orbital parameters. For unequal mass mergers, the predictions of remnant properties remain relatively accurate with $S = 0.13$ about the previously fit relation for radii, and $S = 0.20$ for σ^2 (see Figure 2.7). Note that in some cases the spread does not fall directly along the line. This is the result of a number of simulations with the same progenitors and orbital parameters, but with different orientations of the progenitors with respect to the orbital plane. Variations due to orientation do not have clear enough systematics to be accounted for in the model. We discuss this limitation in §2.5.2.

In major mergers, which have mass ratios greater than 1:3, the gas disks of the galaxies are severely disrupted, and we see large flows of gas toward the galactic centres. However, in minor mergers, which have mass ratios less than 1:3, these flows are much less pronounced because the gas disk of the larger progenitor is only modestly disrupted. For example, central gas densities in a major merger of two G3 galaxies reach values roughly four times that of a minor merger (1:6) of G3 and G1 galaxies on

the same orbit. Hence, dissipation is expected to be much less important in the centres

of the big progenitors of minor mergers. Our model captures this effect through the

impulse dependence of the radiation term. For minor mergers where $M_{\text{big}} \gg M_{\text{small}}$, the

radiation term becomes insignificant in comparison to the internal energy term. It is also

worth noting that the the star formation equation (2.4) under predicts star formation

in the smaller progenitor in this extreme minor merger regime. However, this has little

effect on the predictions of remnant properties since the mass of new stars formed in a

much smaller progenitor is much smaller than the mass of the larger progenitor.

2.5 Caveats

2.5.1 Feedback

Arguably the largest uncertainty in the physics of our simulations is in the

prescription for feedback. The merger simulations fit by our model all use the same

prescription for feedback with the same parameters, hence, it would be useful to vary

these feedback parameters and examine the effect on our model. The feedback recipe is

characterized by two parameters: feedback efficiency and an equation of state parameter,

n, which sets the polytropic index. The effective pressure is

$$P_{eff} \sim \rho^{1+(n/2)}. \tag{2.15}$$

We explore three equations of state, $n = 0$, $n = 1$, and $n = 2$, where $n = 0$

corresponds to an isothermal equation of state and $n = 2$ results in a stiff equation of
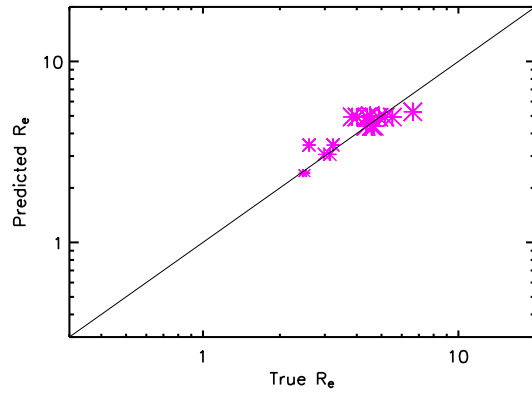
(a)
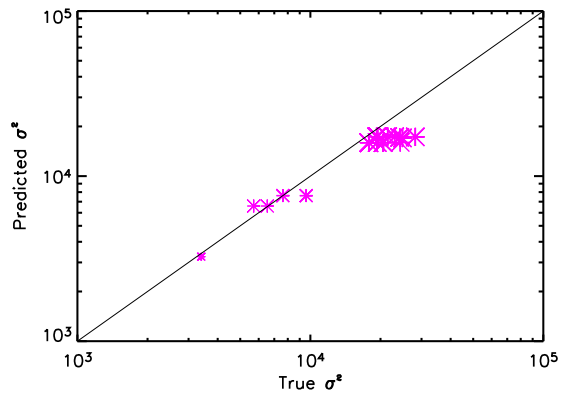
(b)

Figure 2.7: Unequal Mass Mergers. The predicted values of our radius and velocity dispersion models versus the actual values for unequal mass mergers of G series galaxies. $S = 0.13$ for radius, and $S = 0.20$ for σ^2.

state. The feedback efficiency determines how quickly the feedback energy is allowed to thermalize. Higher efficiencies result in a quicker dissipation of the feedback energy. For each value of n, we examine two different values of efficiency. As a lower limit, we use a low efficiency value that gives just enough pressure to stabilize the disk. We also simulate cases of super-stable disks where the efficiency is set to ten times that needed for disk stabilization. In table 2, labels of the feedback parameter sets denote the values of n and efficiency chosen. Unstable cases with even lower feedback efficiency were run but are not discussed here. Thus, for consistency our "low" efficiency cases are labeled "med"(e.g. *n2med* means $n = 2$ and the feedback efficiency is low). In general, with lower feedback, the maximum star formation rate is higher, but the starburst duration is shorter. For a more detailed description of our feedback model see Cox et al. (2006, 2008b).

To examine the effects of feedback on our remnant model, we take the fiducial Sbc merger and simulate identical initial conditions with varied values of the feedback parameters. As expected, feedback has a significant effect on star formation. The effect is twofold. First, both increased feedback efficiency and, to a smaller extent, stiffer equations of state (higher n) decrease the total number of stars formed. This can be a dramatic effect. As shown in Table 2.3 the total number of stars formed varies by more than a factor of three. Secondly, feedback can change the radial distribution of stars formed. A stiffer equation of state will lead to more stars being formed at large radii (Cox et al., 2006).

Both of these effects can act in concert to increase the size of the merger

Table 2.3: Effect of differing feedback parameters on remnant properties. All simulations in the table are variations of a fiducial Sbc merger. M_{newstars} is the total mass in new stars formed during the 3 Gyr simulation, burst and quiescent. $R_{\mathrm{f},1/2}$ is the stellar *three-dimensional half-mass radius* of the remnant. σ_{f} is the velocity dispersion of the remnants measured inside of the *projected half-mass radius* averaged over 50 random projections.

Model	M_{newstars} $(10^{10}\mathrm{M}_\odot)$	$R_{\mathrm{f},1/2}$ (kpc)	σ_{f} (km s^{-1})
n0med	5.75	5.37	253
n0high	2.68	5.72	218
n1med	5.30	5.34	252
n1high	2.57	5.75	190
n2med(fiducial)	5.03	5.62	225
n2high	1.61	6.95	178

remnant. However, the effect is weak enough that it takes both high feedback efficiency and a stiff equation of state to significantly alter the final half-mass radius (see Figure 2.8). In our set of feedback models, the only model for which the radius is significantly different than the others is *n2high*. Even in this model the remnant radius is only a factor of ~ 1.3 larger than the most compact remnant. Differences in radius and compactness will also affect the central velocity dispersion. Higher efficiency and stiffer feedback models produce somewhat lower σ. This effect is similar in magnitude to the effect on radius, with a factor of ~ 1.4 between the largest and smallest σ. For velocity dispersion, our fiducial model lies near the centre of the distribution (see Figure 2.8). These differences are roughly comparable to the scatter in our remnant model.

While we have chosen a specific feedback model as a fiducial, and used it to run most of our cases, we note that there are currently no theoretical or observational motivations for this choice. Feedback in the real universe could resemble any of these
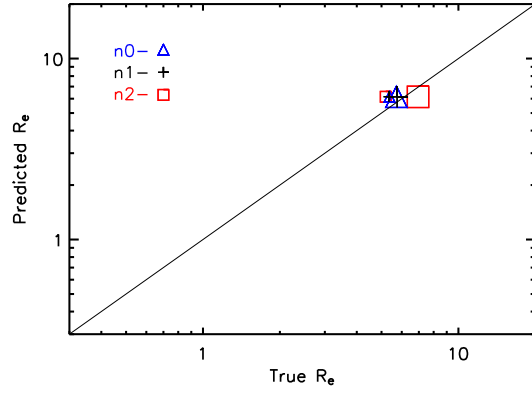
(a)
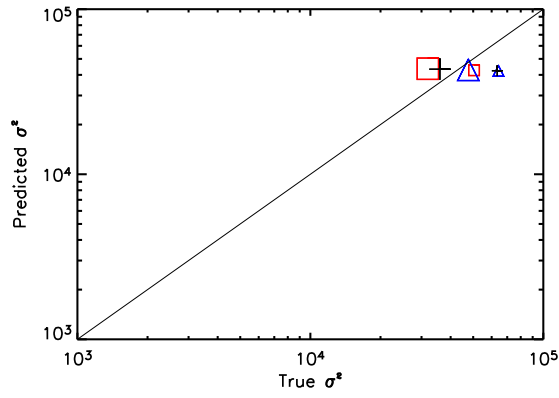
(b)

Figure 2.8: Various feedback models. The predicted values of radius (a) and velocity dispersion (b) for all of the variations on the feedback model. Large symbols represent high feedback efficiency, small symbols represent low efficiency, and squares, crosses, and triangles represent n=2, n=1, and n=0 respectively.

37

models. If feedback in the real universe is significantly different from our fiducial case, then it is possible that the parameters of our model would require some tuning. C_{new} is the parameter most affected by differing feedback. The variations in star formation suggest that C_{new} could vary roughly from 0.1 to 0.35. It is also possible that the structural parameters C_{int}, C_{vir}, and C_{stars} would need to be adjusted. However, aside from the mass of new stars, the relatively drastic changes in feedback produce relatively minor changes in remnant properties. This suggests that any tuning needed to match the real universe would be small. Further verification of the model will require testing with independent feedback recipes.

2.5.2   Orbits

There are several potential sources of uncertainty concerning our treatment of the initial orbits of the progenitors. The first regards the orbital energy term in our energy conservation equation. Cole et al. (2000a) assume in their dissipationless model that some of the orbital energy is transferred to the outer dark matter halo through dynamical friction. In order to estimate the energy transferred from the orbit to the baryonic remnant, they assume that the two galaxies come into a circular orbit at a radius that equals the sum of their half-mass radii. However, the orbits in our simulations actually tend to quickly radialize after the first close passage. We therefore adopt the better approximation that all the orbital energy ends up in the baryonic remnant. This too may be an over-simplification, as the energy deposited in the dark halo is likely to depend on the initial eccentricity of the orbit, and may get larger for

increasingly tangential orbits. Unfortunately, our suite of simulations is not particularly well-suited to exploring this dependence, as most of them start with initial orbital eccentricities close to unity. Our suite does contain three Sbc simulations and one Z simulation with $e = 0.8$, and also one unequal mass merger, a G3-G2, with an initially circular orbit, $e = 0$. We find that these few cases are well fit by our model as is. However, given our limited sampling of non-radial orbits, we keep in mind that our orbital-energy term may require some modification. On the other hand, we note that statistical studies of cosmological merger orbits suggest that they tend to be rather radial (Benson, 2005; Khochfar & Burkert, 2006), and that all attempts we made to include a term for energy transfer to the dark matter did not significantly improve the model.

A second potential concern is the initial orbital parameters we use. Our simulations typically start when the centre of one galaxy is near half of the virial radius of the other galaxy, whereas the typical analysis of halo orbits in N-body simulations refer to orbits at the virial radius (Benson, 2005; Khochfar & Burkert, 2006). Furthermore, our simulations involve the final entry into this radius, whereas in cosmological situations many of the halos enter and leave the virial radius more than once before merging. One practical concern is how to convert between orbits at $0.5\,R_{\rm vir}$ and at $R_{\rm vir}$. Dynamical friction undoubtedly induces some evolution in the orbital parameters as the galaxies fall between $0.5\,R_{\rm vir}$ and $R_{\rm vir}$. This effect should be evaluated using cosmological N-body simulations.

Finally, our model does not take into account the effect of the initial orientation

of the progenitors with respect to the orbital plane. Our suite of simulations does include a number of different initial orientations, including both prograde and retrograde encounters. Previous authors have observed systematic differences between encounters with different orientations (Naab et al., 2006; Barnes, 2002), but the effects on the remnants in our simulations do not show clear enough systematics for us to effectively characterize them. The performance of the model could be improved by including a term that depends on orientation, but the modest improvement did not seem to justify the inclusion of yet another parameter that would increase both the complexity of the model and the risk that the model is over-fit.

2.5.3   Gas Fraction

Our merger suite primarily consists of disky progenitors with high gas fractions. It is possible that we are missing some of the effects that dominate the results of dry mergers of spheroids. For example, Boylan-Kolchin et al. (2006) find that more radial encounters of dry ellipticals result in larger remnants. However, we see no evidence for such a trend, not even in our lowest gas fraction simulations, the Z series, where $M_{gas}/M_{baryon} = 0.1$. In fact, for these low-gas cases, we see essentially no systematic trend of remnant size with orbit, and a generally smaller scatter in remnant size. We conclude that if we miss any effect of this sort, it is likely to be small. Apparently, the dissipationless energy conservation equation becomes a relatively accurate approximation in the limit of low gas fraction, and our model converges to the dissipationless model when the progenitors are gas-free.

Another limitation of our model is that it is unlikely to apply to extremely gas-rich mergers, where $M_{\mathrm{gas}} \gg M_{stars}$. For such cases the initial energy term should account for the size of the gas disk, whereas our model only takes into account the initial size of the stellar disks. The highest gas fraction case that we include has a ratio of $M_{\mathrm{gas}}/M_{\mathrm{stars}} = 3.1$. For the cases that we simulate, where $M_{\mathrm{gas}} \lesssim M_{\mathrm{stars}}$ we find that the final sizes are relatively insensitive to the initial sizes of the gas disks. Specifically, our suite includes cases where the gas disk scale length is equal to the stellar disk scale length and cases where the gas disk scale length is three times the stellar disk scale length. Both of these cases are well fit by our model.

One final note is that our merger simulation suite does not attempt to model galaxies at higher redshift by systematically changing gas fraction and concentration as has been done in other studies (Robertson et al., 2006). Since progenitors are primarily modeled after low-redshift galaxies, this is the regime where the model is most well-calibrated. However, the model is based on simple physical principles and is robust to systematic changes in gas and bulge fraction. We see no obvious reason why it should not apply to binary mergers at higher redshifts.

2.6   Conclusions

We have developed a simple toy model for the physical processes involved in wet mergers of galaxies, and have calibrated it using a suite of hydrodynamical merger simulations. This modeling helped us to gain a better understanding of these pro-

cesses, and provides a practical semi-analytic recipe for predicting post-merger galaxy properties in SAMs.

Crude models of this sort have been used by Cole et al. (2000a), Hatton et al. (2003), and Shen et al. (2003), but these models did not account for energy losses through dissipative processes, and they have not been calibrated against realistic merger simulations. Using a suite of merger simulations, we have demonstrated the key role of dissipative energy losses in determining the final radii and velocity dispersions of merger remnants. We found that the dissipative effects depend on the initial orbits of the progenitors. More violent, lower angular momentum orbits create greater disturbances in the gas disks, which in turn radiate more energy and produce more stars. This orbital "violence" can be parameterized through an impulse approximation for energy exchange between the orbital and internal components during the first close pass of the encounter.

We present a physically-motivated, simulation-calibrated model that is capable of predicting star formation, central dark matter fraction, remnant radius and remnant velocity dispersion, given the properties of the progenitors and the initial orbital parameters of a merger.

The non-dissipative energy conservation model often predicts radii that are off by a factor of $\sim 2 - 3$, and it does not reproduce the spread due to orbital variations. Our model, which accounts for the dissipative energy losses, results in only $\sim 25\%$ errors in the predicted radius and velocity dispersion when a wide variety of progenitor types is considered. For a given progenitor type, the error in remnant properties is reduced to $\sim 10\%$, indicating that our model correctly captures the variation of remnant properties

due to merger orbit.

Since we used the whole available simulation suite to calibrate our model, via a few proportionality constants of order unity, a proper evaluation of the model performance is yet to be pursued using an independent suite of simulations.

2.7 Appendix A: Impulse Approximation

A number of previous researchers have studied and parameterized the transfer of orbital to internal kinetic energy during galaxy encounters (Richstone, 1975; Dekel et al., 1980; Aguilar & White, 1985). Binney & Tremaine (1987) summarize these studies and present formulas for impulse approximations valid in the tidal and radial cases. Aguilar & White (1985) find that the tidal approximation breaks down at approximately $5R_e$, but that a smooth interpolation between the two cases gives an approximate fit to actual energy transfers:

$$Tidal\ case: \Delta E = \frac{2G^2 M_1 M_2^2 \bar{r^2}}{3R_{\mathrm{peri}}^4 V_{\mathrm{peri}}^2} \tag{2.16}$$

$$Radial\ case: \Delta E = \frac{3G^2 M_1 M_2^2}{3V_{\mathrm{peri}}^2 a^2} \tag{2.17}$$

M_1 and M_2 are the masses of the perturbed and perturbing galaxies respectively, and R_{peri} and V_{peri} are the pericentric distance and velocity. For the tidal case, $\bar{r^2}$ is the mean-square radius of the perturbed galaxy. A Plummer model, $\Phi = -GM/\sqrt{r^2 + a^2}$, is assumed for the radial approximation.

We measure the change in internal kinetic energy of each progenitor during the first close encounter and define this as our "impulse." In order to compare with the above

approximations we assume that the galaxies are point masses and use values of R_{peri} and V_{peri} calculated at the beginning of the simulations. The impact parameters simulated in our suite all fall well within $5R_{\mathrm{dm}}$, as might be expected for *merger* orbits. Consequently, the tidal approximation performs quite poorly at predicting the impulse. Furthermore, any impulse approximation assumes that the dynamical time of the perturbed galaxy is much less than the time of the encounter. However, if two galaxies are going to merge, then the encounter velocity is typically of the same order as the internal velocity of the larger galaxy. Therefore, it is not clear that either impulse approximation above would apply. We compared the radial approximation, and several similar functions that included a dependence on impact parameter, to the measured impulses and found that they did not provide satisfactory fits.

However, we do find that the measured impulse, during an encounter with orbital parameters within our range of simulated values, is well-fit by the following formula:

$$\Delta E = \frac{AG^2 M_{1,\mathrm{tot}}^2 M_{2,\mathrm{tot}}}{V_{\mathrm{peri}}^2 (R_{\mathrm{peri}}^2 + B\ R_{1,\mathrm{tot}}\ R_{\mathrm{peri}} + C\ R_{1,\mathrm{tot}}^2)}, \tag{2.18}$$

where $M_{1,\mathrm{tot}}$ and $M_{2,\mathrm{tot}}$ are the total mass of the perturbed and perturbing galaxies respectively, baryons plus dark matter, and $R_{1,\mathrm{tot}}$ is the total half mass radius of the perturbed galaxy. The parameters are set by best fit to the simulation results with $A = 1.6$, $B = 1.0$, and $C = 0.006$.

For a radial orbit, this formula vaguely resembles the radial approximation. However, the mass dependence of the formula is different. In the radial impulse approximation $\Delta E \propto M_1 M_2^2$, whereas in our formula $\Delta E \propto M_1^2 M_2$. This suggests that

the impulse approximation is breaking down, that we cannot simply assume that the potential of the perturbed galaxy is constant during the encounter. At intermediate impact parameters, where $R_{\mathrm{peri}} < R_{1,\mathrm{tot}}$, the fitting formula falls off as $1/R_{\mathrm{peri}}$. At larger impact parameters, $R_{peri} > R_{dm}$, it falls off as $1/R_{peri}^2$. The parameter C sets the cutoff radius at which the impulse ceases to increase with decreasing impact parameter and approaches the constant radial case. The fit of C is somewhat tenuous since our simulations do not actually probe the range of $R_{peri}^2 < CR_{dm}^2$. However, these cases are so radial that the probability of such encounters is low, and the effects of small changes in C are likely to be insignificant. Our suite probes a range of roughly $0.1R_{1,\mathrm{tot}} < R_{\mathrm{peri}} < 2R_{1,\mathrm{tot}}$ and $2\sigma_{\mathrm{prog}} < V_{\mathrm{peri}} < 10\sigma_{\mathrm{prog}}$, where σ_{prog} is the initial velocity dispersion of the larger progenitor. The formula is plotted against impulses measured from our simulations in Figure 2.3. This plot includes both equal and unequal mass mergers. The fit is valid over a range of progenitor mass distributions. Specifically, the structure of the fitted galaxies varies widely with a variety of bulge fractions and dark matter concentrations.

2.8   Appendix B: Summary of the Model

The model presented requires the integration of formulas and ideas found throughout the paper. Hence, for pragmatic purposes, we present a brief summary of the model for the reader who wishes to implement it as a recipe within a semi-analytic model of galaxy formation. In Figure 2.9 we illustrate the outline of the model.

Table 2.4: Definitions of the inputs used in the model.

Name	Definition
Inputs	
$M_{\mathrm{tot},1}, M_{\mathrm{tot},2}$	The total masses (baryonic plus dark) of galaxies 1 and 2 respectively.
$R_{\mathrm{tot},1}, R_{\mathrm{tot},2}$	The three-dimensional half-mass radii of the total masses (baryonic plus dark) of galaxies 1 and 2 respectively.
$V_{\mathrm{peri}}, R_{\mathrm{peri}}$	The theoretical pericentric velocity and distance of the first encounter, defined when the galaxies are separated by $\sim R_{vir}$.
$K_{\mathrm{tot},1}, K_{\mathrm{tot},2}$	The total kinetic energies of the galaxy/halo systems of galaxy 1 and 2 respectively. In our simulations $K_{\mathrm{tot},1} \simeq 0.35\ GM_{\mathrm{tot},1}^2/R_{\mathrm{tot},1}$ with very little scatter.
$f_{\mathrm{g},1}, f_{\mathrm{g},2}$	The gas fractions of galaxies 1 and 2, defined as (gas mass)/(total mass).
R_1, R_2	The stellar three-dimensional half-mass radii of galaxies 1 and 2.
M_1, M_2	The stellar masses of galaxies 1 and 2.
$M_{\mathrm{dm},1}, M_{\mathrm{dm},2}$	The dark matter mass inside 1/2 the stellar three-dimensional half-mass radius of galaxies 1 and 2 respectively.
$M_{\mathrm{stars},1}, M_{\mathrm{stars},2}$	The stellar mass inside 1/2 the stellar three-dimensional half-mass radius of galaxies 1 and 2 respectively.

Table 2.5: Definitions of the parameters used in the model.

Name/Value	Description
Parameters	
$A = 1.6$ $B = 1.0$ $C = 0.006$	Parameters fit to match the impulse model to the simulations. See Appendix A.
$C_{\text{new}} = 0.3$	Proportionality constant in star formation equation. Determines mass of new stars.
$C_{\text{int}} = 0.5$	Structural constant which sets relative weighting of internal energy.
$C_{\text{rad}} = 1.0$	Constant which sets relative weighting of radiated energy.
$C_{\text{sig}} = 0.30$	Structural constant which sets proportionality of σ^2 to M/R in remnants.
$C_{\text{stars}} = 0.35$	Sets fraction of stars within $1/2$ of the half-mass radius of the remnants.

Table 2.6: Definitions of the outputs used in the model.

Name	Definition
Outputs	
M_{f}	Mass of stars in the remnant (old + burst).
R_{f}	Stellar three-dimensional half-mass radius of remnant.
$f_{\text{dm,f}}$	The dark matter fraction inside $1/2$ of R_{f}
σ_{f}	The stellar velocity dispersion of the remnant inside the projected half-mass radius.

The relevant equations are included, except for the definitions of the energy terms in the conservation equation. For these, we refer the reader to the list in §2.3.3. Inputs, parameters, and outputs are defined in Tables 2.4, 2.5, and 2.6.

The general flow of the model is as follows:

1. Use orbits and masses to calculate impulse.

2. Use impulse and gas fraction to calculate new stars formed in the burst.

3. Use mass of new stars and properties of progenitors to calculate radius.

4. Use initial dark matter fraction and final mass of stars to calculate remnant central dark matter fraction.

5. Use central dark matter fraction and radius to calculate velocity dispersion.
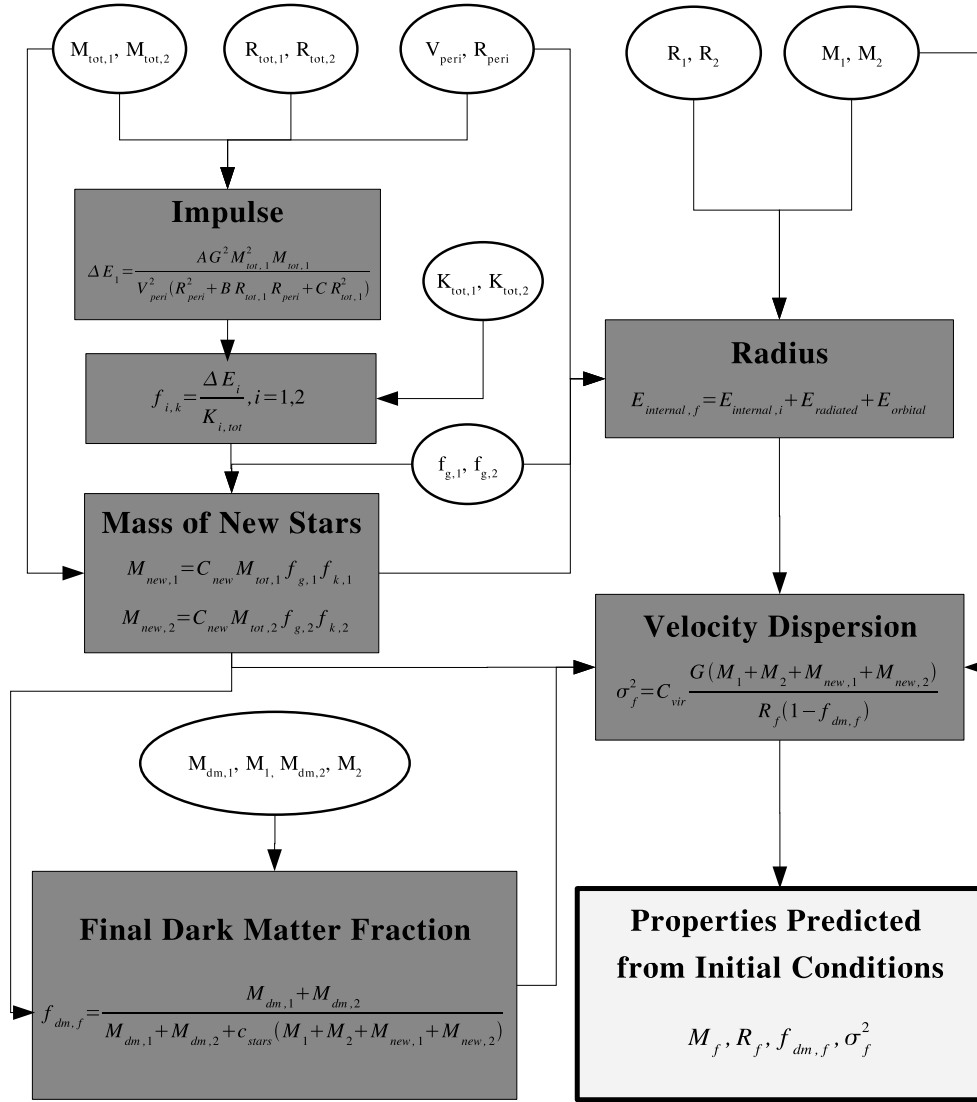
Figure 2.9: Summary of the inputs (ovals), outputs (white rectangle), and equations (shaded rectangles) needed to implement the merger model.

Chapter 3

The Evolution of Early-Type Galaxy

Scaling Relations in Semi-Analytic

Models

3.1 Introduction

The merging of disk galaxies is one of the main hypothesized mechanisms for the formation of elliptical galaxies. Simulations have shown that mergers of disks with similar masses effectively disrupt the ordered rotation in the disks and convert it into random velocity support, creating merger remnants that appear similar to observed elliptical galaxies (Toomre & Toomre, 1972; Toomre, 1977; Barnes & Hernquist, 1992; Mihos & Hernquist, 1994a). Furthermore, the ΛCDM cosmology predicts the hierarchical buildup of galaxies through a sequence of mergers. These results suggest that merging is a likely mechanism for producing elliptical galaxies.

However, observed ellipticals follow a number of scaling relations, including relatively tight relations between stellar mass and velocity dispersion, the Faber-Jackson Relation (Faber & Jackson, 1976), and between size and stellar mass (Kormendy, 1977). Furthermore, observed ellipticals fall in a tight plane, the fundamental plane (FP), in the three-dimensional space of stellar mass, size, and velocity dispersion (Djorgovski & Davis, 1987; Dressler et al., 1987). Recent studies of the Sloan Digital Sky Survey (SDSS) have provided excellent statistics on these scaling relations in the local universe (Shen et al., 2003; Bernardi et al., 2003a,b; Padmanabhan et al., 2004; Gallazzi et al., 2006), and studies using high redshift surveys have provided evidence for the evolution of these relations over cosmological time (Barden et al., 2005; McIntosh et al., 2005; Trujillo et al., 2006). If mergers are a major mechanism for producing elliptical galaxies then they must be able to produce the correct scaling relations as well as the evolution of

scaling relations over time. Theoretical studies have shown that simulations of gas-rich galaxy mergers are capable of reproducing the observed scaling relations of elliptical galaxies if the correct progenitor properties are used (Robertson et al., 2006; Hopkins et al., 2008). This is a step toward verifying the production of scaling laws through mergers, but current computing power only allows the simulation of relatively small numbers of mergers and the space of possible merger initial conditions and progenitor properties is quite large. Furthermore, these simulations are not placed within a cosmological context, making it more difficult to explore in detail the origin and evolution of scaling relations.

Currently, the primary tool for studying the evolution of statistical samples of galaxies over cosmological scales is Semi-Analytic Modeling (Kauffmann et al., 1993; Cole et al., 1994; Somerville & Primack, 1999; Hatton et al., 2003; Croton et al., 2006). These models combine dark matter halo merger trees with analytic recipes for populating the halos with galaxies. However, Semi-Analytic Models (SAMs) do not currently incorporate realistic formula for predicting the properties of the remnants of galaxy mergers. We recently developed a physically motivated analytical model for predicting the properties of merger remnants (Covington et al., 2008). The parameters in this new merger model were calibrated using a suite of galaxy merger simulations (see Section 3.2). Here we implement this model using post-processing of merger outputs from the SAMs developed by Somerville et al. (2008) and Croton et al. (2006). This provides a rich population of tens of thousands of merger remnants over a large range of redshifts ($0 < z < 3$) complete with predicted values of size, stellar mass, and velocity dispersion.

Comparison of the modeled population of ellipticals with the observed scaling relations provides an important test of the merger hypothesis as well as physical insight into the origin and evolution of these relations via merging.

3.2   Methodology

We use a combination of modeling approaches to create a theoretical framework for predicting the evolution of early-type scaling relations over cosmological time. In previous work, the authors developed a large suite of hydrodynamical galaxy merger simulations (Cox, 2004; Cox et al., 2006, 2008a). These simulations were performed using the N-body/SPH code GADGET (Springel et al., 2001), and include hydrodynamics, star formation, and stellar feedback. The simulation suite contains mergers with a wide variety of progenitor properties, mass ratios and merger orbits. Variations in progenitor properties include a range of stellar masses, gas fractions, dark matter halo concentrations, bulge fractions, baryonic fractions, and gas disk sizes.

In subsequent work, Covington et al. (2008, hereafter C08) constructed a physically-motivated analytic galaxy merger model capable of predicting the half-mass radii, stellar masses, and velocity dispersions of galaxy merger remnants given the properties of the progenitor galaxies and the initial orbits of the mergers. This model was calibrated using the galaxy merger suite described above. Unlike previous similar models (Cole et al., 2000a; Hatton et al., 2003), this model includes the effects of star formation and energy loss due to dissipation. Here we combine this new galaxy merger model with

several semi-analytic models (SAMs) in order to explore the creation and evolution of the scaling relations of early-type galaxies.

3.2.1 Description of the Merger Model

For a detailed description of the galaxy merger model used, we refer the reader to C08. However, for completeness we include a brief summary here. Previous models for predicting the sizes and velocity dispersions of galaxy merger remnants employed a combination of energy conservation and the virial theorem (Cole et al., 2000a; Hatton et al., 2003). Assuming homology between progenitors and remnants then allows a straightforward calculation of remnant properties. However, the most common mergers are "wet" mergers of gaseous galaxies, and the approach used previously does not account for energy losses due to gas processes. Recent work has suggested that these dissipative effects play an important role in the formation of elliptical galaxies (Cox et al., 2006; Robertson et al., 2006; Dekel & Cox, 2006; Ciotti et al., 2007; Cox et al., 2008a; Hopkins et al., 2008). C08 develops a framework for modifying the energy conservation approach to include dissipative losses due to gas processes.

In order to account for dissipative losses, we include a radiated energy term within the energy conservation equation. Furthermore, since stars form during the merger, we include the mass of gas that will form stars when calculating the internal energies of the progenitor galaxies. C08 found that the energy lost and the number of new stars formed are a function of both the gas fraction and the initial merger orbit. Closer, more disruptive encounters will result in greater total energy losses and larger

numbers of stars forming. Orbital impulse of the initial encounter is used to quantify how disruptive a particular merger orbit is.

Remnant properties are calculated as follows (summarized in Figure 3.1):

1. The total masses (baryonic and dark matter), the total half-mass radii (baryonic and dark matter), and the initial orbital parameters are used to calculate the impulses on each galaxy during the first encounter.

2. The impulses are converted into a dimensionless quantity (f_k) by dividing by the initial total kinetic energies of the baryon/dark matter system.

3. The dimensionless impulse and gas mass are used to calculate the mass of new stars formed in each galaxy via the relation $M_{\mathrm{new}} = C_{\mathrm{new}} M_{\mathrm{gas}} f_k$. C_{new} is a parameter that is calibrated to the simulations. For our fiducial feedback model $C_{\mathrm{new}} = 0.3$, however the exploration of various feedback parameters in the simulations suggests that a range of roughly 0.1 to 0.4 would be reasonable.

4. The stellar half-mass radii and stellar masses of the two progenitor galaxies along with the mass of gas that will turn into stars in each progenitor galaxy are used to calculate the internal energy of each progenitor using the virial relation ($E_{\mathrm{internal}} \propto GM^2/R$).

5. The radiated energy term is calculated using the impulses ($f_{k,i}$), gas fractions ($f_{g,i}$), and initial kinetic energies (K_i) after C08 ($E_{\mathrm{rad}} = -C_{\mathrm{rad}}\Sigma_{i=1}^{2} K_i f_{g,i} f_{k,i}(1 + f_{k,i})$). For our fiducial feedback model $C_{\mathrm{rad}} = 1.0$.

Impulse

$$\Delta E_i = \frac{A\,G^2 M_{tot,1}^2 M_{tot,1}}{V_{peri}^2 (R_{peri}^2 + B\,R_{tot,1} R_{peri} + C\,R_{tot,1}^2)}$$

$M_{tot,1}$, $M_{tot,2}$ $R_{tot,1}$, $R_{tot,2}$ V_{peri}, R_{peri} R_1, R_2 M_1, M_2

$K_{tot,1}$, $K_{tot,2}$

$$f_{i,k} = \frac{\Delta E_i}{K_{i,tot}}, i = 1,2$$

Radius

$$E_{internal,f} = E_{internal,i} + E_{radiated} + E_{orbital}$$

$f_{g,1}$, $f_{g,2}$

Mass of New Stars

$$M_{new,1} = C_{new} M_{tot,1} f_{g,1} f_{k,1}$$

$$M_{new,2} = C_{new} M_{tot,2} f_{g,2} f_{k,2}$$

Velocity Dispersion

$$\sigma_f^2 = C_{vir} \frac{G(M_1 + M_2 + M_{new,1} + M_{new,2})}{R_f (1 - f_{dm,f})}$$

$M_{dm,1}$, M_1, $M_{dm,2}$, M_2

Final Dark Matter Fraction

$$f_{dm,f} = \frac{M_{dm,1} + M_{dm,2}}{M_{dm,1} + M_{dm,2} + c_{stars}(M_1 + M_2 + M_{new,1} + M_{new,2})}$$

Properties Predicted from Initial Conditions

$$M_f, R_f, f_{dm,f}, \sigma_f^2$$

Figure 3.1: Summary of the inputs (ovals), outputs (white rectangle), and equations (shaded rectangles) needed to implement the merger model. The these formulas the coefficients C, of order unity, are determined using our suite of hydrodynamic galaxy merger simulations.

6. Initial internal energies, radiated energy, and orbital energy are combined to calculate final internal energy. Final energy is then used along with final mass to calculate the final half-mass radius.

7. The size of the final dark matter halo is calculated assuming dissipationless merging of the dark matter halos. An NFW profile is fit to the final halo and then a dark matter mass inside the stellar half-mass radius is determined. This value is used to calculate the central dark matter fraction. This is a different model than used in C08. See Appendix 3.7 for details.

8. A modified virial relation that accounts for changes in central dynamical mass, using the final central dark matter fraction calculated above, is used to calculate the velocity dispersion of the remnant.

3.2.2 Implementation of Merger Model with SAMs

In order to make comparisons with observational data, and to explore the evolution of scaling relations over cosmological time scales, we apply the new merger model to progenitor properties from several SAMs. We implement the merger model externally rather than incorporating it within each of the SAMs. This provides an expedient means of exploring the properties of new elliptical galaxies arriving into the population via the merging of disk-dominated galaxies. We restrict our analysis to mergers of disk galaxies because the current generation of SAMs do not have a reliable method for calculating bulge sizes, and we need stellar radii in order to calculate initial

internal energies. Consequently, we only analyze mergers in each SAM where both progenitors have a stellar disk more massive than their bulge. Additionally, since we are comparing the remnants to observations of elliptical galaxy populations, we only include major mergers with a mass ratio of 1:3 or greater, as these are the mergers expected to create elliptical galaxies.

To make comparisons with observations of elliptical scaling relations we implement our merger model using two different SAMs: the Somerville et al. (2008) SAM (hereafter S08) and a SAM based on the Millennium Simulation (Croton et al., 2006). Each SAM directly provides the stellar mass, disk radius, and mass of cold gas for each progenitor. In addition, the model requires information about the dark matter halo of each progenitor. Specifically, we need to be able to calculate mass as a function of radius in order to calculate both the halo half-mass radius and the central dark matter mass. S08 and Millennium provide the masses of the dark matter halos, but specify the halo mass distributions using different quantities. S08 provides halo concentrations. The Millennium SAM provides $V_{\max}$ and V_{vir}, from which concentration can be calculated. For both cases the concentration, virial mass, and redshift are used to calculate the distribution of mass within the halo. For S08 the spherical top-hat collapse model is used to calculate the virial overdensity, using the approximation from Bryan & Norman (1998), whereas for Millennium the virial overdensity is assumed to be 200.

The merger model also requires the total initial internal kinetic energy of each progenitor. This quantity is approximated by $K_{\mathrm{tot}} \simeq 0.35 G M_{\mathrm{tot}}^2 / R_{\mathrm{tot}}$ as described in C08. The final piece of information needed as model input is the initial orbit of each

galaxy merger. This information is not available from any of the SAMs. Consequently, we use a statistical distribution of orbits as measured from cosmological simulations (Benson, 2005), including the observed evolution with redshift. Each merger orbit is drawn randomly from the observed distribution for the redshift at which the merger occurs.

3.3 Systematic Exploration of the Merger Model

In order to gain a better intuitive grasp of the behavior of the model, we begin with a systematic exploration of the effects of variations in the progenitor properties and model parameters. For this study we introduce a series of four idealized progenitor models. In order to isolate the effects of various progenitor properties we begin with a fiducial progenitor and scale the progenitor properties in such as way as to keep baryon fraction, average density, and halo concentration constant.

The fiducial galaxy with which we begin our series is the G3 galaxy from Cox et al. (2008a), whose properties are designed to fit the average properties of observed disks in the Sloan Digital Sky Survey. The G3 has a dark matter halo mass of $1.1 \times 10^{12}M_{\odot}$, a stellar mass of $5.0 \times 10^{10}M_{\odot}$, an initial half-mass radius of 3.8 kpc, and a halo concentration of 6.0. Each subsequent galaxy in the series is created by reducing the mass by 1/3 and keeping the average densities, concentration, and baryon fraction constant. For each of the experiments below, the galaxies in the series are merged together on 100 orbits drawn from the low redshift distribution of halo merger orbits

measured from cosmological dark matter simulations by Benson (2005). The remnant properties shown in the experiments below are averaged over these 100 orbits. The scatter due to orbit is roughly the size of the symbols plotted.

3.3.1   Gas Fraction

Previous work has shown that gas can have a significant effect on merger remnants (Robertson et al., 2006; Dekel & Cox, 2006). Dekel & Cox (2006) suggest that a systematic variation in gas fraction with mass could be responsible for the tilt in the fundamental plane of elliptical galaxies, and Hopkins et al. (2008) demonstrate observational evidence for this hypothesis. Thus, we examine the effect of progenitor gas fraction, defined here as the ratio of gas to stellar mass, on the properties of equal-mass merger remnants.

In our first experiment we set the gas mass of each progenitor such that gas fraction is constant as a function of mass. We run the model for several gas fractions, setting the ratio of gas mass to stellar mass to 0.0, 0.5, 1.0, 2.0, and 4.0. The size-stellar mass relation, stellar-mass Faber-Jackson relation (FJ), and virial projection of the fundamental plane (FP) of the merger remnants are shown in Figure 3.2.

Several things are worth noting about the size-mass relation plotted (Figure 3.2(a)). First, for all gas fractions the remnant relations (crosses) are just shifted horizontally and vertically from the progenitor relation (stars) without any significant rotation. That is, the vector between progenitor and remnant is constant for any given gas fraction. This means that $R_{\mathrm{f}}/R_{\mathrm{i}}$ and $M_{\mathrm{star,f}}/M_{\mathrm{star,f}}$ are also constant for any particular

(a)

(b)

(c)
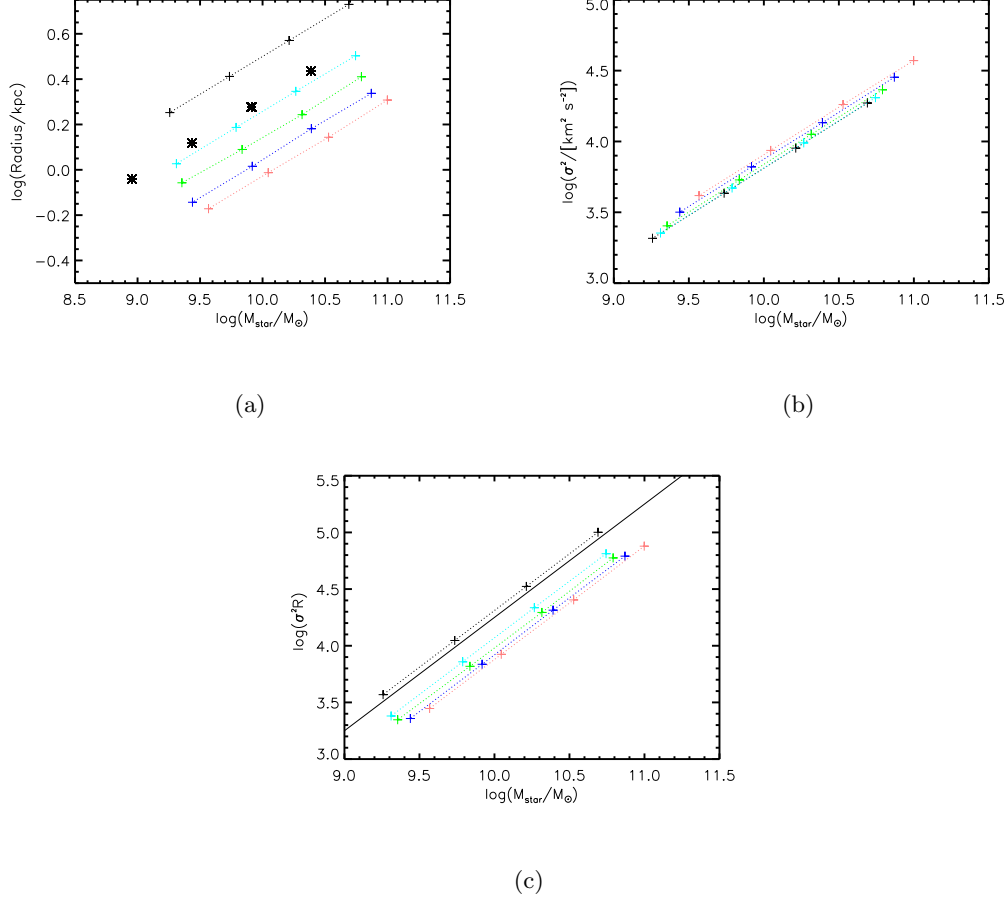
Figure 3.2: Scaling relations for merger remnants produced by the model from our series of idealized progenitors with a range of initial gas fractions held constant as a function of mass. (a) shows the size-stellar mass relation of the merger remnants (crosses) and progenitors (stars), while (b) and (c) show the stellar mass FJ relation and the fundamental plane for the merger remnants. The line plotted in (c) shows the slope for galaxies with a virial scaling. For remnants, colors depict ratio of gas mass to stellar mass in the progenitors that created that remnant where black=0.0, light blue=0.5, green=1.0, blue=2.0, and red=4.0. Dotted lines connect remnants with progenitors with the same gas fraction.

gas fraction. This is worth noting because the observed size-mass relations for disks and ellipticals are significantly rotated from one another with the relation for ellipticals being much steeper. A realistic mechanism for the production of ellipticals must account for this rotation.

One can also see from this figure that starting with zero and adding gas initially has a significant effect on the radius of the remnant, since the new stars form mainly near the center. As the ratio of gas to stars increases above about 1.0 the effect of additional gas on the merger remnant is less dramatic. This dwindling effect of gas results from the increasing dominance of new stars. As the mass of new stars overwhelms the old stars, one can no longer reduce the radius by forming more stars. In contrast to change in radius, the change in mass is approximately proportional to the gas mass added. Finally, remember that our progenitors are constructed so that they have a constant density inside their half-mass radius. Thus one can quickly see from the plot that 'dry' mergers, with no gas, will produce remnants with densities less than their progenitors and sizes larger than their progenitors, whereas gas-rich mergers will produce remnants with densities higher than their progenitors. The sizes of the remnants of gas-rich mergers can be similar to or even smaller than the sizes of their progenitors. For this value of model parameters constant density evolution occurs at roughly a gas to stellar mass ratio of 0.5 (light-blue crosses).

The stellar-mass FJ plot (Figure 3.2(b)) demonstrates a similar effect. Progenitors are not shown because they have no values for σ, however one can see that remnants of mergers with each gas fraction follow parallel lines. No rotation is intro-

duced between one gas fraction series and the next.

If elliptical galaxies followed an exact virial relation between stellar mass, velocity dispersion, and size then one would expect that $M_{\text{star}} \propto \sigma^2 R$. Thus plotting these quantities against each other gives us a 'virial' projection of the fundamental plane. Galaxies following the virial relation would fall on a line with a slope of one. Observed galaxies do not fall on the expected virial relation. This variance from virial scaling is the so-called tilt of the fundamental plane. In Figure 3.2(c) we plot M_{star} versus $\sigma^2 R$. The line plotted has a slope of one and therefore follows a virial scaling. The remnants from each gas fraction set fall on the same virial scaling. This demonstrates that our model produces no tilt in the fundamental plane for remnants when the progenitors' properties are scaled with the mass. However, while each gas fraction series follows the virial scaling, there is a shift between cases with different gas fractions such that larger gas fraction progenitors result in remnants with larger ratios of stellar mass to dynamical mass.

In the next experiment we let gas fraction vary as a function of mass. We fix the gas mass of the largest progenitor (G3) such that the ratio of gas mass to stellar mass is 0.25. Then we let the baryonic gas fraction vary as a power law with the baryonic mass, $M_{\text{gas}}/M_{\text{baryons}} \propto M_{\text{baryons}}^{-\gamma}$ (as suggested in Dekel & Cox (2006)). We use values of zero, one, and two for γ. In Figure 3.3 we show the scaling relations of the remnants produced by this series of progenitors. Each line of remnants is fixed to the largest mass remnant, but the slope of the size-mass and FJ relations clearly depends on the value chosen for γ. Non-zero values of γ allow for significant rotations in all of
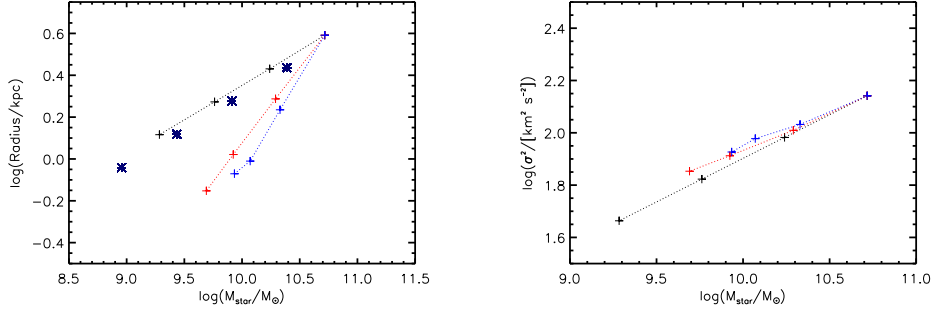
(a)   (b)
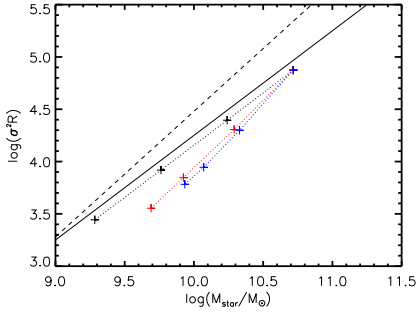
(c)

Figure 3.3: Scaling relations for merger remnants produced by the model from our series of idealized progenitors with a baryonic gas fraction that varies as a power law with baryonic mass ($M_{gas}/M_{baryons} \propto M_{baryons}^{-\gamma}$). (a) shows the size-stellar mass relation of the merger remnants (crosses) and progenitors (stars), while (b) and (c) show the stellar mass FJ relation and the fundamental plane for the merger remnants. The line plotted in (c) shows the slope for galaxies with a virial scaling. For remnants, colors depict the value of γ used to set the progenitor gas fractions black=0.0, red=1.0, and blue=2.0. Dotted lines connect remnants with progenitors from the same gas fraction power law.

the plotted projections of the FP. The rotation in the size-mass relation is the direction

of rotation required if one is to create ellipticals from mergers of disks that follow the

observed relations. The rotation in the FJ is the least pronounced of all of the relations.

Importantly, fundamental plane relation rotates away from the virial relation in the

same direction as the observed tilt. For reference, the slope of the observed tilt is shown

with a dashed line. The tilt required is slightly overshot by the $\gamma = 1$ case, suggesting

a slightly shallower power law slope would reproduce the observed tilt. This result is

compatible with the gas fraction power of 0.7 suggested by Dekel & Cox (2006). Thus

within our model a gas fraction gradient is capable of creating a tilt in the fundamental

plane. Our model relies on the virial relation to calculate sizes and velocity dispersion.

However, in our model the central dark matter fraction is calculated assuming that no

dissipation occurs within the dark matter halo, and this affects our calculation of σ.

The break from virial scaling results from this changing central dark matter fraction,

with more gas rich progenitors producing a larger difference between the dissipational

baryons and dissipationless dark matter resulting in a lower central dark matter fraction.

3.3.2   Model Parameters

The merger model contains several parameters with uncertain values because

of the uncertainty in the feedback prescription used by the merger simulations. The

most uncertain parameter is C_{new}, which determines the amount of stars that will form

in the merger via the equation $M_{\mathrm{new}} = C_{\mathrm{new}} M_{\mathrm{gas}} f_{\mathrm{k}}$. For our fiducial feedback model

C_{new} takes the value 0.3. However, the exploration of various feedback parameters in the

simulations suggests that a range of roughly 0.1 to 0.4 would be reasonable (Covington et al., 2008). Here we let C_{new} vary from 0.1 to 0.5 and examine the effect on the scaling relations.

First, we assume a constant gas to stellar mass ratio of 1 across the idealized galaxy series. Increasing C_{new} will increase the number of stars that form and, perhaps surprisingly, increase the remnant radius (Figure 3.4(a)). The first effect is obvious, however one might think that increasing the number of new stars would decrease the final radius. On the contrary, within the model, energy losses due to dissipation are not calculated directly from the mass of new stars formed but rather in a term that includes gas fraction, orbital impulse, and another parameter that fixes the relative importance of radiative loss. Thus, increasing C_{new} increases the size of all of the internal energy terms in the equation without increasing the radiative losses. This results in a reduction in the importance of dissipative losses and thus a slight increase in the final size. In the FJ relation, an increase in C_{new} results in increasing mass and slightly decreasing dispersion (Figure 3.4(b)). The dispersion decreases because of a combination of increasing size and decreasing central dark matter fraction. Adjusting C_{new} causes no rotation in any of the scaling relations. The normalization of the FP relation is very slightly affected, but no tilt is created by changing C_{new} (Figure 3.4(c)).

If we introduce a gas gradient with mass, then adjusting C_{new} can produce rotations of the scaling relations. To demonstrate this we create a series of mergers with gas fraction increasing as mass decreases. Specifically, to create each less massive progenitor in the series the gas mass is cut in half whereas all other masses are divided
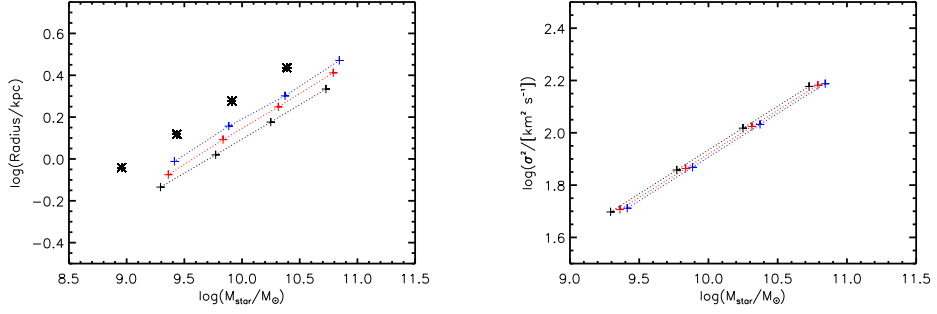
(a)

(b)
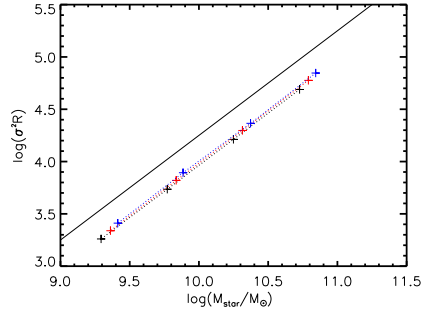
(c)

Figure 3.4: Scaling relations for merger remnants produced by the model from our series of idealized progenitors with a constant gas to stellar mass ratio of 1.0, and a varying star formation parameter C_{new}, which takes values of 0.1 (black), 0.3 (red), and 0.5 (blue). 0.3 is the fiducial value. (a) shows the size-stellar mass relation of the merger remnants (crosses) and progenitors (stars), while (b) and (c) show the stellar mass FJ relation and the fundamental plane for the merger remnants. The line plotted in (c) shows the slope for galaxies with a virial scaling. Dotted lines connect cases with the same value of Cnew.

by three. For this series changing C_{new} has a greater effect on the mergers with a larger gas fraction, resulting in rotations in the size-mass and FJ but no significant tilting in the FP (Figure 3.5).

Another parameter for which feedback could produce some uncertainty is C_{rad}, which sets the importance of the radiative energy term. In fact, because of the unphysical reduction of size with increasing C_{new} described above, one could argue that an adjustment of C_{new} should be accompanied by an adjustment of C_{rad}. Since the C_{rad} parameter is decoupled from the equation that determines the number of new stars, adjusting C_{rad} results in no difference in final mass. However, an increase of the parameter results in significant reduction of size and increase in velocity dispersion for the remnants. The same constant gas and gas gradient merger series are plotted in Figures 3.6 and 3.7 respectively with C_{rad} taking values of 0.5 (black), 1.0 (red) and 2.0 (blue). The value of C_{rad} determined by fitting to the merger simulations was 1.0. As with C_{new}, rotation in the scaling relations is only caused for the series with a gas gradient. For the gas gradient series a modest rotation is created in the size-mass and FJ relations, but adjusting C_{rad} never introduces a tilt in the FP. This is because the model is built on the assumption of the virial theorem, and the only portion of the model that violates this assumption is the formula for calculating the change in central dark matter fraction, which is then used to adjust the velocity dispersion. Changing C_{rad} does not affect this portion of the model.

(a)

(b)

(c)
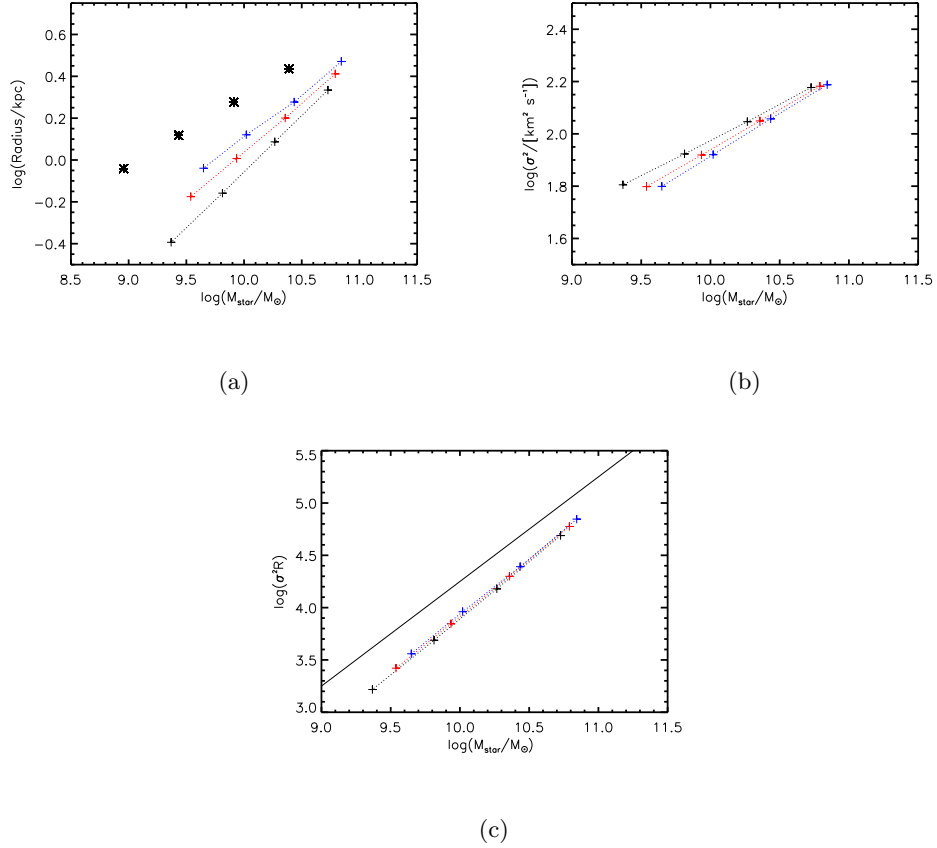
Figure 3.5: Scaling relations for merger remnants produced by the model from our series of idealized progenitors with a gas fraction gradient, and a varying star formation parameter C_{new}, which takes values of 0.1 (black), 0.3 (red), and 0.5 (blue). 0.3 is the fiducial value. (a) shows the size-stellar mass relation of the merger remnants (crosses) and progenitors (stars), while (b) and (c) show the stellar mass FJ relation and the fundamental plane for the merger remnants. The line plotted in (c) shows the slope for galaxies with a virial scaling. Dotted lines connect cases with the same value of Cnew.
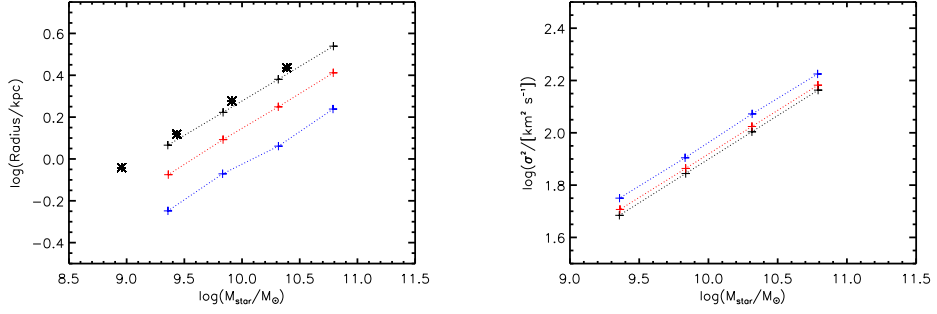
(a)

(b)
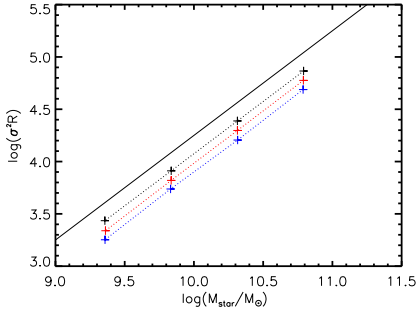
(c)

Figure 3.6: Scaling relations for merger remnants produced by the model from our series of idealized progenitors with a constant gas to stellar mass ratio of 1.0, and a varying radiative energy loss parameter $C_{\rm rad}$, which takes values of 0.5 (black), 1.0 (red), and 2.0 (blue). 1.0 is the fiducial value. (a) shows the size-stellar mass relation of the merger remnants (crosses) and progenitors (stars), while (b) and (c) show the stellar mass FJ relation and the fundamental plane for the merger remnants. The line plotted in (c) shows the slope for galaxies with a virial scaling. Dotted lines connect cases with the same value of Crad.

(a)

(b)

(c)
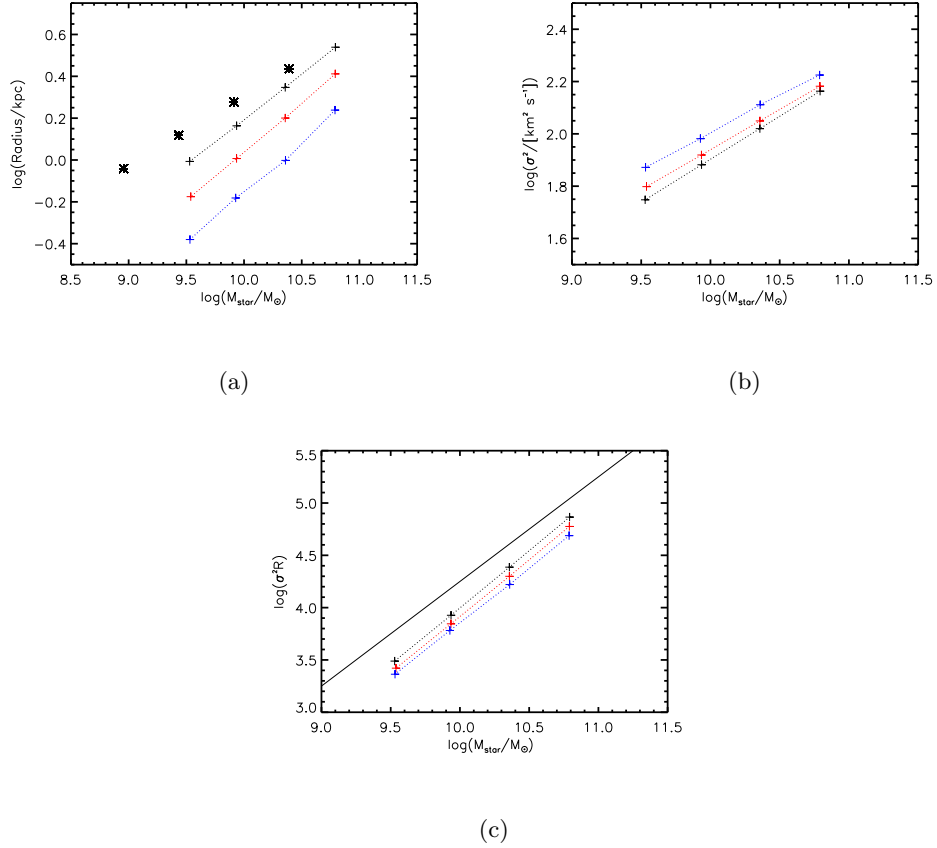
Figure 3.7: Scaling relations for merger remnants produced by the model from our series of idealized progenitors with a gas fraction gradient, and a varying radiative energy loss parameter C_{rad}, which takes values of 0.5 (black), 1.0 (red), and 2.0 (blue). 1.0 is the fiducial value. (a) shows the size-stellar mass relation of the merger remnants (crosses) and progenitors (stars), while (b) and (c) show the stellar mass FJ relation and the fundamental plane for the merger remnants. The line plotted in (c) shows the slope for galaxies with a virial scaling. Dotted lines connect cases with the same value of Crad.

71

3.4 Summary of Observational Results

The Sloan Digital Sky Survey (SDSS) (York et al., 2000) has provided exquisite statistics on galaxy scaling relations in the local universe. Shen et al. (2003) show that for local galaxies the size distribution for each type of galaxy at a given stellar mass is log-normal. They provide fitting functions for the medians of the distributions for both early- and late-type galaxies. For late-type galaxies the median ($\bar{R}$) is described by

$$\bar{R}(\text{kpc}) = \gamma \left(\frac{M}{\text{M}_\odot}\right)^\alpha \left(1 + \frac{M}{M_0}\right)^{\beta-\alpha}, \tag{3.1}$$

where $\gamma = 0.1$, $\alpha = 0.14$, $\beta = 0.39$, and $M_0 = 3.98 \times 10^{10}\text{M}_\odot$. A comparison of this distribution to that of Barden et al. (2005) demonstrates a discrepancy, despite the fact that the samples contain significant overlap. Specifically, a comparison of the stellar-mass size ridge line in Somerville et al. (2008) with the figure in Shen et al., correcting for the conversion between disk scale length and half light radius, shows that the Shen et al. distribution is a factor of ~ 1.5 smaller in radius for a given mass. In fact, the two distributions are off by a factor of 1.68 (Somerville, personal comm), suggesting an error in converting between scale radius and half-light radius. For the purpose of this paper we apply this correction factor to the distribution from Shen et al. (2003).

For early-type galaxies the median is described by

$$\bar{R}(\text{kpc}) = b \left(\frac{M}{\text{M}_\odot}\right)^a, \tag{3.2}$$

where $a = 0.56$ and $b = 3.47 \times 10^-5$. The scatter in the relation is similar for both late-

and early-types with the fit to late-type galaxies being

$$\sigma_{\ln R} = \sigma_2 + \frac{(\sigma_1 - \sigma_2)}{1 + (M/M_0)^2},$$ (3.3)

where $\sigma_1 = 0.47$ and $\sigma_2 = 0.34$.

The fit for the stellar mass Faber-Jackson relation in SDSS can be found in Gallazzi et al. (2006), and is given by

$$\log(\sigma_v(\text{km s}^{-1})) = 0.286 \log(M_*/\text{M}_\odot) - 0.895,$$ (3.4)

where σ_v is velocity dispersion and M_* is the stellar mass. The scatter in the relation is 0.071 dex.

The fundamental plane relation can be represented in a number of projections. However, recent work suggests that the tilt of the plane results from a systematic change in the central dark matter fraction (Zaritsky et al., 2007; Hopkins et al., 2008) as the result of a varying effect of dissipation with mass. A number of observational studies have examined the relationship between central dynamical and stellar mass,

$$M_{\text{dyn}} \propto M_{\text{star}}^{1+\alpha},$$ (3.5)

and have determined values of $\alpha \approx 0.2$ (Pahre et al., 1998; Gerhard et al., 2001; Padman-abhan et al., 2004; Gallazzi et al., 2006). Dynamical mass is proportional to $\sigma^2 R$. Previously it was thought that a changing proportionality constant, called non-homology, could be responsible for the relation between dynamical and stellar mass. However, mass modeling from two-dimensional kinematics (Cappellari et al., 2006) and gravitational lensing results (Bolton et al., 2007, 2008; Nipoti et al., 2008) suggest that central dynamical mass and true mass are approximately proportional for all stellar masses.

73

There is little published data on the evolution of the FJ and FP to high redshift. However, a number of studies have examined the evolution of the size-mass relations between $z \sim 0$ and up to $z \sim 3$ (Barden et al., 2005; McIntosh et al., 2005; Trujillo et al., 2006). The most comprehensive of these studies, Trujillo et al. (2006), combines data from SDSS, GEMS (Galaxy Evolution from Morphology and SEDs) and FIRES (Faint Infrared Extragalactic Survey) in order to quantify evolution between $z = 0$ and $z = 3$ for both early- and late-type galaxies. They differentiate galaxies by light concentration according to Sérsic index n and find that for both low-n (late-type) and high-n (early-type) galaxies the mean size at given mass at $z \sim 2.5$ is ~ 2 times smaller than today. Specifically they find that at given stellar mass the sizes of late-type galaxies evolve proportional to $(1 + z)^{-0.40 \pm 0.06}$, whereas the sizes of early types evolve proportional to $(1 + z)^{-0.45 \pm 0.10}$.

3.5 Comparison of Semi-Analytic Models with Observations

Now we apply our merger model within the S08 and Millennium SAMs. These SAMs produce statistical samples of galaxies with properties that are closely matched to those observed in the universe. Thus they provide an effective means for testing the merger model in a cosmological framework. Since the modeled merger remnants are a function of the progenitor properties, we begin by examining the distributions of galaxy properties in the SAMs and making comparisons to the observed distributions.

3.5.1 Properties of the Progenitors

In the model, the most important properties of the progenitors are initial size, mass, and gas fraction. Thus we begin by looking at the size-mass distributions of progenitors in each SAM. The relations are plotted for S08 in Figure 3.8 and for Millennium in Figure 3.9. For each figure the progenitors are separated into six redshift bins. Within each bin, the progenitors are divided into mass bins with a width of 0.5 in $\log(M_\odot)$. The local relations for low-n (solid blue) and high-n (dotted red) galaxies are shown for comparison. Additionally, the observed redshift evolution of the size of the low-n galaxies (Trujillo et al., 2006) is depicted with the blue-dashed line. This is calculated using the median progenitor redshift in each redshift bin.

The size-mass relation produced by the progenitors in S08 reproduces the observed relation quite nicely, including evolution with redshift. The Millennium progenitors are also fairly close to the observed relation, but in the lowest redshift bin they are $\sim 50\%$ too large on average. This gap lessens with increasing redshift. Also of note is that the highest mass bin is typically systematically high. This appears to be the result of increasing positive curvature at high masses. It is also interesting to compare the high-n relations (red curves). As noted before, if a merger explanation of the elliptical size-mass relation is to be successful, it must explain the rotation between the two observed relations.

Observing cold gas within galaxies is extremely challenging, however a study by Kannappan (2004) used a photometric estimation of gas fraction in order to calculate
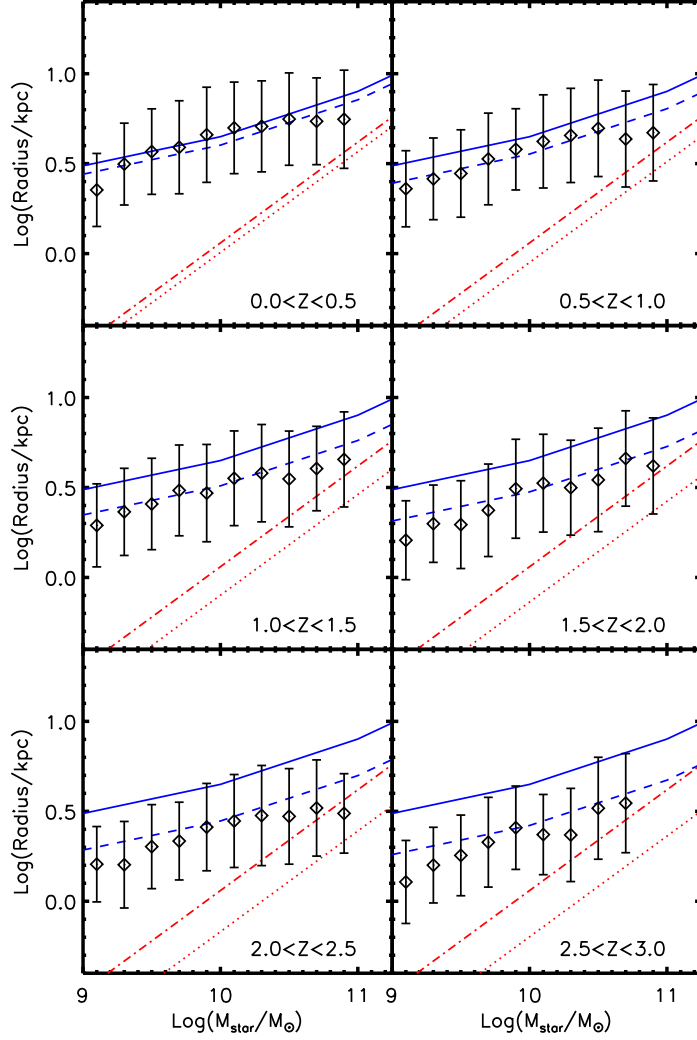
Figure 3.8: Size Mass relations for the progenitors in the S08 SAM, binned by redshift. Symbols denote the median of the progenitor distribution in the SAM, and error bars depict the 1σ spread in the distribution. The solid (blue) line and the dashed (red) line depict the redshift zero relations from Shen et al. (2003) of the low-n and high-n populations respectively. The blue-dashed and red-dotted lines depict the evolution of the low-n and high-n relations respectively with redshift as given by Trujillo et al. (2006). This is calculated using the median redshift for the progenitors in each bin. For this and subsequent scaling relations figures, blue and red lines denote observed scaling relations of disk and elliptical galaxies respectively.

76
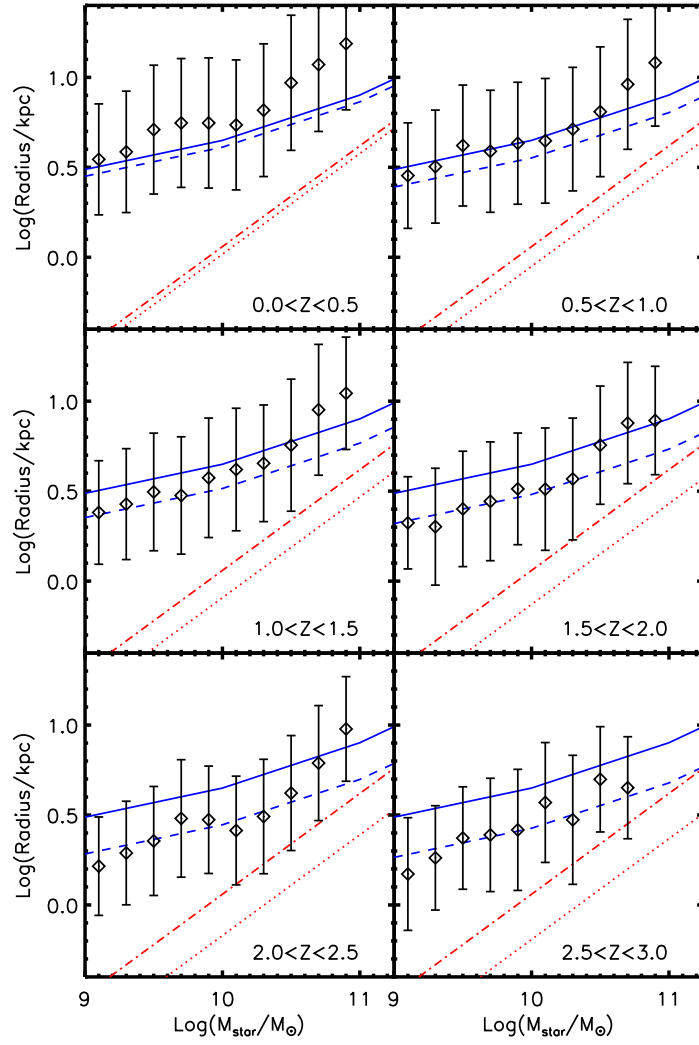
Figure 3.9: Size-Mass relations for the progenitors in the Millennium SAM. Symbols denote the median of the progenitor distribution in the SAM, and error bars depict the 1σ spread in the distribution. The solid (blue) line and the dotted (red) line depict the redshift zero relations from Shen et al. (2003) of the low-n and high-n populations respectively. The blue-dashed and red-dotted lines depict the evolution of the low-n and high-n relations respectively with redshift as given by Trujillo et al. (2006). This is calculated using the median redshift for the progenitors in each bin.

77

the changing ratio of gas to stellar mass (G/S) with galaxies from SDSS. Calura et al. (2007) use star formation rates from a large SDSS sample combined with theoretical modeling to estimate (G/S) as a function of both stellar mass and redshift. Neither study provides fits to the observed relation, but it can be seen from Figure 5 of Calura et al. (2007) that

$$\log(G/S) \sim -1.0 \log(M/M_\odot) + C, \tag{3.6}$$

where for blue galaxies $C \sim 10.85$ and for red galaxies $C \sim 10.35$. At the present time $\log(G/S)$ falls approximately in a range between -4 and 1.5.

The relation between G/S and stellar mass in the SAMs is shown in Figures 3.10 and 3.11. It can clearly be seen that the distributions of G/S in both SAMs are bimodal with a gas-rich (blue) and gas-poor (red) sequence. The lines plotted represent the approximate fits stated above for both red and blue galaxies. The total scatter around the observed relation is ~ 1 dex. Both SAMs capture the slope of the observed relation, however both SAMs produce more spread between the red and blue sequences than the observed relations. Also S08 has G/S that is systematically larger than the observed relations by ~ 0.3 dex. However, we also note that the progenitor gas fractions from S08 match well to the observed distribution from unpublished data on gas masses from Bell et al. (Somerville, personal comm). The relation from the SAMs only evolves very modestly over time, but for both SAMs the fraction of mergers that are coming from high gas fraction progenitors significantly increases with increasing redshift. This is seen both as a disappearance of the red sequence (in S08) and a decrease in the typical mass of progenitors as redshift increases (both SAMs).

78
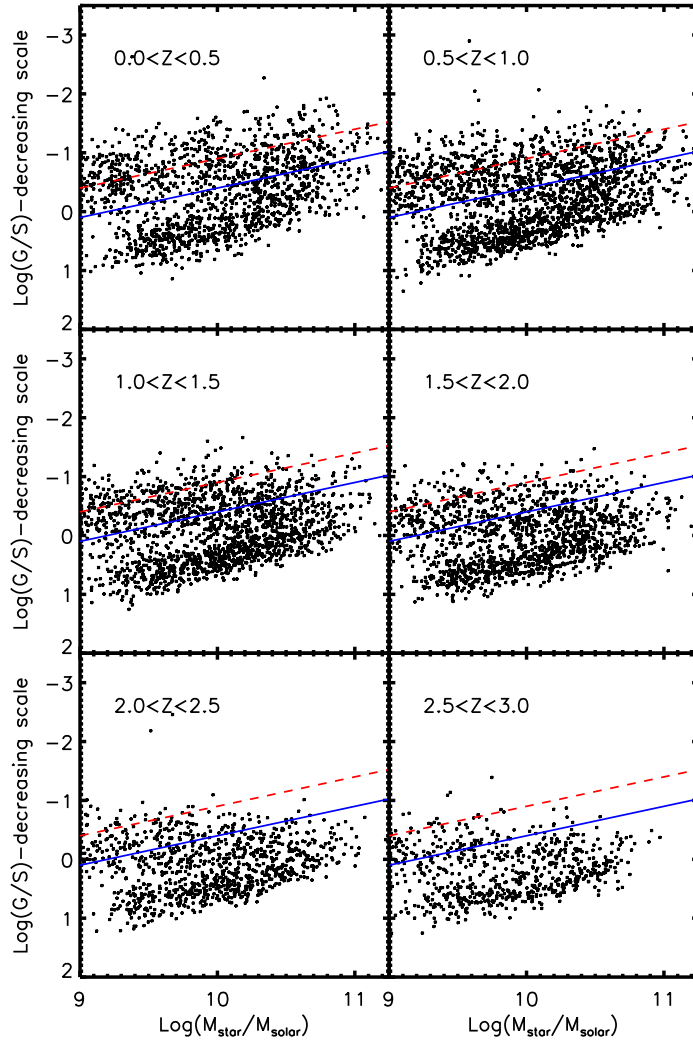
Figure 3.10: The relation between G/S and stellar mass for the progenitors in the S08 SAM. Points are galaxies from the SAM. The blue (solid) and red (dashed) lines are approximate fits to observations of nearby galaxies in the SDSS (Kannappan, 2004; Calura et al., 2007). $\log(G/S)$ is plotted using a decreasing scale as in the observational studies.
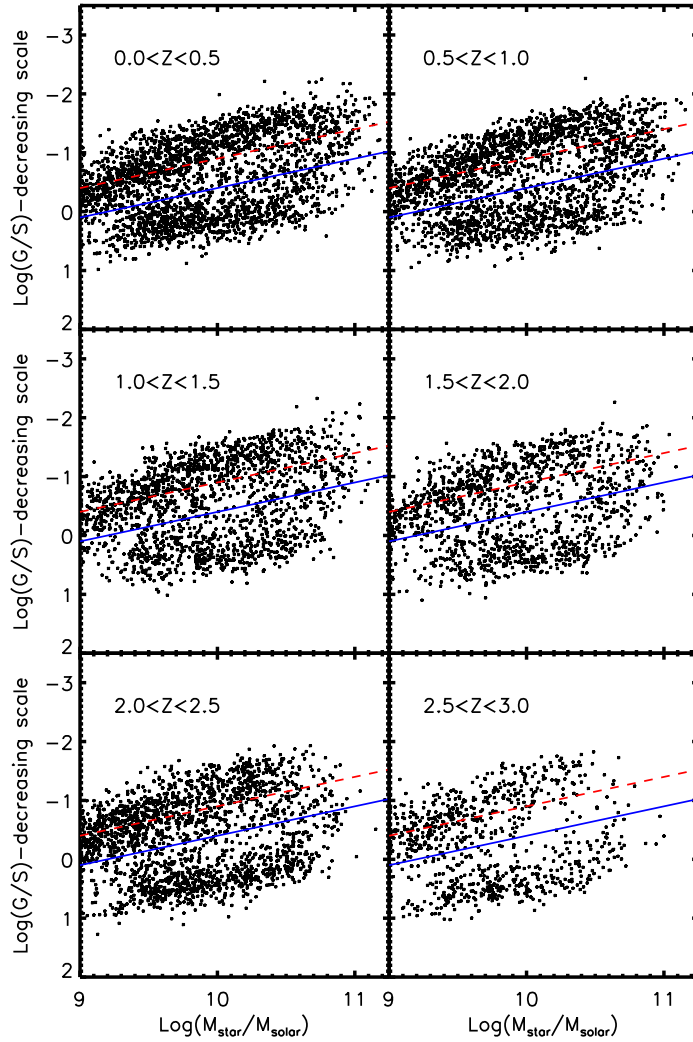
Figure 3.11: The relation between G/S and stellar mass for the progenitors in the Millennium SAM. Points are galaxies from the SAM. The blue (solid) and red (dashed) lines are approximate fits to observations of nearby galaxies in the SDSS (Kannappan, 2004; Calura et al., 2007). $\log(G/S)$ is plotted using a decreasing scale as in the observational studies.

There are also interesting correlations between gas fraction and size. To demonstrate this, we replot the size-mass relation with points drawn for progenitors colored by G/S (see Figures 3.12 and 3.13). Red points are gas-poor with $-2.0 < \log(G/S) < -1.0$. Green points have intermediate gas fractions with $-1.0 < \log(G/S) < 0.0$. Blue points are gas rich with $0.0 < \log(G/S) < 1.0$. For both SAMs, at given mass there is a significant trend of gas fraction with size. The larger radius progenitors have higher gas fractions. This is because these galaxies have lower densities and therefore have lower star formation rates and have consumed less of their gas. This has important implications for evolution of scaling relations with merging. Remember that dry merging moves galaxies up and to the right on the plot, that is, it increases both mass and size (Figure 3.2(a)). Because of their location far above the late-type scaling relation, dry merging would not take these progenitors on to the desired relation for remnants. However, since these galaxies are gas-rich they can travel with a horizontal or even somewhat downward vector when they merge. Additionally, this convergence of merging vectors within a single mass bin, such that the gas-poor compact galaxies move to larger radii while the gas-rich low density galaxies move to smaller radii, means that one could expect the scatter in sizes for a given mass bin to reduce somewhat after merging.

3.5.2 Properties of the Merger Remnants

Given progenitor properties, and statistically drawn orbits, the merger model allows us to predict the sizes, stellar masses, and velocity dispersions of the merger
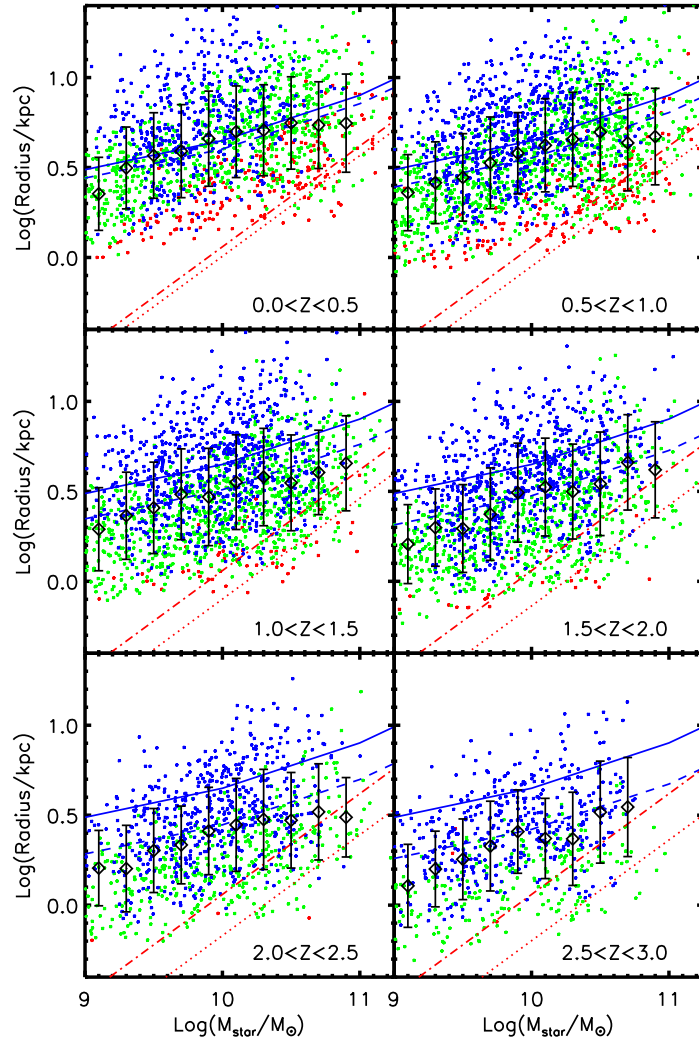
Figure 3.12: Size-Mass relations for the progenitors in the S08 SAM, binned by redshift and including points for progenitors colored by gas fraction. Red denotes $-2.0 < \log(G/S) < -1.0$. Green denotes $-1.0 < \log(G/S) < 0.0$. Blue denotes $0.0 < \log(G/S) < 1.0$. Other symbols and lines are as in Figure 3.8.
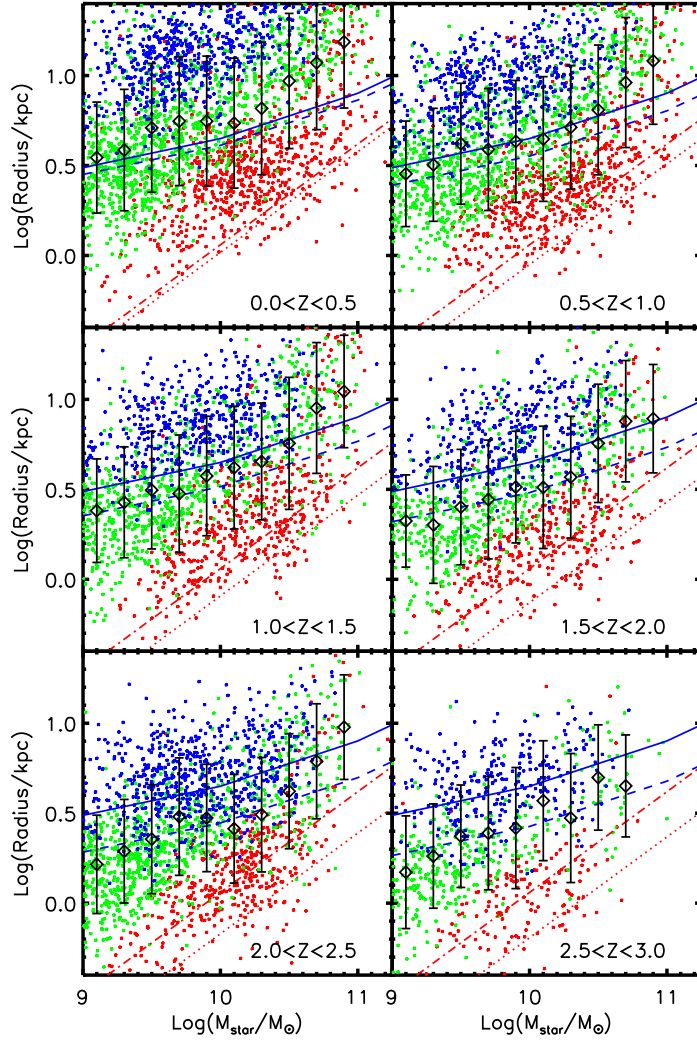
Figure 3.13: Size-Mass relations for the progenitors in the Millennium SAM, binned by redshift and including points for progenitors colored by gas fraction. Red denotes $-2.0 < \log(G/S) < -1.0$. Green denotes $-1.0 < \log(G/S) < 0.0$. Blue denotes $0.0 < \log(G/S) < 1.0$. Other symbols and lines are as in Figure 3.9.

remnants. We now exploit this ability to explore the buildup and evolution of the remnant scaling relations as predicted by the models. We begin with the size-mass relation, as it is best-constrained from both observations and the model.

The remnant size-mass relation for the SAMs is shown in Figures 3.14 and 3.15. Remember that S08 properly captured the normalization for the size-mass relation of the progenitors, including evolution with redshift. Again, S08 does well with the overall normalization of the remnant relation. However, it does best at low redshift and begins to underpredict sizes somewhat as redshift increases. By the highest redshift bin $(2.5 < z < 3.0)$ it underpredicts sizes by about 0.2 dex. However, this discrepancy is well within the errors on the observational sizes at that redshift.

For low redshift, the normalization of the size-mass relation from S08 is correct but the slope is slightly steeper than observed. The gas fraction gradient in the progenitors has produced rotation in the correct direction, but the relation has rotated somewhat too far. This improves with redshift and for high z the slope is very close to that observed. Comparing the S08 progenitor and remnant relations shows that the remnant relation is straighter, almost completely removing the decreasing slope at the high mass end of the progenitor relation. This can be explained if one also compares the progenitor gas fraction plot. At the high mass end the gas-rich blue sequence ends, whereas the red sequence continues, resulting in a more rapid decrease in gas fraction with increasing mass. This decrease in gas fraction causes the average high-mass remnant to be a little bit larger, canceling the effect from the progenitor size-mass relation.

As in the progenitor plots, the average size for galaxies in Millennium is too
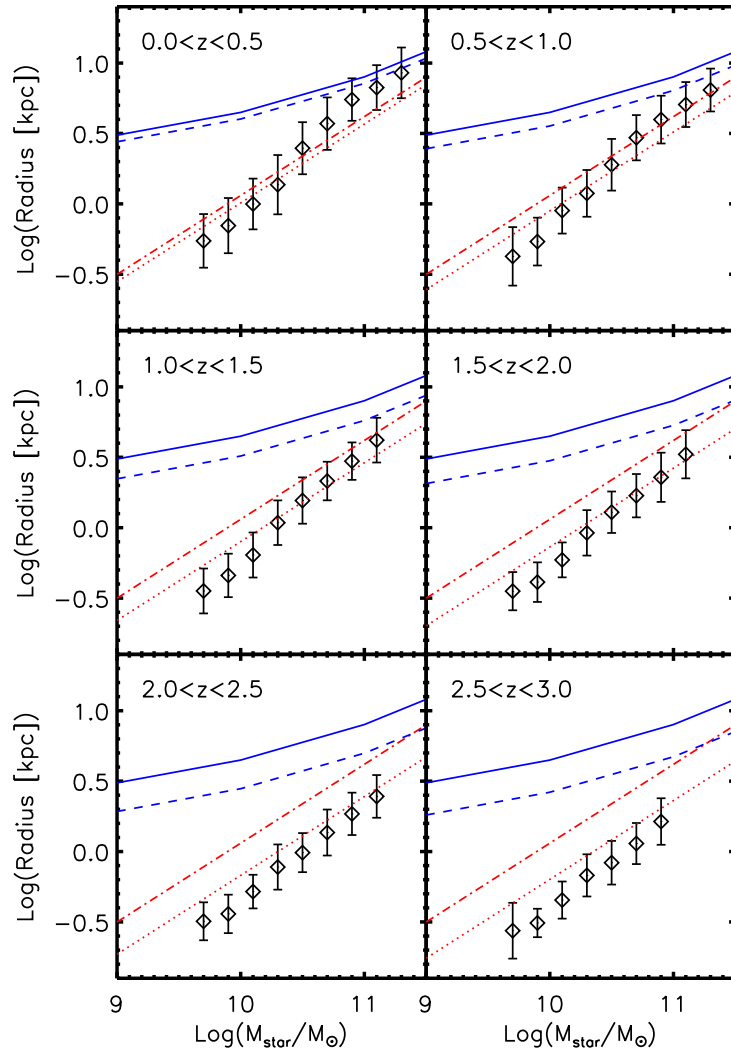
Figure 3.14: Size-Mass relations for the remnants in the S08 SAM, binned by redshift. Lines are observed relations as in Figure 3.8.
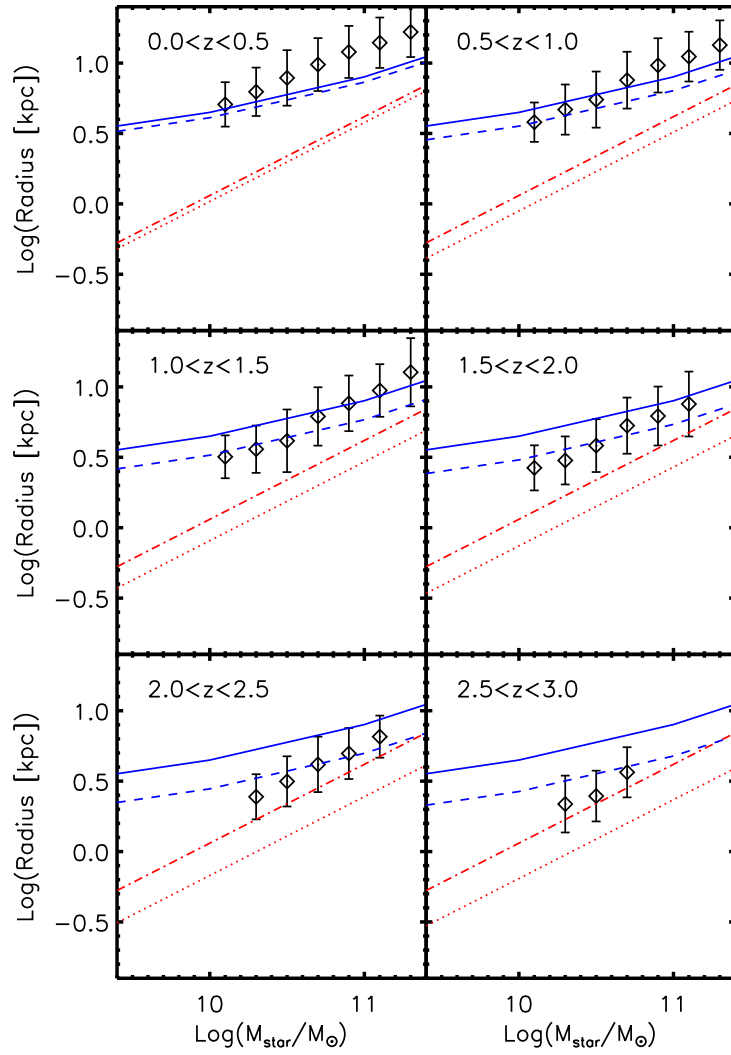
Figure 3.15: Size-Mass relations for the remnants in the Millennium SAM, binned by redshift. Lines are observed relations as in Figure 3.9.

large. The size of the discrepancy is smaller for progenitors than for remnants. Millennium produces a different normalization for the size-mass relation than S08 for two reasons: 1) the progenitors are larger, and 2) the progenitors have less gas. The slope of the relation is, however, quite close to the observed relation for all redshifts. The evolution in the size-mass relationship is such that in the highest redshift bin $(2.5 < z < 3.0)$ the average size at a given mass is ~ 3 times smaller than in the lowest redshift bin. Again this is slightly more evolution than observed, but is within the errors of the observed evolution. Unlike in S08, which evolves noticeably, the slope of the remnant size-mass relation from Millennium remains fairly constant with redshift.

In addition to sizes, the merger model predicts values for velocity dispersion (σ), so we also examine the stellar-mass Faber-Jackson relation (FJ) (see Figures 3.16 and 3.17). All models roughly produce the proper slope for the local FJ. Millennium does somewhat better with the slope, and S08 deviates to a flatter than observed slope at low mass. This is likely the result of the slight under-prediction of size at low mass. While S08 has the correct normalization at $z = 0$, Millennium produces a systematic offset. Since remnants from Millennium are systematically too large they also have systematically low velocity dispersions. Both SAMs show an evolution of FJ with redshift. Within the model there are two possible mechanisms for evolution in σ at a given mass: evolving size and evolving dark matter halo properties. For S08 σ at a given mass increases by roughly a factor of 1.5 between $z = 0$ and $z = 3$; for Millennium σ increases by a factor of 1.75. These values are commensurate with the factor of 2.5 and 3.15 decrease in size at a given mass for S08 and Millennium respectively, suggesting

87

that changing dark matter properties have little effect on the evolution. It is not known yet whether this evolution is consistent with the real universe, thus the result from the model is a theoretical prediction, which may be validated or contradicted by future observations.

Finally, we examine the fundamental plane relation (FP) as predicted by the merger model. The model uses the virial relation to predict values for σ, however the mass used in the model is a dynamical mass that includes a contribution from dark matter. Therefore, if a tilt is produced by the model in the virial projection of the FP, then it is purely a result of changing dark matter content in the galaxy centers. In Figures 3.18 and 3.19 we plot the relation between $\sigma^2 r$ and stellar mass. Indeed, the model produces a tilt from the expected virial relation (dotted red line), similar to the observed tilt (solid red line). The FP is tilted in the same sense as is suggested by observations, with dynamical mass increasing faster than stellar mass. This tilt results from the contrasting dissipational and dissipationless evolution of the baryonic and dark matter components convolved with the gas gradient in the progenitors. Lower mass progenitors have higher gas fractions and therefore produce more compact stellar remnants with smaller central dark matter fractions. Higher mass progenitors have smaller gas fractions and therefore end up with a sparser stellar center, resulting in larger central dark matter fractions.

While both SAMs produce a FP that is tilted by roughly the same amount as the observed FP, they produce different evolutions with redshift. The Millennium SAM produces so systematic evolution in tilt with redshift, whereas S08 produces a FP tilt
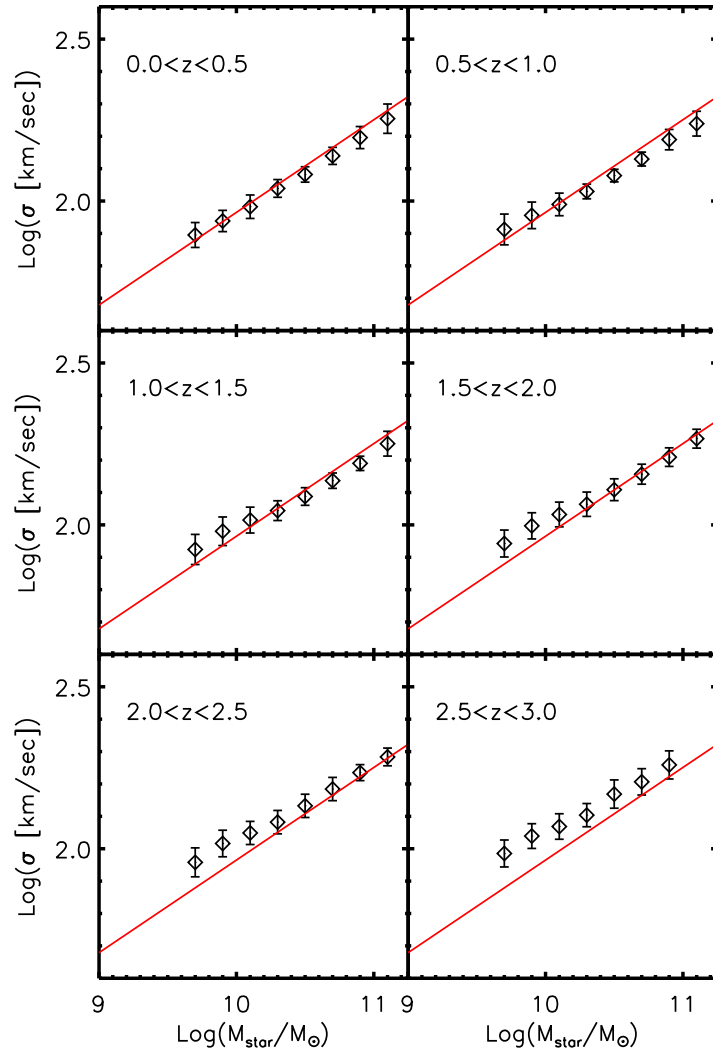
Figure 3.16: Faber-Jackson relations for the remnants in the S08 SAM, binned by redshift. Red line is the observed relation at low redshift (Gallazzi et al., 2006).
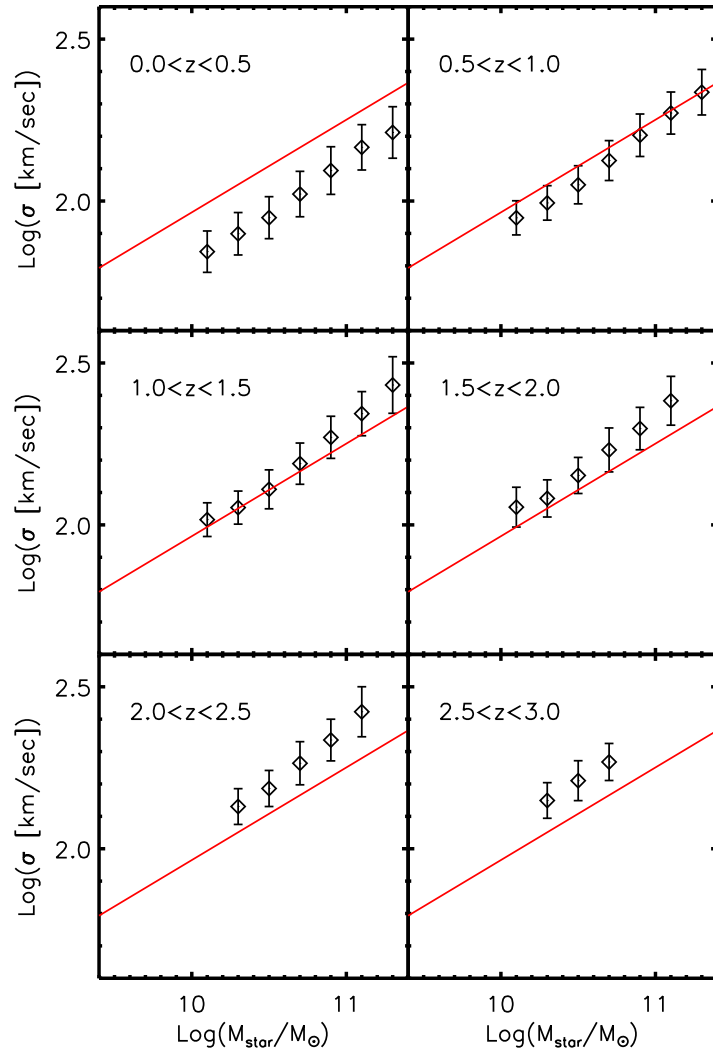
Figure 3.17: Faber-Jackson relations for the remnants in the Millennium SAM, binned by redshift. Red line is the observed relation at low redshift (Gallazzi et al., 2006).

90

that gradually decreases with redshift. This is related to the changing size-mass relation slope for S08 and is the result of a changing slope for the progenitor gas fractions.

Plotting σ versus r gives a nearly face-on view of the FP, and allows us to determine the portion of the FP being populated and a given redshifts by major mergers of disk galaxies. We show this relationship for both S08 (Figure 3.20) and Millennium (Figure 3.21). Both SAMs show a correlation between σ and r such that galaxies with larger sizes also tend to have larger velocity dispersions. Most interesting perhaps is the noticeable evolution with redshift across the face of the FP. At high redshift the mergers produce primarily high σ galaxies with relatively small sizes. As time progresses toward $z = 0$, the typical σ of a merger remnant decreases and the typical size increases, as the correlation between the size and velocity dispersion marches across the face of the plane.

3.5.3 Mergers of Progenitors that Follow the Observed Relations

It is encouraging that the SAMs produce reasonable scaling relations, particularly S08. However, in order to disentangle the success of the merger model from the success of the SAMs at predicting progenitor properties, we conduct a test case where only stellar masses and dark matter properties are taken from the SAM. For this case we use the S08 SAM and for each merger we draw the progenitor sizes and gas fractions from the observed relations. Sizes are drawn from the Shen et al. (2003) distribution and gas fractions are assumed to fall exactly on the relation derived from (Kannappan, 2004) for blue galaxies (equation 3.6). This allows us to check whether the model
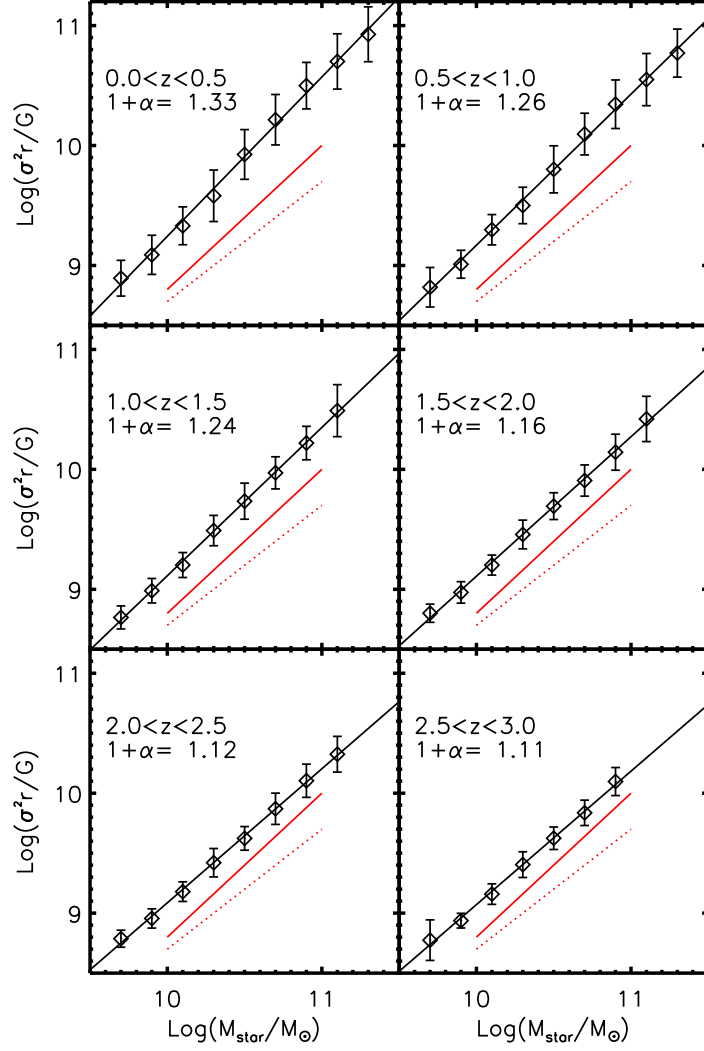
Figure 3.18: Fundamental plane plotted as M_{star} versus M_{dyn} for the remnants in the S08 SAM, binned by redshift. The solid red line shows the observed scaling of $M_{dyn} \propto M_{star}^{1.2}$, and the dotted red line shows the virial scaling. The black line is fit to the SAM remnants with $M_{dyn} \propto M_{star}^{1+\alpha}$ and $1 + \alpha$ is shown on the figure.
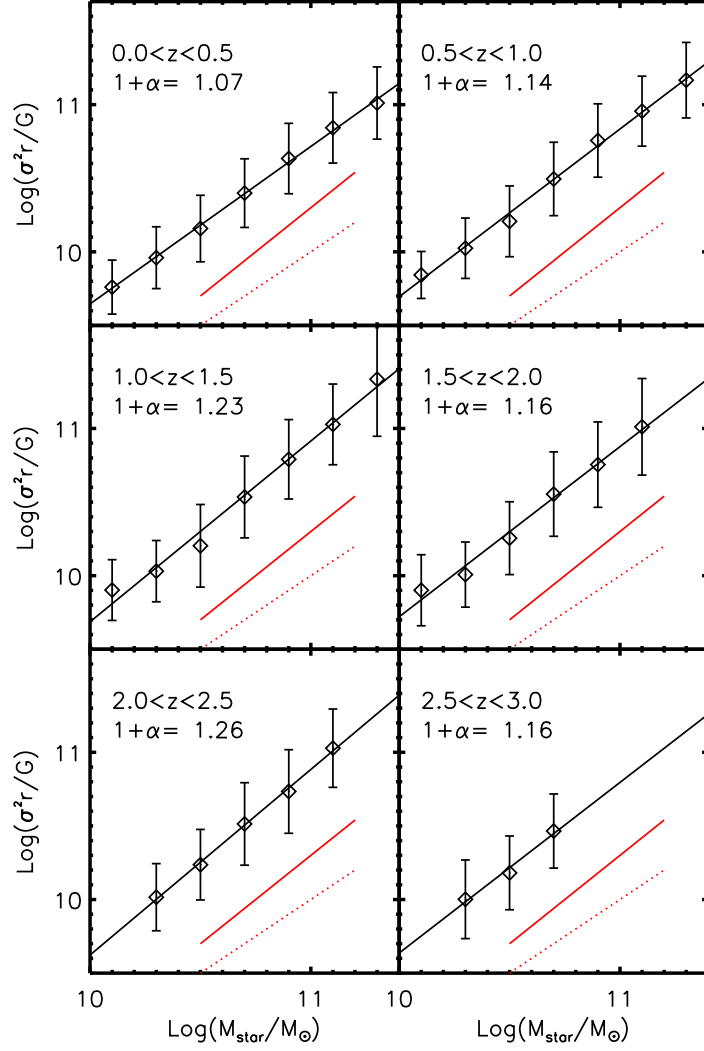
Figure 3.19: Fundamental plane plotted as M_{star} versus M_{dyn} for the remnants in the Millennium SAM, binned by redshift. The solid red line shows the observed scaling of $M_{\text{dyn}} \propto M_{\text{star}}^{1.2}$, and the dotted red line shows the virial scaling. The black line is fit to the SAM remnants with $M_{\text{dyn}} \propto M_{\text{star}}^{1+\alpha}$ and $1 + \alpha$ is shown on the figure.
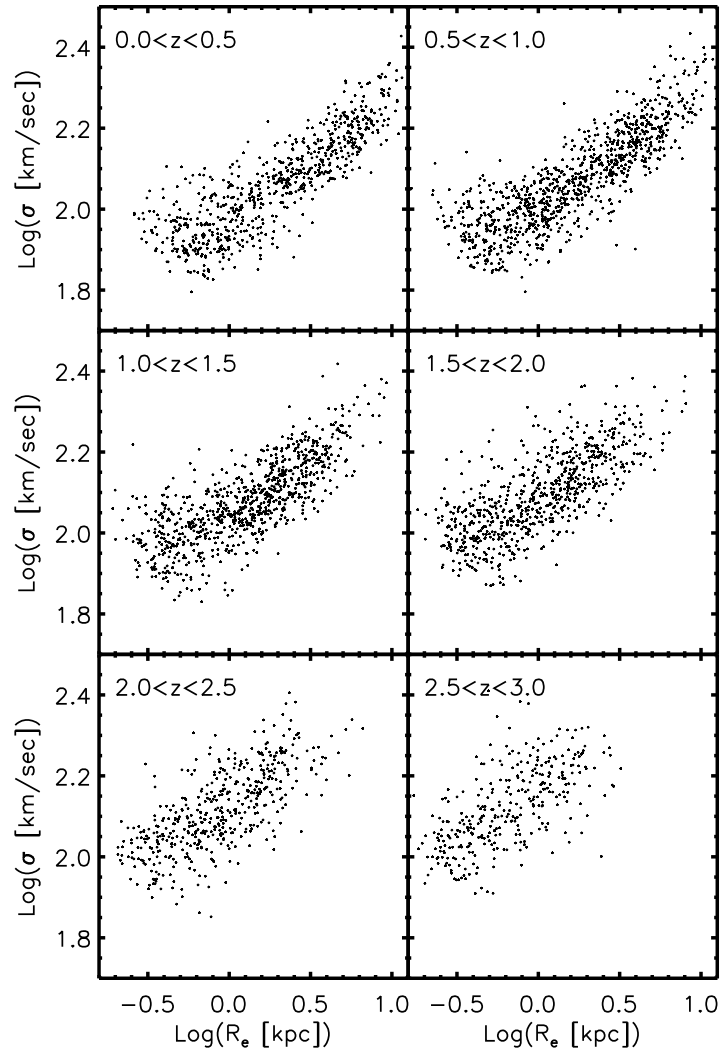
Figure 3.20: Nearly face-on view of the fundamental plane plotted as r versus σ for the remnants in the S08 SAM, binned by redshift.
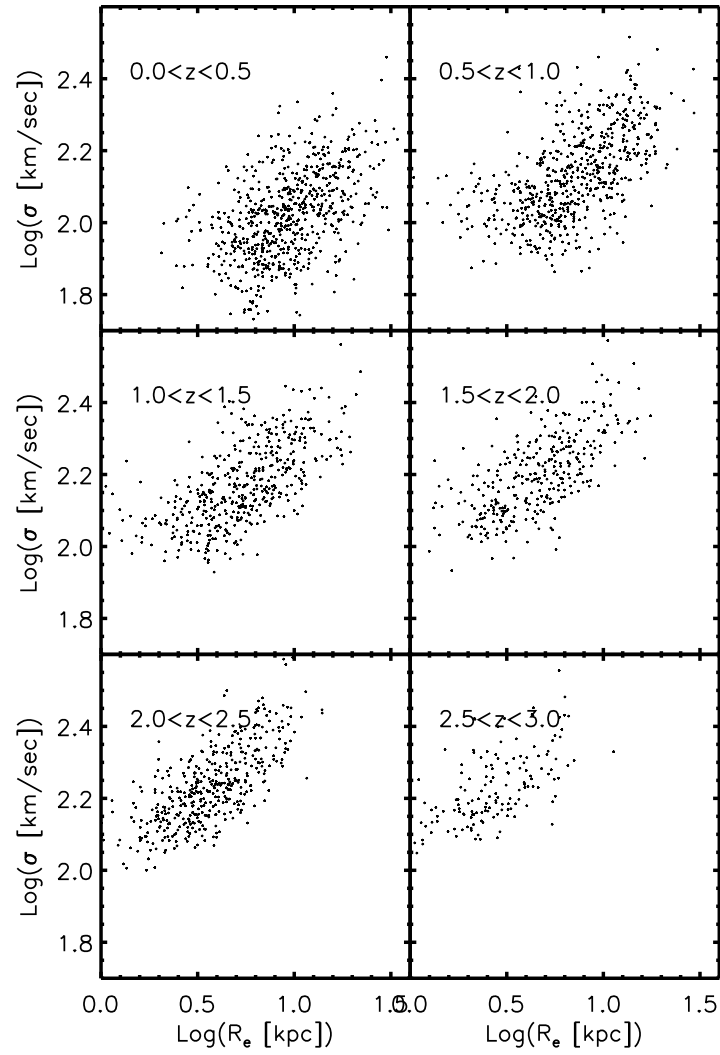
Figure 3.21: Nearly face-on view of the fundamental plane plotted as r versus σ for the remnants in the Millennium SAM, binned by redshift.

produces the correct results when the progenitor properties are correct.

The results of this test are shown in Figures 3.22, 3.23, and 3.24. In general, since the S08 progenitors are relatively close to the observed relations, the results are quite similar to using the full S08 SAM. Since the gas fractions used in this test are for low redshift galaxies, one would not necessarily expect agreement with the observed size-mass relations at higher redshift. In fact, the test size-mass relation shows less evolution than the observed evolution from Trujillo et al. (2006). Because the test progenitor gas fractions are not evolving this is not a problem with the model, but it does provide additional information about what is causing the evolution of remnant size in the model. Because we see some evolution we know that evolution in progenitor size will cause evolution in remnant size. But this alone is not enough to reproduce the observed evolution for early-type galaxies. The additional evolution that is being captured so well by the model in Figure 3.8 is being produced by an evolution toward higher gas fractions in the progenitors from the SAMs.

The agreement with the Faber-Jackson relation is striking. It shows no evolution with redshift, in contrast to the results from the SAMs. This results from the lack of evolution in gas fractions in our test. The FP retains roughly the observed tilt, and does not evolve appreciably with redshift. Again, this is likely the result of the constant relation applied between gas mass and stellar mass. The test confirms that if we use progenitor properties from observed distributions the model gives us the correct results. This suggests that little, if any, tuning is needed of model parameters.
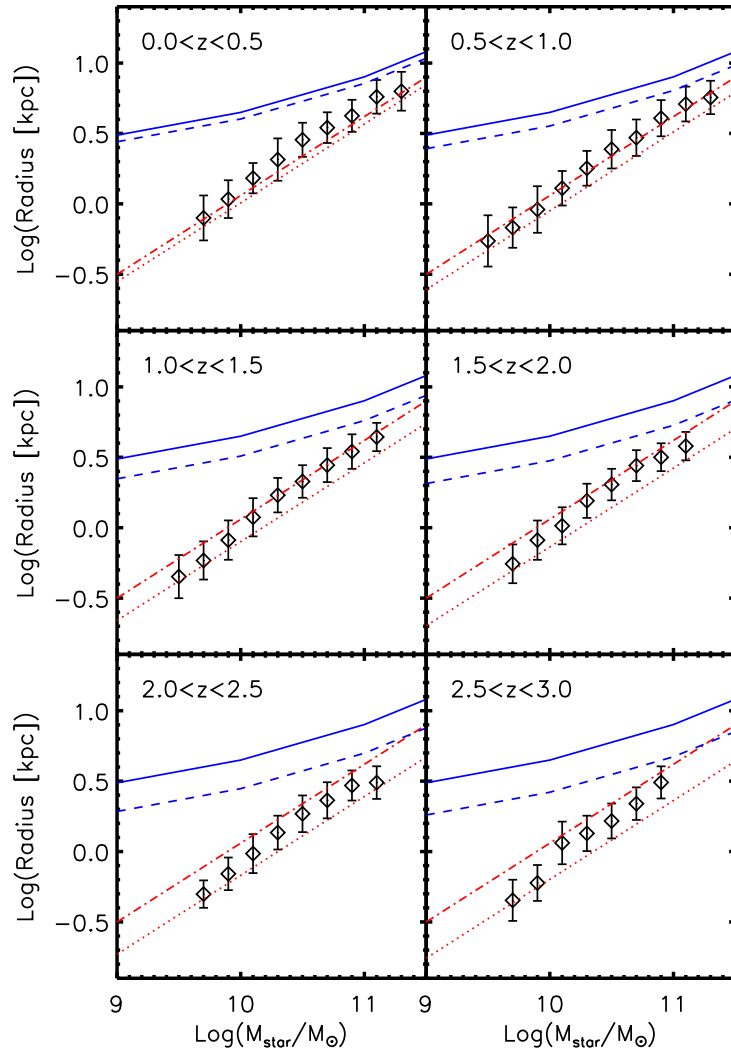
Figure 3.22: Size-Mass relations for the remnants using the observed distributions of progenitor properties, binned by redshift. Lines are observed relations as in Figure 3.8.
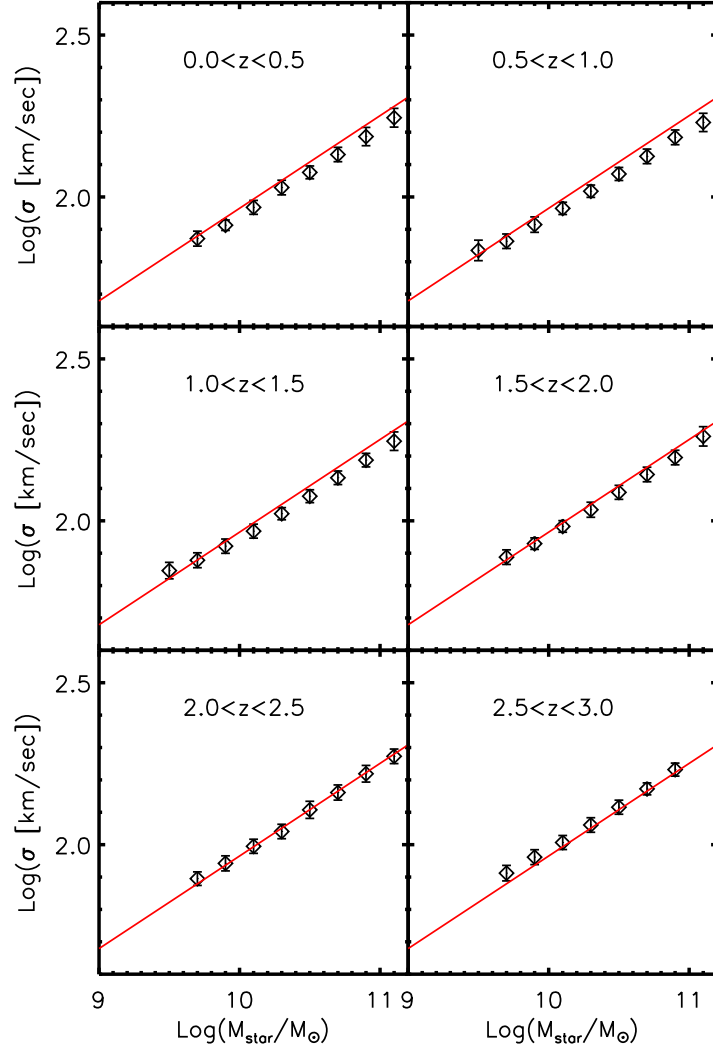
Figure 3.23: Faber-Jackson relations for the remnants using the observed distributions of progenitor properties, binned by redshift. Red line is the observed relation at low redshift (Gallazzi et al., 2006).
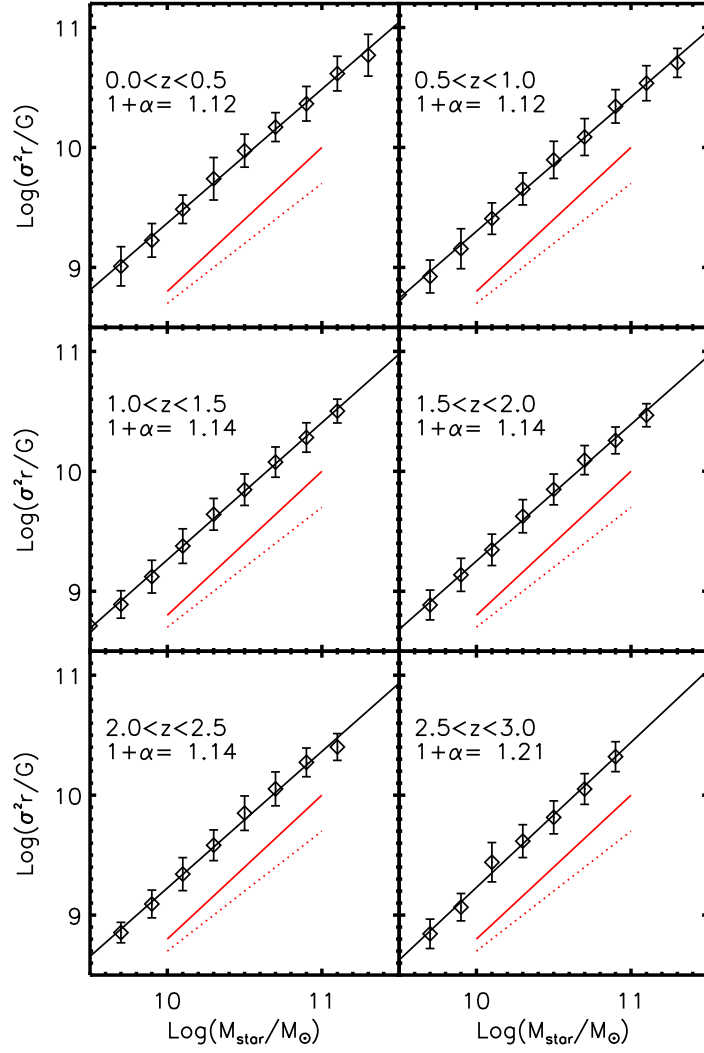
Figure 3.24: Fundamental plane plotted as M_{star} versus M_{dyn} for the remnants using the observed distributions of progenitor properties, binned by redshift. The solid red line shows the observed scaling of $M_{\mathrm{dyn}} \propto M_{\mathrm{star}}^{1.2}$, and the dotted red line shows the virial scaling. The black line is fit to the SAM remnants with $M_{\mathrm{dyn}} \propto M_{\mathrm{star}}^{1+\alpha}$ and $1 + \alpha$ is shown on the figure.

3.6 Discussion

A continuing question in the field of galaxy formation is the role that mergers play in constructing elliptical galaxies. Shen et al. (2003) have suggested that it is difficult to get the proper elliptical galaxy scaling relations from repeated major mergers of disk galaxies because of the rotation between the relations (Shen et al., 2003). However, Shen et al. did not take into account the effect of a gas gradient within the progenitors. Here we demonstrate that if the effect of gas is included, the remnants of major mergers of disk galaxies at each redshift fall near the observed size-mass relation at that redshift. A gradient in progenitor gas fraction with mass, such that higher mass galaxies have less gas, will create a steepening in the remnant size-mass relation.

Comparison of the progenitor and remnant properties suggests that the overall normalization of the early-type size-mass relation is determined by a combination of the size-mass relation of the progenitor disk galaxies and the normalization of the gas fraction relation. The slope in the relation between gas fraction and mass is responsible for rotating the size-mass relation from the shallower disk relation to the steeper elliptical relation during the merger process.

In order to capture the observed FJ relation, it is necessary to track the changing central dark matter fraction. The results from our model suggest that FJ may evolve modestly over time such that early-type galaxies at a given mass have larger velocity dispersions at larger redshift. This evolution is explained by the evolution in the size-mass relation. The observed tilt in the FP is also reproduced by our model and is

the result of a changing central dark matter fraction with mass. This changing dark matter fraction is caused by a gradient in gas fractions in the progenitors. Higher mass progenitors have less gas and therefore less dissipation during their mergers, resulting in remnants with less of a concentrated stellar center and a consequently higher dark matter fraction. In the face-on view of the FP the remnants evolve from higher σ and lower r at high redshift to lower σ and higher r at low redshift.

In future work, it will be useful to incorporate the model from C08 within SAMs. This will allow a more comprehensive exploration of the evolution of galaxy scaling relations via merging by allowing the inclusion of a wider variety of progenitor types, and enable the study of correlations with other quantities such as age and metallicity. An additional improvement would be to use the actual orbital parameters of each merger from the simulations instead of drawing orbits from the statistical distribution. This would allow exploration of potential environmental effects due to systematically different orbits. However, even the simple external processing of SAM progenitors using this merger model as carried out in this study suggests that mergers are a viable mechanism for the production of elliptical galaxies. Furthermore, the elliptical scaling relations are naturally explained given the combination of progenitor scaling relations and gas fractions.

3.7 Appendix A: New Model for Central Dark Matter Fraction

In C08 we presented a formula for calculating the dark matter fraction in the central part of the merger remnants. We define the dark matter fraction with a given radius as

$$f_{\mathrm{dm}} = \frac{M_{\mathrm{dm}}}{(M_{\mathrm{dm}} + M_{\mathrm{stars}})}, \tag{3.7}$$

where M_{dm} and M_{stars} are the dark matter and stellar masses inside that radius, respectively. For the merger simulations we found that the dark matter fraction inside half of the stellar half mass radius could be well-approximated by the following formula:

$$f_{\mathrm{dm,f}} = \frac{M_{\mathrm{dm,1}} + M_{\mathrm{dm,2}}}{M_{\mathrm{dm,1}} + M_{\mathrm{dm,2}} + C_{\mathrm{stars}}(M_1 + M_2 + M_{\mathrm{new}})}. \tag{3.8}$$

$M_{\mathrm{dm,1}}$ and $M_{\mathrm{dm,2}}$ are the dark matter masses inside half of the three-dimensional stellar half-mass radii of the progenitors. M_1 and M_2 are the stellar masses of the progenitors, and M_{new} is the total mass of stars formed during the merger. This expression simply assumes that the inner region of the remnant contains the same amount of dark matter as the sum of the inner regions of the progenitors, and that a fixed fraction, C_{stars}, of the final stellar mass is inside one-half of the three-dimensional stellar half-mass radius.

While this formula works well for the simulated remnants, it fails outside the regime where $R_{progenitor} \sim R_{remnant}$. One of the benefits of the formula is that since it puts all of the central dark matter from the progenitors into the central portion of the remnant it allows contraction of the halo as a result of the baryonic dissipation.

However, this contraction is precisely what causes the problem when the initial and final radii differ greatly. Specifically, for high gas fraction progenitors with large radii, the remnants can have much smaller radii and the previous formula predicts extreme contraction of the dark matter.

In order to increase the applicability of the merger model, we introduce a simpler, more physically intuitive model for predicting the central dark matter fraction that does not suffer from the deficiencies mentioned above. We begin with the dark matter halo masses and half-mass radii, and assume that the two halos merge dissipationlessly so that

$$\frac{(M_{1,\mathrm{dm}} + M_{2,\mathrm{dm}})}{R_{\mathrm{dm,f}}} = \frac{M_{1,\mathrm{dm}}}{R_{1,\mathrm{dm}}} + \frac{M_{2,\mathrm{dm}}}{R_{2,\mathrm{dm}}}. \tag{3.9}$$

This equation can be solved for the final halo half-mass radius $(R_{\mathrm{dm,f}})$. We use the final radius and mass to fit an NFW profile to the final halo. Then we calculate the mass expected inside the stellar half-mass radius and this value is used to calculate the final central dark matter fraction. For this paper we calculate the dark matter fraction inside the stellar half-mass radius and use this to compute the velocity dispersion of the merger remnant. In addition to extending the range of validity, this new method removes one of the least certain parameters from the merger model. A check against the merger simulations demonstrates that the new method produces a larger scatter between predicted and measured velocity dispersion, with the fractional rms scatter increasing from 0.24 to 0.35. However, most of the additional scatter results from variations in orbit, and in this work we find that the distribution of orbits found in N-body simulations is such that orbital variation plays a minor role.

Chapter 4

Stellar Mass Tully-Fisher Relation

Evolution in Galaxy Merger Simulations

4.1 Introduction

In today's Universe, galaxies follow two similar scaling laws that relate orbital speeds to stellar masses: the Tully-Fisher law (TF) (Tully & Fisher, 1977) for rotating disk galaxies, which relates stellar mass to rotation velocity (V_{rot}), and the Faber-Jackson law (FJ) (Faber & Jackson, 1976) for spheroidal (elliptical) galaxies, which relates stellar mass to velocity dispersion (σ). The standard paradigm for forming ellipticals is through mergers of disk galaxies (Barnes & Hernquist, 1992), in which case the FJ law descended from the TF law, as modified by mergers.

The TF and FJ laws relate the specific kinetic energy required to support a galaxy to the attractive potential well created by the mass of the galaxy. Kassin et al. (2007) observed the kinematics and masses of emission line galaxies in a redshift range from 0.1 to 1.2 from the All Wavelength Extended Groth Strip International Survey (AEGIS) and the Deep Extragalactic Evolutionary Probe 2 Survey (DEEP2), incorporating morphologically normal and disturbed galaxies. They find that while the normal galaxies generally lie on the standard TF law, the disturbed galaxies do not. Many of the disturbed galaxies have rotation velocities that are well below the normal values. This is not surprising, as one might expect kinematic relations to fail for cases where the systems are not in equilibrium. Non-equilibrium galaxies need not have a delicate balance between supporting velocities and attractive gravitational forces. Interestingly, when Weiner et al. (2006) and Kassin et al. (2007) incorporated the random internal motions of galaxies, as measured by velocity dispersion, along with rotational veloc-

ity into a new parameter, $S_{0.5} = \sqrt{0.5V_{rot}^2 + \sigma^2}$, then all galaxies regardless of type fell onto a single relation between $S_{0.5}$ and stellar mass. It is surprising that a set of non-homologous and even non-equilibrium systems fall on the same kinematic relation.

Given the complexity of effects at work, it is difficult to understand the reason for this tight kinematic relation. Perhaps the velocity dispersion is not measuring random motion, there are observational effects, such as blurring, that could be responsible for the transformation between rotation and dispersion. Or it could be that $S_{0.5}$ is measuring a total specific kinetic energy and that the virial theorem remains a good approximation even for these non-equilibrium systems. In order to investigate these possibilities and to explore the origin of the $S_{0.5}$-stellar mass relation, we analyze a large suite of hydrodynamical galaxy merger simulations. Mock observations of this simulation set provide kinematic data on isolated disk galaxies, disturbed galaxies, merging/overlapping galaxies, and elliptical merger remnants. The simulations allow for a comparison with observational results as well as a parallel analysis of intrinsic kinematics and observational effects.

4.2 Methods

4.2.1 Galaxy Merger Simulations

We exploit a large suite of binary galaxy merger simulations originally used to study feedback and star-formation in galaxy mergers. It provides a rich source of galaxy kinematic data for galaxies with a wide range of morphologies. For full details on the

merger simulations we refer the reader to previous studies (Cox et al., 2004; Cox, 2004; Cox et al., 2006, 2008b), but we include a brief description here for completeness.

The numerical simulations performed in this work use the N-Body/SPH code GADGET (Springel et al., 2001). Hydrodynamics are included via the Lagrangian technique of smoothed particle hydrodynamics (SPH). We use the "conservative entropy" version of SPH (Springel & Hernquist, 2002). Gas is assumed, for simplicity, to be a primordial plasma that can radiatively cool via atomic and free-free emission.

All of the numerical simulations presented here include star formation. Stars are formed in regions of gas that are above a critical density for star formation at a rate proportional to the local gas density and inversely proportional to the local dynamical time-scale. The efficiency of star formation is fixed by requiring star formation to follow the observed correlation between gas surface densities and star-formation rate (Kennicutt, 1998).

We also include a simple prescription to simulate the effects of feedback from massive stars. This feedback acts to pressurize the interstellar medium and regulates the conversion of gas to stars. Details of this model and the parameter choices can be found in Cox et al. (2006). Specifically, the simulations studied in this paper used the $n2med$ parameter set. Under these assumptions the gas pressure increases as the density squared; i.e, star-forming gas has a "stiff" equation of state.

The simulations adopt a gravitational softening length $h = 400$ pc for the dark matter particles and 100 pc for the stellar and gas particles. We remind the reader that, in GADGET, forces between neighboring particles become non-Newtonian for

107

separations $< 2.3\,h$.

The disk galaxy models and orbits are cosmologically motivated, but the simulations are not cosmological since the two galaxies are isolated. Disk galaxies are constructed in equilibrium and contain dark matter, an exponential stellar disk, an extended exponential gas disk, and some contain a dense central bulge. The portion of the suite used in this study contains two types of progenitor galaxy models:

1. "Sbc" galaxies, which are modeled after local Sbc-type spirals, with a small bulge and high gas fraction.

2. "G" galaxies, which span a range of mass, bulge fraction, and gas fraction. Their properties are taken from statistical samples of local galaxies, including the Sloan Digital Sky Survey (York et al., 2000).

The Sbc mergers are all major mergers of identical progenitors with a stellar disk of $3.92 \times 10^{10} \mathrm{M}_\odot$, a gas disk of $5.36 \times 10^{10} \mathrm{M}_\odot$, a stellar bulge of $1.00 \times 10^{10} \mathrm{M}_\odot$, and a dark matter halo of $81.2 \times 10^{10} \mathrm{M}_\odot$. The Sbc series contains the widest variation of initial merger orbits and orientations, with 17 different orbits run. The G series mergers include both major mergers between identical galaxies and mergers of galaxies with mass ratios between 1:1 and 1:50. For more detail on these models see Cox (2004), Cox et al. (2008b), and Covington et al. (2008).

4.2.2 Mock Observations of the Simulations

In order to make comparisons with the observational results, we must first mock 'observe' the galaxies in the same manner as Kassin et al. (2007). They used an algorithm called ROTCURVE (Weiner et al., 2006). This algorithm was designed to obtain kinematic measurements for as many galaxies as possible by allowing seeing-compensated rotation curves to be fit using only the 2-d spectra. ROTCURVE creates an intrinsic model for the emission intensity, velocity, and dispersion, blurs this model to simulate seeing, and then fits the model to the data. The intrinsic model used is:

$$I(x,v) = G(x)\exp(-\frac{(v-V(x))^2}{2\sigma_{2d}^2}), \tag{4.1}$$

$$G(x) = \frac{I_{tot}}{\sqrt{2\pi}r_i}\exp(-\frac{(x-x_0)^2}{2r_i^2}), \tag{4.2}$$

$$V(x) = V_{rot}\frac{2}{\pi}\arctan(x/r_v), \tag{4.3}$$

where $G(x)$ is an assumed Gaussian light distribution along the slit, $V(x)$ is the rotation curve, with asymptotic velocity V_{rot} and knee radius r_v, and σ_{2d} is the velocity dispersion, which is assumed to be constant along the slit. In order to fit the spectra, $I(x,v)$ is blurred using a 1-d Gaussian in the spatial direction. After blurring, moments are taken of the blurred model in the velocity direction in order get values of average velocity and dispersion for each bin within the slit. These values are then compared against the observed rotation curve by computing a χ^2 value. χ^2 is then minimized via adjustments of V_{rot} and σ_{2d}. The other potentially adjustable parameter, r_v, is held fixed at 0.2 arcsecs. Observational results do not change significantly if r_v is varied within a reasonable range by 0.2 ± 0.1.

In order to analyze the simulations, we follow an analogous algorithm. Each simulation has snapshots every 40-100 Myr. Each of these snapshots is viewed from 11 different evenly distributed angles, and assumed to be at three different redshifts ($z \sim 0.03$, $z \sim 0.3$, and $z \sim 1.0$) resulting in a sample of roughly 150,000 mock observations. The data in Kassin et al. span $0.1 < z < 1.2$. Two of our redshift bins cover this range, and we include a low redshift bin to examine the relation with very little blurring. Physical distances are converted to arcsecs given the assumed redshift of the observation. The effects of seeing are taken into account by smearing particle positions using a Gaussian with $\sigma = 0.3$ arcsecs. If the projected separation of the two galaxies is less than 0.7 arcsecs then the two galaxies are treated as one object. This allows us to include merging and overlapping galaxies within the sample. We orient the slit by fitting an ellipse to the stellar density profile. All mock observations use a slit width of 1.0 arcsec, and the slit length varies with redshift beginning with a length of 4.0 arcsecs at $z \sim 1$ and scaling with physical galaxy size.

Within the slit, stellar particles - either all stars or just new stars (see Section 4.4.2) - are separated into 0.1 arcsec bins, mimicking the pixel width in the observations. Rotation curves are calculated using the average velocities and dispersions of the particles in each bin. We fit $G(x)$ to the bin masses and calculate $I(x,v)$ and $V(x)$ as above. Unlike Weiner et al. (2006) and Kassin et al. (2007) we do not hold r_v fixed, but instead assume a value of 0.2 arcsecs at $z \sim 1$ and scale that value with the physical size of the galaxy as redshift decreases. If we do not scale r_v and the slit length with redshift, we get spurious systematic offsets in $V_{\rm rot}$ when comparing the lowest redshift

bin with the two higher redshift bins. Inclination is also calculated, using the thin disk approximation as in the observational work, and is used to correct $V_{\rm rot}$. We cut all galaxies from the sample with inclinations less than 50 degrees, as we find that the inclination fits become unreliable below that value. The observational sample is also cut for nearly edge-on disks because of dust effects, but the simulations do not suffer from the same limitation. Therefore we do not cut at large inclinations.

4.3   Comparison of the Simulations with Observations

4.3.1   Evolution of a Single Galaxy Merger

To illustrate how the kinematics of galaxies change during a merger event we follow the time evolution of a single galaxy merger. The simulation used for this study is a merger of two identical Sbc galaxies. Initially, the galaxies are set on a parabolic prograde-prograde orbit with a pericentric distance of 11.0 kpc. We depict the evolution of kinematic quantities during the merger viewed from a single angle (Figure 4.1), and follow the galaxies' evolution on the kinematic relations (Figure 4.2, numbers). The merger is assumed to be at a redshift of one.

We start off at time=0 Gyr with the progenitor, which is designed to lie on the observed TF ridge-line. The progenitor is demarcated as '1' in Figures 4.1 and 4.2. The merging galaxies have two encounters and merge during the second encounter. The first encounter occurs at 0.6 Gyr after the start of the simulation. This encounter results in a significant increase in the velocity dispersion by ~ 60 km s^{-1} and a sharp

Figure 4.1: Time evolution of rotation velocity (red dotted line), velocity dispersion (blue dashed line), and $S_{0.5}$ (solid and dash-dot black lines) during a single merger simulation of two Sbc galaxies with stellar masses of $\sim 5 \times 10^{10} M_\odot$ initially on a parabolic orbit. Care is taken to mock observe the simulations just as in the actual observations, assuming $z = 1$. The solid portion of the $S_{0.5}$ line denotes the snapshots where only a single progenitor is observed in the slit, and the dash-dot portion denotes snapshots where both progenitors are observed in the slit. The merger simulation uses the smoothed-particle hydrodynamics code GADGET (Springel et al., 2001) and includes gas, star formation, and stellar feedback. The galaxy images are extracted from the simulation using the dust radiative transfer code SUNRISE (Jonsson et al., 2006) and are shown at four different times during the merger: 1) Before any encounters, 2) shortly after the initial encounter, 3) at the final coalescence, and 4) the remnant after the galaxies have coalesced. With each encounter, the rotation velocity decreases and the integrated velocity dispersion increases. However, $S_{0.5}$ remains relatively constant throughout the merger, increasing primarily when the two galaxies coalesce.
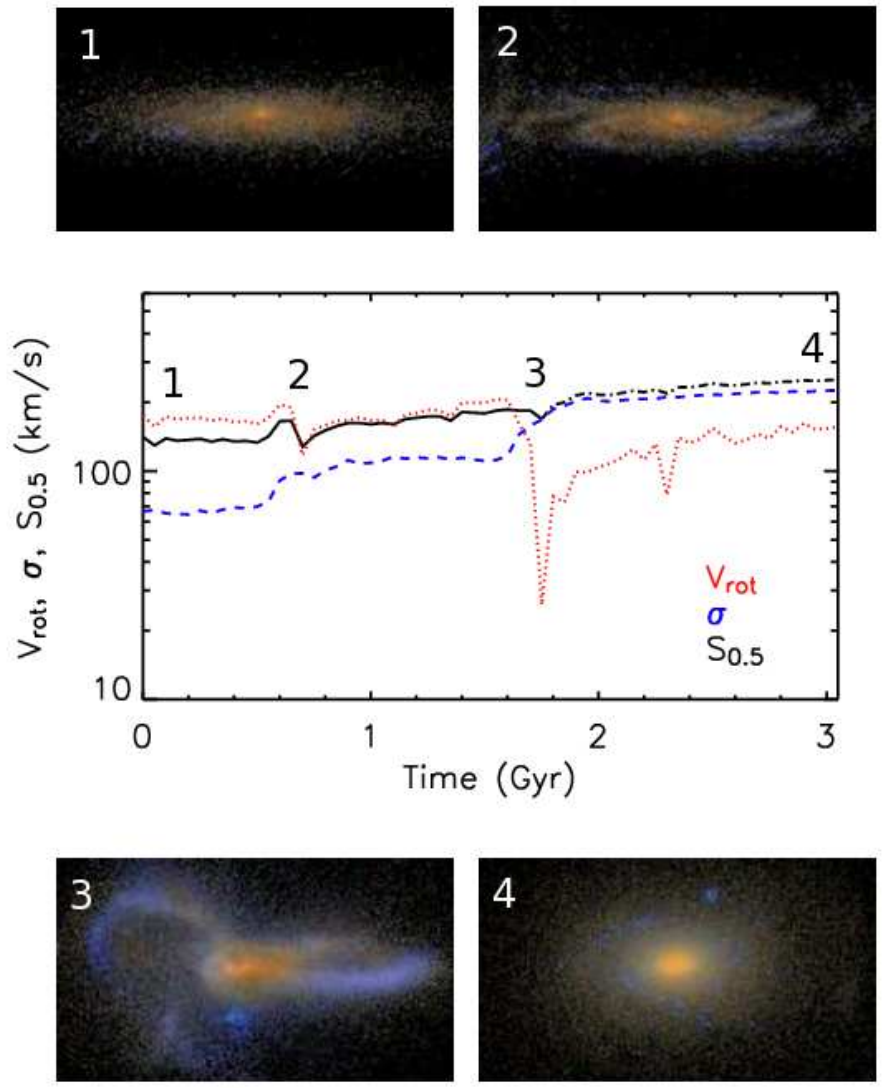
Figure 4.1:

decrease in the rotation velocity by ~ 55 km s^{-1}. During this encounter the galaxy appears morphologically disturbed, especially in its outer disk. Shortly following the encounter, at 0.7 Gyr, the galaxy is a slightly low rotation velocity outlier in the TF ('2' in Figure 4.2). Between the first and second/final encounters, the rotation velocity of the galaxy gradually increases by ~ 20 km s^{-1} as tidal debris that was removed from the disk settles back. The final coalescence occurs at 1.75 Gyr after the start of the simulation ('3' in Figure 1). At coalescence, the galaxy's rotation velocity drops abruptly to a meager 20 km s^{-1}. The mock observational slit now contains both the first progenitor and the remains of the second progenitor, which has been severely disrupted. Projection results in the overlapping of the two progenitors within the slit and pollutes the rotation curve, causing the dramatic decrease in rotational velocity. Consequently, the system lies furthest from the TF law at this time ('3' in Figure 4.2). At the final coalescence we find an increase in the velocity dispersion by ~ 100 km s^{-1}. From this point on, the kinematics are dominated by dispersion rather than rotation. The final stage (4) depicts the merger remnant, which is a rotating elliptical galaxy. In contrast to the other kinematic quantities, $S_{0.5}$ remains relatively stable throughout the merger process, increasing primarily when the two progenitors combine to create a more massive system.

The tendency for rotation velocity to decrease as velocity dispersion increases during galaxy interactions and mergers provides a simple mechanism to explain the observed $S_{0.5}$-stellar mass relation and large scatter in the conventional TF. We note, however, that observed $S_{0.5}$ is not strictly conserved, even when mass is constant. During

a close encounter all of the 'lost' rotation is not immediately converted into velocity

dispersion. Rather, the tendency during such an encounter is for the apparent rotation

velocity to briefly drop to very low values while the velocity dispersion increases only

modestly. The effects of this lack of strict conservation of $S_{0.5}$ fall within the scatter

of the $S_{0.5}$-stellar mass relation. It is not surprising that there is no strict conservation

of $S_{0.5}$, however it is perhaps surprising that $S_{0.5}$ is conserved as well as it is even in

non-equilibrium cases.

4.3.2   Kinematic Relations for an Ensemble of Simulated Galaxy Mergers

In order to further test this explanation for the observed kinematic relations,

we plot rotation velocity and $S_{0.5}$ versus stellar mass for 500 randomly chosen snapshots

from our suite of merger simulations and compare to similar plots for 544 galaxies from

Kassin et al. (2007) (Figure 4.2). These 500 snapshots are analyzed assuming $z \sim 0.03$,

$z \sim 0.3$, and $z \sim 1.0$. We find that at all redshifts the simulated TF has a significant

scatter to low V_{rot} (spanning ~ 1.5 dex), as in the observations. Furthermore, this

scatter is correlated with close encounters. Sixty-four percent of the cases with scatter

greater than 0.5 dex are encounters/mergers, whereas encounters/mergers are only 30%

of the entire sample. The scatter in the TF also decreases somewhat with redshift, as

in the observational results, suggesting that the change in scatter could be the result of

observational effects such as blurring and slit size.

If we incorporate random internal motions using $S_{0.5}$, then we find a single,

115

Figure 4.2: The TF relation (left) and $S_{0.5}$-stellar mass relation (right) for mock observations of simulated merging galaxies at redshifts of $z \sim 0.03$ (top), $z \sim 0.3$ (middle), and $z \sim 1.0$ (bottom). Each dot represents a mock observation of a single snapshot viewed from a single angle. In order to compare with the observational results from Kassin et al. (2007) 500 such images were chosen from the simulation set at random. Red points are mock observations where both galaxies are present in the slit (i.e. close encounters and the merger remnant), and black points are mock observations of single simulated galaxies. In the TF plots the solid line is the high-redshift TF ridge line from Conselice et al. (2005), with the dotted lines representing the scatter. As in Kassin et al. (2007) a significant number of the simulated galaxies scatter to low $V_{\rm rot}$. In the observations, these galaxies have disordered or compact morphologies. Similarly, in the simulations, the majority of the cases scattered to low $V_{\rm rot}$ are either undergoing or have recently undergone an encounter. In the $S_{0.5}$ plots, the solid line is the fit to the observed $S_{0.5}$ relation at $z \sim 1.0$, and the dotted lines depict scatter in the relation. The dashed line is the best fit to the simulations. Slopes (m), zero points (y0), and scatters (σ) for each fit are listed. Including velocity dispersion greatly reduces the scatter and brings the progenitors, disturbed galaxies, merging galaxies, and merger remnants onto a single kinematic relation. The relation and scatter found for the simulated galaxies are comparable to the observed relation. Numbers on the plots show the location of the various numbered merger stages from Figure 4.1. The bottom panel has no '2' because it overlaps '1'.
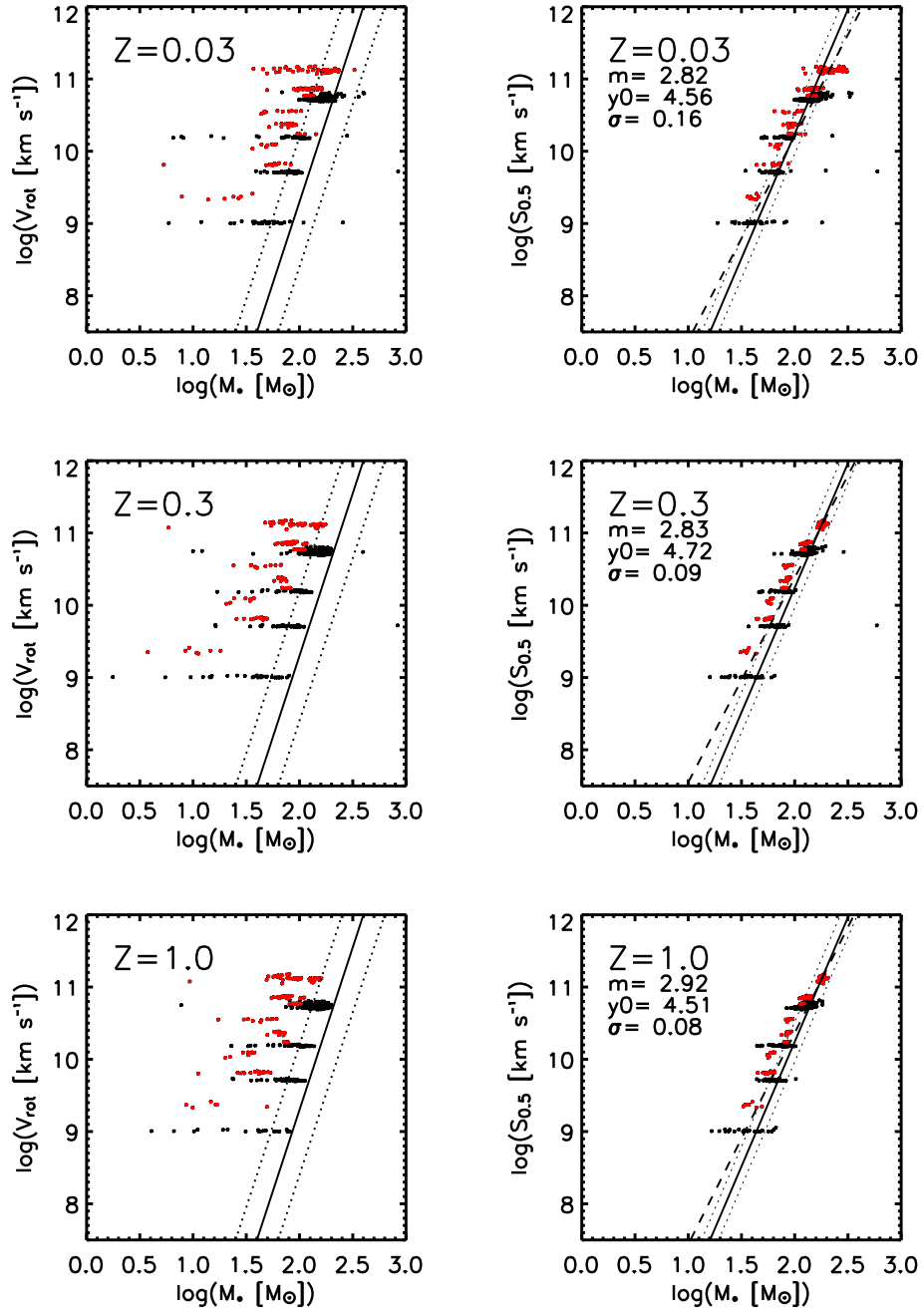
Figure 4.2:

relatively tight relation with stellar mass. Comparing different redshift bins we see that the slope fitted to the simulated galaxies stays within a range of $\sim 2.8 - 2.9$, whereas the observed slopes are typically slightly steeper but range between $\sim 2.4 - 3.3$. There is no significant trend in slope with redshift in either the observations or simulations. In the two higher redshift bins the scatter in $S_{0.5}$ for the simulations is 0.08-0.09 dex. The intrinsic scatter in the observed relation ranges between 0.08 and 0.12 dex and also has no systematic trend with redshift. The lowest redshift bin for the simulated results does show more scatter (0.16 dex), but this is likely due to difficulty in fitting unblurred rotation curves of disturbed objects, which often do not look like the idealized arctan rotation curve. This is also outside of the range of the observations discussed in Kassin et al. (2007).

While a detailed quantitative comparison of the samples is not warranted because the galaxies in the simulation suite are not a statistically representative sample of the types of galaxies that one would expect to find in the real Universe, the agreement with the observed relations demonstrates that galaxy mergers and interactions are a mechanism that can create large scatter in the TF concurrent with low scatter in the $S_{0.5}$-stellar mass relation.

Furthermore, the simulated results show that the merging process moves galaxies up the $S_{0.5}$-stellar mass relation toward higher values of $S_{0.5}$, and therefore that the relation ties together progenitors (spirals), merging galaxies, and merger remnants (ellipticals). The robustness of this relation has two causes. First, throughout the merger process there is a tendency for rotation and velocity dispersion (or, random internal mo-

118

tions) to be anti-correlated. It has been known for a long time that galaxy mergers are an effective mechanism for converting ordered rotational support into random pressure support (Toomre & Toomre, 1972). As noted above, it is surprising that a kinematic relation would hold for even merging cases. This results from a subtly different cause. Much of the apparent rotation velocity may be lost in an encounter when the two galaxies overlap in projection. This is because the two galaxies' orbital velocities and internal velocities rarely add coherently when randomly overlapped. However, velocity dispersions are not so easily lost. In fact, overlapping two galaxies with interfering rotation curves will increase velocity dispersion. Thus, when such an overlap occurs, apparent rotation typically decreases, whereas velocity dispersion typically increases.

4.4 Observational Effects on the $S_{0.5}$-Stellar Mass Relation.

From the observations alone, it is unclear the extent to which the $S_{0.5}$-stellar mass relation is a result of observational effects or is telling us something about the intrinsic properties of the galaxies. In this section, we explore the various observational effects on the kinematic measurements of the simulations and determine whether they can contribute to the observed relation.

4.4.1 Blurring

As galaxies are observed at higher redshifts, their angular extent becomes smaller. Consequently, the typical $\sim 0.7''$ seeing produced by the atmosphere effectively moves the stars from one spectral bin into other nearby bins within the slit. This reduces the apparent rotation velocity and produces an artificial velocity dispersion (Weiner et al., 2006). The fitting algorithm used by ROTCURVE takes this into account by fitting a blurred model and extrapolating back to an intrinsic model. However, an interesting question is how successful this procedure is, and whether or not blurring conserves $S_{0.5}$. If $S_{0.5}$ is conserved by blurring, then it is possible that blurring is partially responsible for the scatter in the TF and the tight $S_{0.5}$ relation.

In order to explore the effects of blurring, we take the fiducial merger simulation from §4.3.1 (the Sbc) and analyze the kinematics after blurring the particles using gaussians with σ's of 0.0", 0.1", 0.3", 0.6", 0.8", and 1.6", assuming the galaxy is at a redshift $z \sim 1$ (Figure 4.4.1). We use the four example snapshots from Figure 4.1: the undisturbed disk, disturbed disk, merger, and merger remnant. The effective blurring within the AEGIS sample is all between 0.1" and 0.3", given seeing of 0.7" (defined as full-width at half max). There is little difference between the unblurred kinematics and 0.1" kinematics for all snapshots shown. However, in both the disks and remnant there is a decrease in $V_{\rm rot}$ and increase in σ by the time we have reached 0.3". However, for all cases the decrease in $V_{\rm rot} \leq 30\%$. For all cases, as the blurring becomes much greater than R_{50}, the radius that contains 50% of the stellar mass, the ROTCURVE algorithm

breaks down and $V_{\rm rot}$ drops to very low values while σ rises.

For the undisturbed disk, disturbed disk, and merger, $S_{0.5}$ is approximately conserved by blurring as $V_{\rm rot}$ and σ adjust in lockstep. However, for the remnant, by 0.3" blurring $S_{0.5}$ has already increased by $\sim 50\%$. This results from a steeply-peaked central velocity dispersion. For zero blurring, the assumption of a constant σ underestimates the kinetic energy contribution from random motion because the central peak is small with respect to the size of the slit. As this peak gets blurred, the fit improves.

Therefore, it is true that as blurring becomes very large the ROTCURVE fitting procedure will break down and the rotational component of the kinematics will transform into dispersion. Also, for three of the four cases shown, $S_{0.5}$ is conserved throughout this process. Therefore it is true that blurring could cause some additional spread in the TF and that using $S_{0.5}$ rather than rotation velocity would help to reduce this spread. However, for the range of blurring and galaxy sizes in the observational study the ROTCURVE model performs relatively well, and certainly does not produce large enough errors to low $V_{\rm rot}$ to account for the observed scatter. This is also confirmed by the apparent lack of systematic changes in $V_{\rm rot}$ with redshift in Figure 4.2. Thus blurring cannot be the main reason for the observational findings.

4.4.2 Tracking of Emission Lines

A potential concern with our analysis is that the AEGIS observational results rely on OII 3727 emission line spectra from hot gas, whereas the kinematic analysis of the simulations described above uses all of the star particles. Specifically, the emission
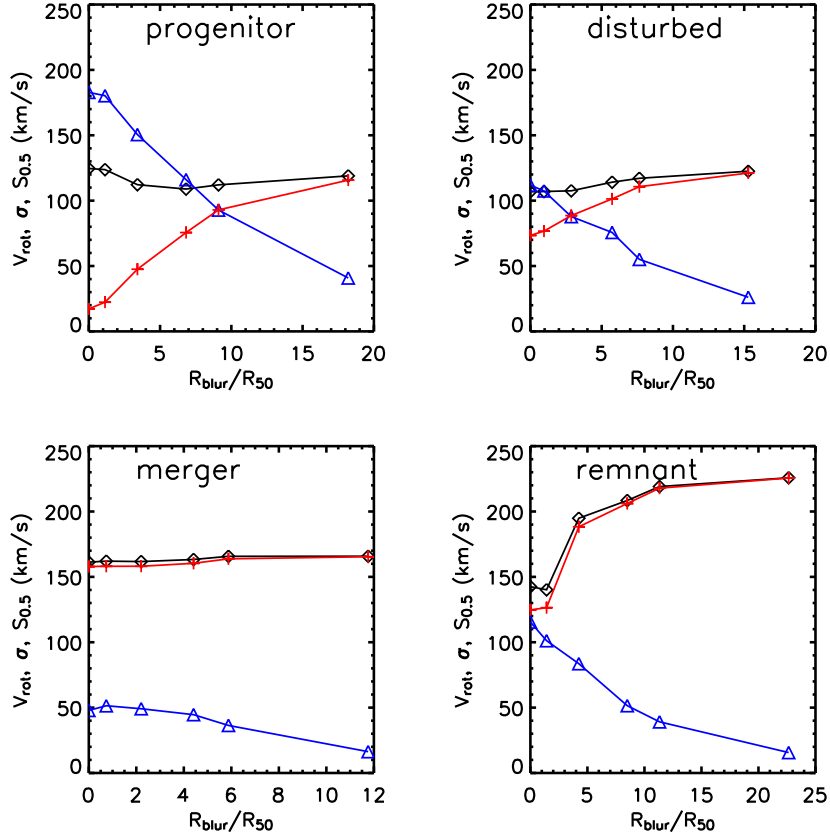
Figure 4.3: Effect of blurring on kinematics. We take the four snapshots from our fiducial Sbc merger (undisturbed disk=top left, disturbed disk=top right, merger=bottom left, and remnant=bottom right) and analyze the kinematics after blurring the particle positions by gaussians with σ's of 0.0", 0.1", 0.3", 0.6",0.8", and 1.6". Blurring is normalized using the (unblurred) radius that contains 50% of the stellar mass (R_{50}). Lines and symbols are rotation velocity (blue triangles), σ (red crosses), and $S_{0.5}$ (black diamonds).

line spectra are correlated with areas of new star formation. Thus, we repeat the analysis from §4.3.2 using only new stars that form in the simulation and assuming $z = 1$ (Figure 4.4). This gives us many fewer particles to work with, especially in the early stages of the merger when few new stars have formed. In order to provide sufficient statistics within the slit, we restrict the analysis to snapshots that have greater than 500 new star particles. This removes some of the sample from early on in the simulations, but will provide a check for whether or not limiting the analysis to new stars affects the results.

The TF and $S_{0.5}$ relations are qualitatively quite similar to those calculated using all star particles, showing large scatter for TF and relatively small scatter for $S_{0.5}$. This suggests that the observational difference between tracing kinematics using hot gas and stars does not have a significant effect on the results. There is some additional scatter in the new star $S_{0.5}$ relation (0.14 dex as compared to 0.08 dex). However, one must also remember that dust creates a counteracting effect. Within the simulations, analyzing only new stars will emphasize the central portions of the galaxies (where most stars form), however, these also tend to be the portions of the galaxy most enshrouded by dust. Thus, the real difference between the two observations is likely to be less. In order to truly pin down this effect one would have to create artificial spectral kinematics by fully modeling the radiative transfer through the gas and dust. This will soon be possible using a newer version of SUNRISE (Jonsson, 2006 and in preparation).
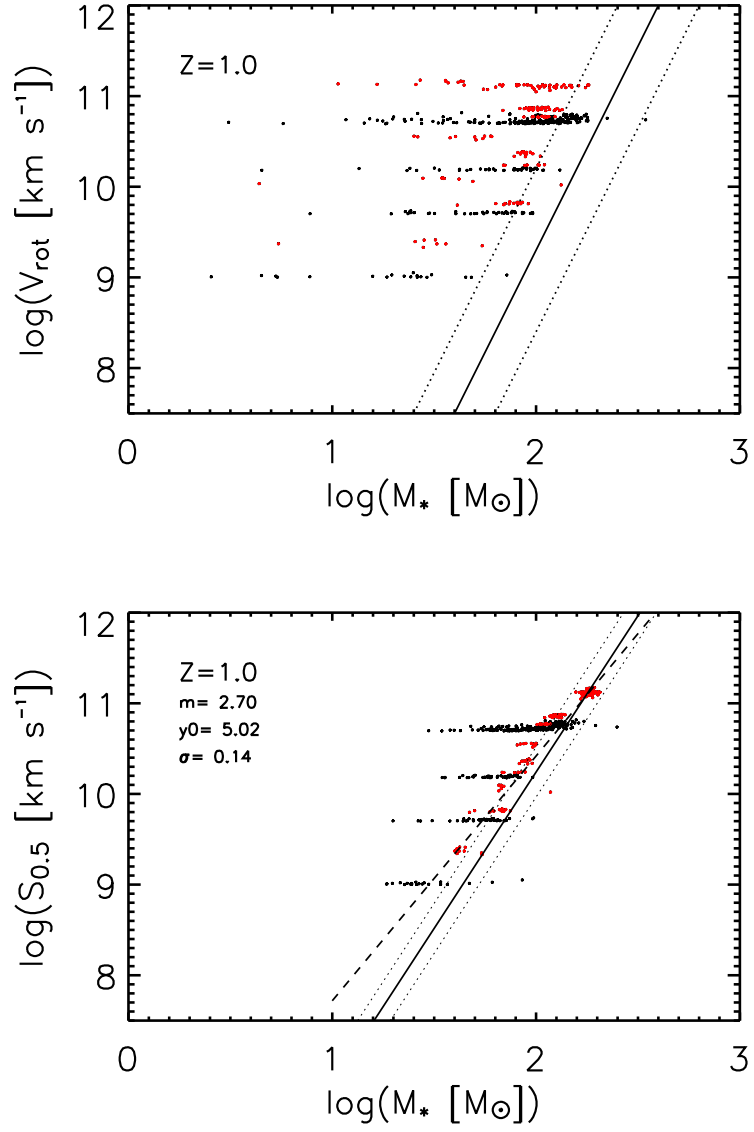
Figure 4.4: The Stellar Mass TF and S$_{0.5}$-Stellar Mass relations analogous to Figure 4.2 with the analysis from the simulations done using only new star particles.

4.5 Intrinsic Kinematic Quantities

We have explored some of the observational effects on the kinematic relations, however, we can further utilize the simulations to examine intrinsic kinematic quantities in order to better understand the origin of the $S_{0.5}$-stellar mass relation. If one assumes a tracer population within an isothermal sphere at a distance $r >> r_{core}$, where r_{core} is the core radius of the isothermal sphere, and then allows that population to assume complete rotational support or complete support from random motion then one finds that $V_{circ} \sim \sqrt{2}\sigma$, where V_{circ} is the velocity with pure circular support and σ is the dispersion for pure random support (Weiner et al., 2006; Kassin et al., 2007). This was the motivation for the multiplying factor in front of V_{rot} in $S_{0.5}$. One might expect that a smooth transition between rotational and random support, while conserving the density profile, would result in conservation of $S_{0.5}$. Therefore, an important question is whether this idealized picture is correct and $S_{0.5}$ really does trace the mass distribution. If so, this would provide a means of estimating total masses of galaxies including the contribution from dark matter.

4.5.1 Kinematics as a Function of Radius

We begin our analysis of intrinsic galaxy properties by examining kinematics as a function of radius. The $S_{0.5}$ parameter is motivated by results obtained from the Jeans Equations for an isothermal sphere. However, our systems are not isothermal spheres, so we take a step back to see where the assumptions could be wrong. For steady state

spherically symmetric systems with no rotation, the following relation holds (Binney and Tremaine, 1987, eq. (4-55)):

$$V_{\mathrm{circ}}^2 = \frac{GM(r)}{r} = -\overline{\sigma_{\mathrm{r}}^2}\left(\frac{d\ln\nu}{d\ln r} + \frac{d\ln\overline{\sigma_{\mathrm{r}^2}}}{d\ln r} + 2\beta\right), \qquad (4.4)$$

where σ_{r} is the radial velocity dispersion, ν is the mass density, $\beta \equiv 1 - \sigma_\theta^2/\sigma_\phi^2$ is the velocity anisotropy parameter, and σ_θ and σ_ϕ are the velocity dispersions in the θ and ϕ directions. At a given radius, this can be represented as the simpler

$$V_{circ}^2 = k\sigma_{\mathrm{r}^2}. \qquad (4.5)$$

For the singular isothermal sphere, the second two terms in the parentheses are zero and we are left only with $V_{\mathrm{circ}}^2 = -\overline{\sigma^2}(d\ln\nu/d\ln r)$. For an isothermal sphere with a core radius r_{core} and $r >> r_{\mathrm{core}}$ the density term $(d\ln\nu)/(d\ln r) \sim -2$, giving us the constant, $k \sim 2$, in the $S_{0.5}$ relation. For our simulation set, and for real galaxies, we are neither guaranteed that the density term will be ~ -2 nor that the other two terms will vanish. Thus we look in detail at the values these terms are likely to have.

The velocity dispersion is generally a weak function of radius. Thus the dispersion term, $d(\ln\overline{\sigma_{\mathrm{r}^2}})/d(\ln r)$ is likely to be relatively small. The drop in dispersion with radius is quite small in the progenitors and is largest for the remnants, where significant dissipation and star formation may have steepened the profiles. As shown in Dekel et al. (2005) the dispersion in the remnants is relatively well represented by $\sigma \propto r^{-0.2}$. Thus the contribution of the dispersion term in equation 4.4 is likely to be -0.2 or smaller, which is quite small compared to the presumed value of the density term. Because of tidal disturbance and dissipation, the stellar orbits in the outer portions of the merger

126

remnants do exhibit relatively large anisotropies with $\beta \sim 0.2 - 0.5$ (Dekel et al., 2005). Furthermore this term is multiplied by a factor of two bringing the overall contribution to $\sim 0.4 - 1.0$. For progenitors, which typically have low anisotropies, one would expect the contributions from these terms to roughly cancel, whereas for remnants there would be a net contribution to k of $\sim 0.2 - 0.8$.

The largest of the three terms is the density term. This term has a value of roughly two for an isothermal sphere and three or four for the outer portion of an NFW or a Hernquist profile. Thus we very well might expect a steeper density relation, $\rho \propto r^{-a}$, and consequently higher value of k than is found for the isothermal case. For each simulation we fit a value of a to the total mass density curve in the vicinity of R_{50}, the radius that contains 50% of the stellar mass. For the simulations, the value of a at R_{50} ranges between $\sim 1.75 - 3.5$, with the majority falling between negative two and three. The slope is typically steeper for massive progenitors and for merger remnants. In summary, for progenitors the density term is likely to be ~ 2, while the other terms will be small. For remnants, the density term will often be closer to 3, but the anisotropy term is likely to counteract much of this effect. So for all cases $k \sim 2$ is a reasonable value, but the variability in the density profiles and kinematics is sure to produce variation around this value.

For our exploration of intrinsic galaxy quantities we adopt a quantity, $S \equiv \sqrt{V_{\mathrm{rot}}^2 + 2.0\sigma^2}$, which is just $\sqrt{2}S_{0.5}$ but with the benefit that it approaches V_{rot} in the low-σ limit. This provides a quantity that can be directly compared with V_{circ}. The constant k is a function of radius, and therefore it is useful to determine the range in

radius for which $k \sim 2$, or alternatively $S \sim V_{circ}$. In order to examine the value of k as a function of radius we stack all of the simulated galaxies, normalizing radii to R_{50}. For this analysis, we separate the particles into bins with width equal to $0.2R_{50}$. For each bin we determine an average velocity and velocity dispersion for the stellar particles within the bin. This provides us with intrinsic quantities analogous to $V_{\rm rot}$ and σ. These values are used to calculate $S_{\rm intrinsic}$. $V_{\rm circ}$ is calculated for each bin by totaling the masses of all particles with a radius less than the bin, including baryons and dark matter. In Figure 4.5 we plot the ratio of $S_{\rm intrinsic}$ and $V_{\rm circ}$ as a function of radius averaged over the velocity profiles of every snapshot within the simulation suite. One can see that at small radii the relation does not hold, as the ratio ($S_{\rm intrinsic}/V_{\rm circ}$) becomes closer to 2 or 3 on average with a large scatter between simulated profiles. However, at radii equal to or larger than R_{50} the ratio is quite close to unity and the scatter is about 30% in either direction. Therefore, at radii larger than R_{50}, $S_{\rm intrinsic}$ is a good indicator of total enclosed mass. For simplicity, we choose a radius of R_{50} at which to draw a value of $S_{\rm intrinsic}$ for comparison across the entire sample.

4.5.2 $S_{\rm intrinsic}$-V_{circ} Relation

Now that we have demonstrated that $S_{\rm intrinsic}$ is roughly comparable to $V_{\rm circ}$ at R_{50}, it is illustrative to plot the relation between $S_{\rm intrinsic}$ and $V_{\rm circ}$ for the sample. We take these values at R_{50} and plot them for 500 randomly chosen snapshots (Figure 4.6). If the two galaxies were separated by less than the sum of their stellar half-mass radii then they were treated as one. The $x = y$ line represents equality between the two
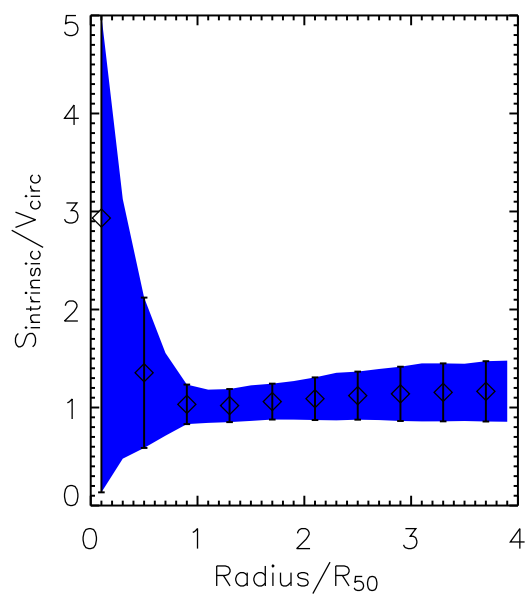
Figure 4.5: Ratio of $S_{\mathrm{intrinsic}}$ and V_{circ} as a function of radius averaged over all simulation snapshots and normalized to R_{50}. Blue range shows the 1σ scatter in the profiles.
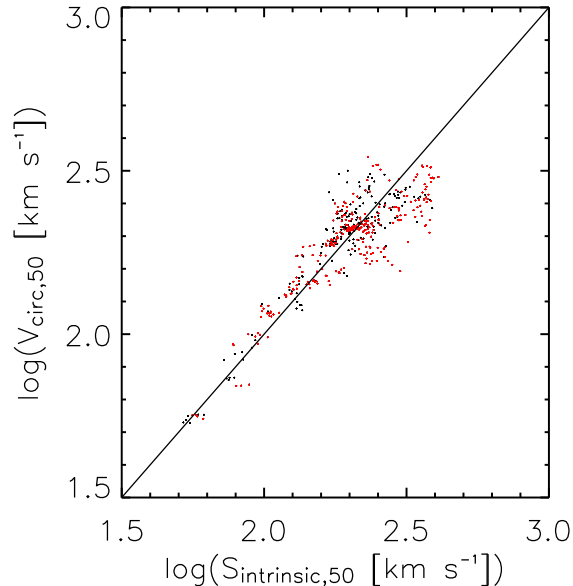
Figure 4.6: Relation between intrinsic $S_{\mathrm{intrinsic}}$ and V_{circ} at R_{50} as observed in the galaxy merger simulations. Red points are cases for which both galaxies were analyzed together, most of which are remnants. The $x = y$ line shows the rough equivalence of $S_{\mathrm{intrinsic}}$ and V_{circ}.

values. One can see that $S_{\mathrm{intrinsic}}$ is a good indicator of enclosed mass. The scatter in the relation increases with mass. This is the result of the distribution of galaxy types in the simulations. There are considerably more simulations run for the larger galaxies, and these simulations have a wide variety of orbits that can introduce significant spread in remnant properties (Covington et al., 2008). Therefore our simulation set will automatically produce more spread at higher masses. However, even for the larger mass cases, whose spread is likely more representative of the real universe than the low mass cases, $\log(S_{\mathrm{intrinsic}}) \sim \log(V_{\mathrm{circ}})$ to typically within 0.15 dex.

4.5.3 Correlation between S_{observed} and Intrinsic V_{circ}

A final question of interest is whether or not the observed quantity, S, can be used to estimate the galaxy mass, including the contribution from dark matter. To address this question we plot the relation between S_{observed} and the intrinsic V_{circ} (Figure 4.7). Again, we have moved the factor of 2 in the $S_{0.5}$ quantity over to the σ in order to produce a correspondence between S_{observed} and V_{circ}. Here we calculated a projected R_{50} using an elliptical aperture and measure a three-dimensional V_{circ} within that radius. The V_{rot} values are taken as the value of the fitted arctan curve at R_{50} rather than the asymptotic value. The observations are assumed to be at a redshift of one. As can be seen in Figure 4.7, there is a rough correspondence between S_{observed} and V_{circ}. Therefore, we take this result as a confirmation that S_{observed} can be used to track central galaxy mass, including contributions from dark matter. There is a tendency for S_{observed} to be a bit lower than V_{circ}. This is likely the result projection effects and counter-rotation, both of which would serve to reduce S_{observed}. The outliers to low S_{observed} are typically overlapping cases where the kinematics are poorly represented by an arctan curve. The fact that the intrinsic relation is significantly better than the observed one suggests that it may be possible to improve the observational measurement of S. The assumptions of the arctan rotation curve and flat velocity dispersion often fail for the simulated galaxies, particularly when two galaxies overlap. Future work should examine possible improvements to the observational algorithm.
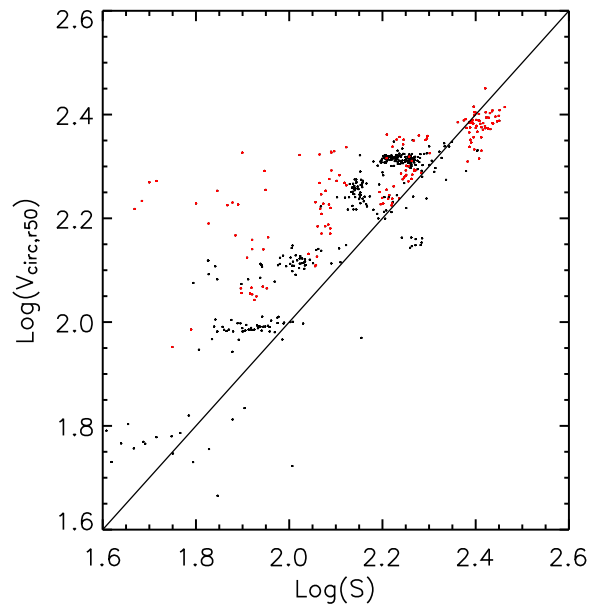
Figure 4.7: Relation between S_{observed} and V_{circ} as measured at R_{50}. Red points are case for which both galaxies are analyzed together. The line plotted is the x=y line, demonstrating the correspondence between the two values.

4.6   Discussion

The observational results from Kassin et al. (2007) were interesting for several reasons. They demonstrated that a new kinematic quantity, $S_{0.5}$, was capable of producing a relation that unified all galaxy types, including disturbed and merging cases. However, this study left open several questions that cannot be answered from the observations alone. First, what sort of mechanisms could produce the large scatter in the stellar mass TF while preserving the $S_{0.5}$-stellar mass relation? A second question is whether the relation is telling us something deep about the observed galaxies, or whether it is an artifact from the observations. Here we used a suite of galaxy merger simulations to address these questions.

We find that galaxy mergers and interactions are capable of reproducing the observed relation. Specifically, there are merger stages during which the galaxies overlap and the rotation velocity significantly drops. This overlap results in increased dispersion which when included in a kinematic relation helps to reduce the scatter. Additionally, within a given merger one can see that rotational support is transformed into random pressure support. This transformation occurs in such a way that $\log(S_{0.5})/\log(M_{\mathrm{star}})$ is roughly conserved. Thus, galaxy mergers move galaxies up along the $S_{0.5}$-stellar mass relation, and the relation effectively unifies progenitors, mergers, and remnants.

We examine the observational effect of blurring to see whether it could be responsible for the observed additional dispersion and lack of rotation. We find that the ROTCURVE algorithm performs well for the range of blurring found in the obser-

vations. We also find that $S_{0.5}$ is typically conserved by blurring. Therefore it could be responsible for some of the reduction in scatter, but the effect is much too small to account for the observed scatter.

Our examination of the kinematic scaling laws of the galaxies, and how they change with radius suggests that the appropriate constant in the $S_{0.5}$ parameter is ~ 2. Additionally, we find that S at R_{50} is a reasonably good tracer of $V_{\rm circ}$ at R_{50}. Therefore, it can be used to infer the galaxy mass within R_{50}, including contributions from dark matter. However, the details of this relation warrant more study. Specifically, the relation between $S_{\rm intrinsic}$ and $V_{\rm circ}$ is much better than that with $S_{\rm observed}$, suggesting that it may be possible to improve the observational measurement of S and consequently of the total enclosed mass. Additionally, it would be interesting to compare the merger simulations with galaxies at lower redshift, perhaps using integral field unit kinematic data. It is also likely that kinematics could be used as an indicator for merging galaxies, and possibly merger stage, since mergers often produce TF outliers and typically have significant asymmetry in their kinematics, but the development of new kinematic indicators of merging is left for future work.

Chapter 5

Conclusion

5.1 Summary

The central endeavor of this dissertation has been to further the understanding of the role of galaxy mergers in galaxy formation. In this pursuit I have used a number of different approaches. The work in this dissertation relies heavily on the galaxy merger simulation suite developed by Cox (2004). In Chapter 2 of the dissertation, I use the merger simulation suite to motivate and calibrate an analytical model that is capable of predicting the properties of merger remnants. Previous such models have used no calibration from simulations and have relied on a pure energy conservation approach, not allowing for the effects of gas dissipation (Cole et al., 2000b). We demonstrate that dissipation is a crucial effect for predicting the properties of remnants of gaseous mergers, which arguably are the majority case in the real universe. Additionally, we show that merger orbit can have a significant effect on the amount of dissipation and therefore the properties of the remnant. The model, though more complex than that of Cole et al. (2000b), is capable of accurately predicting the sizes, stellar masses, and velocity dispersions of the simulated merger remnants. This allows interpolation between and extrapolation beyond the cases in the merger suite.

In Chapter 3 we apply the new merger model using two SAMs (Croton et al., 2006; Somerville et al., 2008). Rather than fully implementing the model within the SAMs, we apply it in postprocessing. This allows the quick calculation of the properties of new elliptical galaxies arriving into the population via major mergers of disk galaxies. The SAMs have mixed success at matching the observed scaling relations, but a test

using progenitors that match the observed properties of disk galaxies demonstrates that the model performs well when given the proper input. This further suggests that the model parameters as tuned from the simulations do not require further adjustment. The study produces a simple picture that explains production of elliptical scaling laws from disk scaling laws. Perhaps the two most salient features of the elliptical scaling laws are the tilt of the fundamental plane and the rotation of the size-mass relation with respect to the disk relation. The merger model captures these features and provides a simple physical mechanism that explains both. If the disk galaxies have a gas fraction gradient, as observed (Kannappan, 2004), then the changing amount of dissipation with mass produces both the tilt in the fundamental plane and the rotation in the size-mass relation. Larger gas fractions in the smaller mass progenitors result in greater dissipation and therefore smaller remnants. Additionally, more dissipation produces a larger concentration of baryons relative to dark matter, effectively lowering the central dark matter fraction. This changing dark matter fraction with mass provides an explanation for the tilt in the fundamental plane. The overall success in the model suggests that major mergers of disk galaxies are a valid mechanism for producing elliptical galaxies. Other mechanisms, such as monolithic collapse would need to have similar success in order to be viable.

In Chapter 4 we undertake a comparison between the merger simulations and observations of kinematics of high redshift galaxies. Kassin et al. (2007) show that disturbed and merging galaxies produce low-velocity outliers in the stellar-mass Tully-Fisher relation. However, if velocity dispersion is combined with rotation in a parameter

$S_{0.5} = \sqrt{0.5V_{\mathrm{rot}}^2 + \sigma^2}$ then this results in a relatively tight relation with stellar mass. This observational result leads to a number of questions. Are galaxy mergers responsible for this effect? Is $S_{0.5}$ telling us something deep about the galaxies or is it just the result of observational effects? We construct mock observations of the merger simulations and demonstrate that mergers can reproduce the observed relation. Overlapping, disturbed, and merging cases tend to result in low-velocity outliers, but these very cases also typically have enhanced dispersion such that $S_{0.5}$ produces a tight relation with stellar mass. The $S_{0.5}$-stellar mass relation also holds for merger remnants and therefore unifies progenitors, disturbed galaxies, merging galaxies, and elliptical galaxies in one relation. Mergers simply increase mass and $S_{0.5}$ and move galaxies up the relation. In addition to confirming mergers as a possible mechanism for producing the observed relations, we examine the effect of blurring and demonstrate that $S_{0.5}$ has a real physical meaning. It tracks the total enclosed mass, or V_{circ}. We demonstrate this by examining intrinsic kinematic quantities as well as the mock observational quantities. The intrinsic S-V_{circ} relation has less scatter than the relation with observed S.

This dissertation work adds to the growing body of evidence that galaxy mergers are a powerful explanatory tool within galaxy formation. We show that galaxy mergers provide an effective mechanism for producing observed scaling relations of elliptical galaxies and also are capable of explaining the observed low rotation velocity outliers in the TF concurrent with a tight $S_{0.5}$-stellar mass relation.

5.2   Future Work

In many ways this work is just the beginning of what could be a long train of research questions. Our merger model is capable of explaining the broad strokes of the scaling relations of elliptical galaxies, but many questions remain. An important constraint will be data concerning the evolution of the FJ and FP relations to high redshift. The model currently makes predictions, but there is little observational data with which to compare. Perhaps the most important next step is fully incorporate the merger model within a SAM. This will allow self-consistent predictions of the evolution of the entire elliptical population, rather than just the new arrivals. Furthermore, it may turn out that the scaling relations provide powerful constraints on other elements of the galaxy formation model, such as galaxy gas fractions. Surely in order to properly capture evolution of scaling relations one must also properly capture evolution of gas. Additionally, full incorporation within SAMs will allow the study of the cross-correlation of many other galaxy attributes such as age, metallicity, and environment.

Another important question is whether there are sections of the observed population that are not produced by binary mergers. Perhaps these ellipticals are produced by many subsequent minor mergers, by multiple mergers, or even by monolithic collapse. It will be important to outline the properties of the galaxies produced by each of these mechanisms in order to understand the role played by each mechanism. A useful contribution here would be to develop similar simulation-calibrated analytical toy models for the other mechanisms.

Regarding the $S_{0.5}$-stellar mass relation many questions also remain. Perhaps the most pressing is that the intrinsic S quantity provides a much better indicator of V_{circ} than the observed quantity. The disturbed and merging cases in the simulation often have velocity curves that look little like the idealized arctan curve. Also the velocity dispersion curve often varies significantly from being flat as a function of radius. Taking these effects into account, it is likely that a better algorithm for calculating S can be devised. For this study it might be useful to examine more detailed kinematics of low-redshift galaxies. It is also quite likely that analysis of 2D integral field unit data could lead to the development of a similar but more powerful means for constraining V_{circ}. In any case detailed comparisons of kinematics of observed galaxies and merger simulations is likely aid our understanding of galaxy formation. Some of this work has already been undertaken by Greg Novak for his dissertation (2008, in progress).

A final future direction of research that I wish to note is the use of kinematics as an indicator of mergers and merger stage. Previous approaches have met relative success at using morphological classification as an indicator of galaxy mergers (Lotz et al., 2004, 2008). However, these methods could likely be improved via the inclusion of kinematic information. As we have demonstrated, galaxy mergers can produce unique kinematic signatures, particularly anomalously low rotation velocities. However, there are many other possible kinematic signatures of galaxy mergers, including asymmetry in the velocity curves, asymmetry in the dispersion curves, and rotation curves that deviate significantly from the idealized arctan curve due to tidal disturbance. A careful study of the simulations would likely lead to novel indicators of mergers and merger

stage. This could be particularly powerful if combined with the approach already used by Lotz et al.

Bibliography

Aguilar L. A., White S. D. M., 1985, ApJ, 295, 374

Barden M., Rix H.-W., Somerville R. S., Bell E. F., Häußler B., Peng C. Y., Borch A.,
   Beckwith S. V. W., Caldwell J. A. R., Heymans C., Jahnke K., Jogee S., McIntosh
   D. H., Meisenheimer K., Sánchez S. F., Wisotzki L., Wolf C., 2005, ApJ, 635, 959

Barnes J. E., 2002, MNRAS, 333, 481

Barnes J. E., Hernquist L., 1992, ARA&A, 30, 705

Benson A. J., 2005, MNRAS, 358, 551

Bernardi M., Sheth R. K., Annis J., Burles S., Eisenstein D. J., Finkbeiner D. P., Hogg
   D. W., Lupton R. H., Schlegel D. J., SubbaRao M., York D. G., 2003a, AJ, 125, 1849

Bernardi M., Sheth R. K., Annis J., Burles S., Eisenstein D. J., Finkbeiner D. P., Hogg
   D. W., Lupton R. H., Schlegel D. J., SubbaRao M., York D. G., 2003b, AJ, 125, 1866

Binney J., Tremaine S., 1987, Galactic dynamics. Princeton, NJ, Princeton University
   Press, 1987, p.747

Blumenthal G. R., Faber S. M., Primack J. R., Rees M. J., 1984, Nature, 311, 517

Bolton A. S., Burles S., Treu T., Koopmans L. V. E., Moustakas L. A., 2007, ApJL, 665, L105

Bolton A. S., Treu T., Koopmans L. V. E., Gavazzi R., Moustakas L. A., Burles S., Schlegel D. J., Wayth R., 2008, ArXiv e-prints, 805

Boylan-Kolchin M., Ma C.-P., Quataert E., 2006, MNRAS, 369, 1081

Bryan G. L., Norman M. L., 1998, ApJ, 495, 80

Calura F., Jimenez R., Panter B., Matteucci F., Heavens A. F., 2007, ArXiv e-prints, 707

Cappellari M., Bacon R., Bureau M., Damen M. C., Davies R. L., de Zeeuw P. T., Emsellem E., Falcón-Barroso J., Krajnović D., Kuntschner H., McDermid R. M., Peletier R. F., Sarzi M., van den Bosch R. C. E., van de Ven G., 2006, MNRAS, 366, 1126

Ciotti L., Lanzoni B., Volonteri M., 2007, ApJ, 658, 65

Cole S., Aragon-Salamanca A., Frenk C. S., Navarro J. F., Zepf S. E., 1994, MNRAS, 271, 781

Cole S., Lacey C. G., Baugh C. M., Frenk C. S., 2000a, MNRAS, 319, 168

Cole S., Lacey C. G., Baugh C. M., Frenk C. S., 2000b, MNRAS, 319, 168

Conselice C. J., Bundy K., Ellis R. S., Brichmann J., Vogt N. P., Phillips A. C., 2005, ApJ, 628, 160

Covington M., Dekel A., Cox T. J., Jonsson P., Primack J. R., 2008, MNRAS, 384, 94

Cox T. J., 2004, PhD thesis, UC Santa Cruz

Cox T. J., Jonsson P., Primack J. R., Somerville R. S., 2006, MNRAS, 373, 1013

Cox T. J., Jonsson P., Somerville R. S., Primack J. R., Dekel A., 2008a, MNRAS, 384, 386

Cox T. J., Jonsson P., Somerville R. S., Primack J. R., Dekel A., 2008b, MNRAS, 384, 386

Cox T. J., Primack J., Jonsson P., Somerville R. S., 2004, ApJL, 607, L87

Croton D. J., Springel V., White S. D. M., De Lucia G., Frenk C. S., Gao L., Jenkins A., Kauffmann G., Navarro J. F., Yoshida N., 2006, MNRAS, 365, 11

Dekel A., Cox T. J., 2006, MNRAS, 370, 1445

Dekel A., Shaham J., Lecar M., 1980, ApJ, 241, 946

Dekel A., Stoehr F., Mamon G. A., Cox T. J., Novak G. S., Primack J. R., 2005, Nature, 437, 707

Diemand J., Kuhlen M., Madau P., 2006, ArXiv Astrophysics e-prints

Djorgovski S., Davis M., 1987, ApJ, 313, 59

144

Dressler A., Lynden-Bell D., Burstein D., Davies R. L., Faber S. M., Terlevich R., Wegner G., 1987, ApJ, 313, 42

Faber S. M., Jackson R. E., 1976, ApJ, 204, 668

Gallazzi A., Charlot S., Brinchmann J., White S. D. M., 2006, MNRAS, 370, 1106

Gerhard O., Kronawitter A., Saglia R. P., Bender R., 2001, AJ, 121, 1936

Gunn J. E., Gott J. R. I., 1972, ApJ, 176, 1

Hatton S., Devriendt J. E. G., Ninin S., Bouchet F. R., Guiderdoni B., Vibert D., 2003, MNRAS, 343, 75

Hopkins P. F., Cox T. J., Hernquist L., 2008, ArXiv e-prints, 806

Hopkins P. F., Hernquist L., Cox T. J., Di Matteo T., Robertson B., Springel V., 2006, ApJS, 163, 1

Jonsson P., 2006, MNRAS, 372, 2

Jonsson P., Cox T. J., Primack J. R., Somerville R. S., 2006, ApJ, 637, 255

Kannappan S. J., 2004, ApJL, 611, L89

Kassin S. A., Weiner B. J., Faber S. M., Koo D. C., Lotz J. M., Diemand J., Harker J. J., Bundy K., Metevier A. J., Phillips A. C., Cooper M. C., Croton D. J., Konidaris N., Noeske K. G., Willmer C. N. A., 2007, ApJL, 660, L35

Kauffmann G., White S. D. M., Guiderdoni B., 1993, MNRAS, 264, 201

Kennicutt R. C., 1998, ApJ, 498, 541

Khochfar S., Burkert A., 2006, A&A, 445, 403

Kormendy J., 1977, ApJ, 218, 333

Larson R. B., 1974, MNRAS, 166, 585

Lotz J. M., Jonsson P., Cox T. J., Primack J. R., 2008, ArXiv e-prints, 805

Lotz J. M., Primack J., Madau P., 2004, AJ, 128, 163

McIntosh D. H., Bell E. F., Rix H.-W., Wolf C., Heymans C., Peng C. Y., Somerville
  R. S., Barden M., Beckwith S. V. W., Borch A., Caldwell J. A. R., Häußler B., Jahnke
  K., Jogee S., Meisenheimer K., Sánchez S. F., Wisotzki L., 2005, ApJ, 632, 191

Mihos J. C., Hernquist L., 1994a, ApJL, 437, L47

Mihos J. C., Hernquist L., 1994b, ApJL, 431, L9

Mo H. J., Mao S., White S. D. M., 1998, MNRAS, 295, 319

Naab T., Burkert A., Hernquist L., 1999, ApJL, 523, L133

Naab T., Jesseit R., Burkert A., 2006, MNRAS, 372, 839

Naab T., Khochfar S., Burkert A., 2006, ApJL, 636, L81

Nipoti C., Treu T., Bolton A. S., 2008, ArXiv e-prints, 806

Padmanabhan N., Seljak U., Strauss M. A., Blanton M. R., Kauffmann G., Schlegel D. J., Tremonti C., Bahcall N. A., Bernardi M., Brinkmann J., Fukugita M., Ivezić Ž., 2004, New Astronomy, 9, 329

Pahre M. A., Djorgovski S. G., de Carvalho R. R., 1998, AJ, 116, 1591

Pipino A., Matteucci F., 2004, MNRAS, 347, 968

Richstone D. O., 1975, ApJ, 200, 535

Robertson B., Cox T. J., Hernquist L., Franx M., Hopkins P. F., Martini P., Springel V., 2006, ApJ, 641, 21

Shen S., Mo H. J., White S. D. M., Blanton M. R., Kauffmann G., Voges W., Brinkmann J., Csabai I., 2003, MNRAS, 343, 978

Somerville R. S., Barden M., Rix H.-W., Bell E. F., Beckwith S. V. W., Borch A., Caldwell J. A. R., Häußler B., Heymans C., Jahnke K., Jogee S., McIntosh D. H., Meisenheimer K., Peng C. Y., Sánchez S. F., Wisotzki L., Wolf C., 2008, ApJ, 672, 776

Somerville R. S., Primack J. R., 1999, MNRAS, 310, 1087

Somerville R. S., Primack J. R., Faber S. M., 2001, MNRAS, 320, 504

Somerville et al. 2008, MNRASsubmitted

Springel V., Hernquist L., 2002, MNRAS, 333, 649

Springel V., White S. D. M., Jenkins A., Frenk C. S., Yoshida N., Gao L., Navarro J., Thacker R., Croton D., Helly J., Peacock J. A., Cole S., Thomas P., Couchman H., Evrard A., Colberg J., Pearce F., 2005, Nature, 435, 629

Springel V., Yoshida N., White S. D. M., 2001, New Astronomy, 6, 79

Toomre A., 1977, in Evolution of Galaxies and Stellar Populations Mergers and Some Consequences. p. 401

Toomre A., Toomre J., 1972, ApJ, 178, 623

Trujillo et al. 2006, ApJ, 650, 18

Tully R. B., Fisher J. R., 1977, A&A, 54, 661

Weiner B. J., Willmer C. N. A., Faber S. M., Melbourne J., Kassin S. A., Phillips A. C., Harker J., Metevier A. J., Vogt N. P., Koo D. C., 2006, ApJ, 653, 1027

York D. G., Adelman J., Anderson Jr. J. E., Anderson S. F., Annis J., Bahcall N. A., Bakken J. A., Barkhouser R., Bastian S., Berman E., Boroski W. N., Yanny B., Yasuda N., 2000, AJ, 120, 1579

Zaritsky D., Zabludoff A. I., Gonzalez A. H., 2007, ArXiv e-prints, 711

Zel'Dovich Y. B., 1970, A&A, 5, 84